

Structure of Beryllium Isotopes in Fermionic Molecular Dynamics

**Vom Fachbereich Physik
der Technischen Universität Darmstadt**

**zur Erlangung des Grades
eines Doktors der Naturwissenschaften
(Dr. rer. nat.)**

**genehmigte Dissertation von
Dipl. Phys. Bahram Ramin Torabi
aus Berlin**

Darmstadt 2010
D17

Referent: Prof. Dr. H. Feldmeier
1. Korreferent: Prof. Dr. R. Roth

Tag der Einreichung: 27. Januar 2009
Tag der Prüfung: 16. Februar 2009

A theory is something nobody believes,
except the person who made it.

An experiment is something everybody believes,
except the person who made it.

- Albert Einstein (1879-1955)

Contents

1	Zusammenfassung und Einleitung	7
1.1	Abstract	7
1.1.1	Deutsch	7
1.1.2	English	8
1.2	Einleitung	9
2	The Nucleon-Nucleon Interaction	13
2.1	Realistic potentials	13
2.2	Unitary Correlation Operator Method	14
3	Fermionic Molecular Dynamics	19
3.1	The Hilbert Space	19
3.1.1	Single-particle states	19
3.1.2	Many-body states	21
3.2	The many-body basis	26
4	Many-Body Hilbert-Space	28
4.1	Ritz variation	28
4.1.1	Total parity	29
4.1.2	Separate parity for protons and neutrons	31
4.1.3	Variation after projection	35
4.2	Configuration mixing	37
4.3	Parameterizations	37
4.4	Constraint minimization	38
4.4.1	Lagrange multiplier	42
4.5	Constraints	42
4.5.1	Center of mass	43
4.5.2	Radius	44

CONTENTS

4.5.3	Multipoles	46
4.5.4	Single particle angular momentum	47
4.5.5	Oscillator quanta	48
4.5.6	Spin-orbit coupling	53
4.6	Selecting states	53
4.7	Spanning the Hilbert space	59
5	Results	61
5.1	Beryllium	61
5.2	Beryllium-7	63
5.3	Beryllium-8	66
5.4	Beryllium-9	69
5.5	Beryllium-10	71
5.6	Beryllium-11	74
5.7	Beryllium-12	76
5.8	Beryllium-13	78
5.9	Beryllium-14	83
5.10	Overview	85
6	Outlook	93
A	Appendix	95
A.1	General relations	95
A.2	Derivatives of the oscillator quanta constraint	97
A.3	Properties	98
A.3.1	Electromagnetic transitions	98
A.3.2	Harmonic oscillator occupation numbers	98
A.3.3	Form factors	98
A.4	Notation	100

Zusammenfassung und Einleitung

1.1 Abstract

1.1.1 Deutsch

Die moderne theoretische Kernstrukturphysik stellt sich zwei großen Herausforderungen. Die Erste ist das Finden einer geeigneten Wechselwirkung, welche die Kräfte zwischen den Nukleonen beschreibt. Die zweite Herausforderung ist das Lösen des nuklearen Vielteilchensystems für einen gegebenen Atomkern unter Verwendung eines realistischen Potentials.

Das im Rahmen dieser Arbeit verwendete Potential basiert auf dem Argonne V18 Potential. Es wurde mit Hilfe der Methode der unitären Korrelatoren (UCOM) transformiert, um die Konvergenz zu optimieren. Die üblichen phänomenologischen Terme wurden verwendet, um das Potential für den in der Fermionischen Molekulardynamik (FMD) verwendeten Hilbertraum zu verbessern. Die FMD ist ein Ansatz zur Lösung des nuklearen Vielteilchenproblems. Es wird eine Einteilchenbasis verwendet, die eine Superposition von im Phasenraum lokalisierten Gaußverteilungen ist.

Der einfachste Vielteilchenzustand ist das antisymmetrische Produkt der Einteilchenwellenfunktionen: eine Slaterdeterminante, der sogenannte intrinsische Zustand. Dieser intrinsische Zustand wird auf vorgegebene Parität und Drehimpuls sowie auf Schwerpunktsimpuls Null projiziert. Der Vielteilchen-Hilbertraum wird durch mehrere projizierte Zustände aufgespannt. Diese Zustände werden durch Minimieren der Energie mit unterschiedlichen Zwangsbedingungen gewonnen. Der Energieerwartungswert wird mit Slaterdeterminanten, paritätsprojizierten Slaterdeterminanten und zusätzlich drehimpulsprojizierten Zuständen berechnet. Die im Niederenergiebereich physikalisch relevanten Zustände werden durch Diagonalisieren im Raum der so erzeugten Vielteilchenbasis gewonnen. Zu den

verwendeten Zwangsbedingungen gehören die ersten Momente der Massen-, Protonen- oder Neutronenverteilung, und die Anregung in Protonen oder Neutronenschalen eines harmonischen Oszillators. Mit diesen Zuständen wird der Niederenergiebereich der Beryllium Isotope mit den Massen 7 bis 14 berechnet. Die Energien, Radien, elektromagnetische Übergänge, Punktdichteverteilungen und magnetischen Momente des niedrig liegenden Spektrums werden berechnet und in dieser Arbeit präsentiert.

1.1.2 English

Modern theoretical nuclear physics faces two major challenges. The first is finding a suitable interaction, which describes the forces between nucleons. The second challenge is the solution of the nuclear many-body problem for a given nucleus while applying a realistic potential.

The potential used in the framework of this thesis is based on the Argonne AV18 potential. It was transformed by means of the Unitary Correlation Operator Method (UCOM) to optimize convergence. The usual phenomenological corrections were applied to improve the potential for the Hilbert space used in Fermionic Molecular Dynamics (FMD). FMD is an approach to solve the nuclear many-body problem. It uses a single-particle basis which is a superposition of Gaussian distributions in phase-space.

The most simple many-body state is the antisymmetric product of the single-particle states: a Slater determinant, the so called intrinsic state. This intrinsic state is projected on parity, total angular momentum and a center of mass momentum zero. The Hilbert space is spanned by several of these projected states. The states are obtained by minimizing their energy while demanding certain constraints. The expectation values of Slater determinants, parity projected and additionally total angular momentum projected Slater determinants are used. The states that are relevant in the low energy regime are obtained by diagonalization. The lowest moments of the mass-, proton- or neutron-distribution and the excitation in proton- and neutron-shells of a harmonic oscillator are some of the used constraints. The low energy regime of the Beryllium isotopes with masses 7 to 14 is calculated by using these states. Energies, radii, electromagnetic transitions, magnetic moments and point density distributions of the low lying states are calculated and are presented in this thesis.

1.2 Einleitung

Aufgrund der Vielfalt an Phänomenen die in Atomkernen entdeckt wurden, gibt es inzwischen eine Vielzahl an Modellen die unterschiedliche Beobachtungen unterschiedlich erklären. Einige dieser Modelle scheinen sich dabei zu widersprechen. So wird der Atomkern beispielsweise im Schalenmodell als Fermigas, im Tröpfchenmodell als Flüssigkeit und bei der Deutung als starren Rotor analog zu einem Festkörper beschrieben.

Um die Struktur von Atomkernen zu verstehen, ohne sich ausschließlich auf Teilaspekte zu beschränken, werden auf mikroskopischen Modellen basierende Kernstrukturrechnungen benötigt, die auf realistischen Wechselwirkungen basieren. Nur wenn derartige Betrachtungen, die aus Experimenten bekannten Daten, sinnvoll reproduzieren, sind weitere Vorhersagen glaubwürdig.

Realistische Zweiteilchen-Wechselwirkungen werden dargestellt durch Potentiale, welche die bekannten Nukleon-Nukleon Streuphasen und das Deuteron im Rahmen der Fehlergrenzen perfekt beschreiben. Die Streuphasen für die Neutron-Neutron Streuung sind nur mit relativ großen Fehlern bekannt. Weitere sinnvolle Einschränkungen für z.B. das off-shell Verhalten lassen sich für das Zwei-Teilchen System nicht finden. Daher gibt es eine Vielzahl unterschiedlicher Zwei-Teilchen Potentiale, die sich teilweise deutlich unterscheiden, allerdings die Streuphasen und das Deuteron ähnlich gut beschreiben. Erst durch die Betrachtung von Drei-Teilchen Systemen lassen sich weitere Aussagen treffen.

Moderne Kernstrukturrechnungen setzen aufgrund ihrer steigenden Komplexität zunehmend auf Computer. Für derartige numerische Berechnungen wird ein Modellraum benötigt, der den relevanten Teil des Hilbert-Raumes möglichst gut beschreibt. Dennoch ist es auch mit den größten Modellräumen bisher kaum möglich, unter Verwendung realistischer Wechselwirkungen, einfache Vorhersagen wie z.B. die Bindungsenergie von ^{16}O genau zu berechnen. Der Grund sind durch die Wechselwirkung hervorgerufene Korrelationen, die sich in der Schalenmodellbasis nur unzureichend beschreiben lassen. Daher wird üblicherweise nicht eine realistische, sondern eine effektive oder phänomenologische Wechselwirkung verwendet. Die effektive Wechselwirkung wird dabei aus einer realistischen mit Hilfe unterschiedlicher Methoden gewonnen.

Die im Rahmen dieser Arbeit verwendete Zweiteilchen-Wechselwirkung wurde mit der Methode des unitären Korrelationsoperators (Unitary Correlation Operator Method - UCOM) aus der realistischen Argonne V18 Wechselwirkung gewonnen. UCOM ist eine Methode um die kurzreichweitigen Korrelationen, die der abstoßende Core und die Tensorcomponenten der realistischen Wechselwirkung induzieren, zu beschreiben [Nef02]. Diese Korrelationen lassen sich nicht mit Slaterdeterminanten darstellen. Aufgrund der kurzen Reichweite der unitären Korrelatoren bleiben dabei die Nukleon-Nukleon-Streuphasen unverändert. Daher ist es

korrekt die transformierte Wechselwirkung nicht als effektive, sondern als eine andere realistische Wechselwirkung zu betrachten. Die Parameter des Korrelationsoperators werden so gewählt, dass Beiträge einer verbleibenden Dreiteilchen-Wechselwirkung auf ein Minimum reduziert sind.

Obwohl die in der FMD verwendete Wechselwirkung noch weitere phänomenologische Korrekturen beinhaltet, können die Ergebnisse als *ab-initio* angesehen werden, da für jedes Problem und jeden Kern immer die selbe Wechselwirkung verwendet wird.

Mikroskopische Theorien haben den Anspruch, durch Lösen des nuklearen Vielteilchen-Problems auch die Aspekte phänomenologischer Modelle zu beschreiben. Durch derartige Rechnungen können Aussagen über Kerne getroffen werden, die experimentell nicht zugänglich sind. Gerade die Kerne fernab der Stabilität zeigen eine Vielzahl exotischer Phänomene.

Die im Rahmen dieser Arbeit vorgestellte Fermionische Molekulardynamik (FMD) ist ein Ansatz das nukleare Vielteilchen-Problem zu lösen. In der FMD wird von Einteilchenwellenfunktionen ausgegangen, die eine Summe von Gaußverteilungen im Phasenraum darstellen. Jede Gaußverteilung wird im Phasenraum durch die komplexen Parameter \vec{b} und a beschrieben [FBS95]. a beschreibt die Breite und die Geschwindigkeit mit der sich die Breite ändert, während \vec{b} den Schwerpunkt und dessen Geschwindigkeit charakterisiert. Die Einteilchenzustände der FMD lassen sich damit als verallgemeinerte kohärente Zustände darstellen [Kra01].

Die FMD Vielteilchenzustände sind explizit antisymmetrisiert. Sie sind wie auch die Einteilchenzustände nichtorthogonal, daher wird auch davon abgesehen sie zu normieren. Die FMD Basiszustände sind übervollständig und beinhalten nicht nur die Schalenmodellzustände und Clusterzustände, sondern können durch die variablen Breiten a der Einteilchenzustände auch Halozustände besser beschreiben als die meisten anderen Modelle.

Im Allgemeinen erfüllt der FMD Vielteilchenzustand nicht die Symmetrien des Hamilton-Operators, daher wird der Zustand auf Parität, Drehimpuls und einen Schwerpunktsimpuls von Null projiziert. Diese projizierten Zustände bilden die Basis des Modell-Hilbert-Raumes für Rechnungen mit Konfigurationsmischung.

Die Basiszustände der FMD werden durch Variation eines Energiefunktionals gewonnen. Als Funktional wird nicht nur der Energieerwartungswert einer Slater-determinante im Sinne einer Mean Field Rechnung berechnet, sondern es werden auch paritäts- oder sogar drehimpulsprojizierte Zustände verwendet.

Im Rahmen dieser Arbeit wird ein weiteres Energiefunktional vorgestellt. Dabei werden die Zustände mit Hilfe zweier Projektoren auf eine definierte Protonen- und Neutronenparität projiziert. Durch Variation dieses Funktionals werden FMD Zustände in Analogie zum Schalenmodell, dessen Basiszustände ebenfalls eine

definierte Protonen- und Neutronenparität besitzen, erzeugt. Im Schalenmodell werden Zustände mit positiver Gesamtparität im Allgemeinen als Mischung von Zuständen mit positiver Protonen- und Neutronenparität und negativer Protonen- und Neutronenparität beschrieben. Durch das neue Energiefunktional ist diese Möglichkeit in die FMD eingeführt worden.

Zusätzliche Basiszustände werden erzeugt, indem während der Variation des Energiefunktionals Nebenbedingungen gefordert werden. Verwendete Nebenbedingungen sind beispielsweise der Radius oder Multipolmomente.

Als weitere Nebenbedingung wird die Anzahl an Oszillatorquanten im Gesamtsystem eingeführt. Diese wird bestimmt indem ein dreidimensionaler nichtisotroper harmonischer Oszillator eingeführt wird. Dieser Oszillator wird so gewählt und orientiert, dass für den betrachteten FMD Zustand immer die kleinstmögliche Anzahl an Anregungsquanten bestimmt wird. Die Nebenbedingung ist so formuliert, dass diese Anzahl an Quanten sich auch auf die Protonen- oder Neutronenschale beschränken lässt.

Ohne Nebenbedingungen variierte Zustände tragen meist primär zum Grundzustand bei. Dennoch wird die Beschreibung des Grundzustandes durch eine Konfigurationsmischung mit anderen Zuständen verbessert. Bei der Beschreibung angeregter Zustände ist eine Beimischung von Zuständen, die unter Nebenbedingungen erzeugt wurden, unabdingbar.

Da zur Beschreibung der Struktur von Zuständen in Berylliumisotopen viele interessante Ansätze wie, Schalenmodellzustände, Clusterzustände, molekulare Zustände und auch Halozustände verwendet werden, stellen sie einen anspruchsvollen Test für eine Beschreibung in der FMD dar.

In dieser Arbeit wird das Niederenergiespektrum der Isotope ^7Be bis ^{14}Be durch Konfigurationsmischung berechnet. Die Grundzustandsenergien dieser Rechnungen sind in Tabelle 1.1 neben den gemessenen Energien aufgelistet.

Radien, Ladungsradien und magnetische Momente werden für die Grundzustände angegeben und den gemessenen Werten aus [NTZ⁺09] gegenübergestellt.

Einige elektromagnetische Übergänge der Berylliumisotope werden vorgestellt.

	FMD	Exp.
⁷ Be	5.40	5.37
⁸ Be	7.25	7.06
⁹ Be	6.60	6.46
¹⁰ Be	6.57	6.50
¹¹ Be	6.06	5.95
¹² Be	5.61	5.72
¹³ Be	5.20	5.27
¹⁴ Be	5.06	4.99

Table 1.1: Grundzustandsenergien wie berechnet in der FMD und experimentell ermittelt. Die experimentellen Werte sind entnommen oder berechnet aus [TKG⁺04, TCG⁺02, AWT03, SMA⁺07]. Die Einheit der angegebenen Energien ist MeV/u.

The Nucleon-Nucleon Interaction

2.1 Realistic potentials

Contrary to atomic or solid state physics, where the underlying potential is the well known Coulomb potential, the nuclear potential is still a major challenge in nuclear physics.

The fundamental theory underlying the nuclear forces is Quantum Chromo Dynamics (QCD). The relevant degrees of freedom in QCD are the color-charged quarks and gluons. This description in the lower energy region is so complex that it does not seem reasonable to try to describe anything far beyond the structure of single baryons. The high energy region that can be treated by applying perturbation theory is not relevant for nuclear physics. The nuclear interaction is the residual strong force between color-neutral nucleons. It shows some analogy to the van der Waals force, which is the residual electromagnetic force between electrically neutral atoms or molecules.

In nuclear physics the relevant degrees of freedom are the nucleons. The interaction is mediated by mesons. Due to the fact that in QCD a nucleon is a very complex many-body system and the gluons can also interact with themselves it is far from easy to get to this description by starting from QCD. Deriving the nuclear interaction is one of the aims of lattice QCD, but results that can compete with recent realistic interactions cannot be expected in the near future. Since the nucleus is a very complex many-body system it is also not possible to directly derive the potential from experimentally known nuclear structure.

Chiral perturbation theory (χ -PT) [EM02, EM03, EGM05, Epe06] is a promising candidate for an effective theory that might lead to a nuclear interaction based on the low-energy region of QCD. Responsible for the name is the assumption that chiral symmetry is fulfilled, e.g. the left-handed and right-handed parts of Dirac fields transform independently. Another approximation is omitting higher

2.2 Unitary Correlation Operator Method

terms coming from power counting schemes used in the expansion around light quark masses.

In general realistic potentials are derived from the most general interaction possible under the stipulated symmetries. For the long-range behavior the pion-exchange is included. The terms are fitted to the high-precision data from nucleon-nucleon elastic scattering. The most widely applied nucleon-nucleon potentials are at the moment the Argonne V18, CD Bonn, Nijmegen and Paris potentials.

The realistic interaction that is the basis for the interaction used in this work is the Argonne V18 potential [WSS95]. The AV18 is dominated by a charge-independent term and additional charge-dependent and charge-symmetry-breaking terms. The short- and medium-range behavior of this interaction does not come from a meson-exchange description but shows a phenomenological operator structure. 4301 pp and pn scattering data points, low-energy nn scattering parameters and the properties of the deuteron were used to fit it. A χ^2 of 1.09 per datum was obtained.

The AV18 potential also shows the basic properties of the nuclear two-body interaction. One of these properties is a strong repulsion, the so-called *hard core* at small relative distances. Another one is the existence of a minimum in the potential in at least one of the channels at ≈ 1 fm. This minimum has to be deep enough to compensate the Coulomb repulsion of protons. For distances greater than ≈ 2 fm the interaction soon becomes negligibly small. The nuclear potential also shows strong spin-dependence and a tensor term that mixes different orbital angular momenta.

The bare Argonne V18 potential cannot be used in most applications as the convergence with the size of the Hilbert space is too slow.

2.2 Unitary Correlation Operator Method

The Unitary Correlation Operator Method (UCOM) is used to treat the strong short-range central and tensor correlations [FNRS98, NF03, RHP⁺05]. These correlations are induced by the repulsive core and the tensor force in the nuclear interaction. By definition they cannot be described by product states like Slater determinants. The unitary transformation has a finite range thus the resulting effective nucleon-nucleon potential is phase-shift equivalent to the original one.

A unitary operator is an operator \tilde{C} that fulfills the following condition:

$$\tilde{C}^\dagger \tilde{C} = \mathbb{1}. \quad (2.1)$$

By applying the unitary correlation operator \tilde{C} to a state $|\Psi\rangle$ the correlated

state $|\widehat{\Psi}\rangle$ is obtained:

$$|\widehat{\Psi}\rangle = \underline{\underline{C}}|\Psi\rangle. \quad (2.2)$$

Matrix elements can be calculated either using the correlated state $|\widehat{\Psi}\rangle$ or the correlated operator $\widehat{A} = \underline{\underline{C}}^\dagger \underline{\underline{A}} \underline{\underline{C}} = \underline{\underline{C}}^{-1} \underline{\underline{A}} \underline{\underline{C}}$

$$\langle \widehat{\Psi}' | \widehat{A} | \widehat{\Psi} \rangle = \langle \Psi' | \underline{\underline{C}}^\dagger \underline{\underline{A}} \underline{\underline{C}} | \Psi \rangle = \langle \Psi' | \widehat{A} | \Psi \rangle. \quad (2.3)$$

The idea behind this method is to choose the unitary correlation operator in a way to transform many-body states that cannot represent short range two-body correlations, like the shell model states or the FMD basis states, into new states that are better adapted to the interaction. In this work the correlation operator is applied to the Hamiltonian to obtain a correlated effective Hamiltonian.

To derive the typical correlation for the nucleon-nucleon interaction the correlation operator is decomposed into a product of the radial correlator $\underline{\underline{C}}_r$ and the tensor correlator $\underline{\underline{C}}_\Omega$

$$\underline{\underline{C}} = \underline{\underline{C}}_\Omega \underline{\underline{C}}_r. \quad (2.4)$$

The ansatz for these unitary correlators

$$\underline{\underline{C}}_r = \exp \left\{ -i \sum_{i < j} g_{r,ij} \right\} \quad (2.5)$$

$$\underline{\underline{C}}_\Omega = \exp \left\{ -i \sum_{i < j} g_{\Omega,ij} \right\} \quad (2.6)$$

involves the hermitian two-body generators $g_{r,ij}$ for the radial correlator and $g_{\Omega,ij}$ for the tensor correlator, respectively.

The radial correlator

The radial correlator was introduced to represent the correlations induced by the short ranged repulsive core in the realistic nucleon-nucleon potential. In UCOM this is done by shifting a pair of nucleons away from each other if they are inside the repulsive region. The appropriate generator of the radial correlator $\underline{\underline{C}}_r$ is chosen to be

$$\underline{\underline{g}}_{r,ij} = \frac{1}{2} \left(\underline{\underline{p}}_{r,ij} s(\underline{\underline{r}}_{ij}) + s(\underline{\underline{r}}_{ij}) \underline{\underline{p}}_{r,ij} \right). \quad (2.7)$$

Where

$$\tilde{p}_r = \frac{1}{2} \left\{ \tilde{\vec{p}} \cdot \frac{\tilde{\vec{r}}}{r} + \frac{\tilde{\vec{r}}}{r} \cdot \tilde{\vec{p}} \right\} \Rightarrow \frac{1}{i} \left(\frac{1}{r} + \frac{\partial}{\partial r} \right) \quad (2.8)$$

is the relative radial momentum operator and $s(r_{ij})$ is the shift function or radial correlation function. The shift is largest at short distances and vanishes for large distances. Since the shift depends on the repulsive core of the potential the shape of $s(r_{ij})$ is adapted to the interaction. Details about the radial correlator can be found in [FNRS98].

The tensor correlator

The tensor operator

$$S_{12} = 3(\tilde{\sigma}_1 \hat{r}_{12})(\tilde{\sigma}_2 \hat{r}_{12}) - (\tilde{\sigma}_1 \tilde{\sigma}_2) = 6(\tilde{S} \hat{r}_{12})^2 - 2\tilde{S}^2 \quad (2.9)$$

describes the tensor force in the $S = 1$ channels of the interaction. It depends on the spins $\tilde{S} = \frac{1}{2}(\tilde{\sigma}_1 + \tilde{\sigma}_2)$ and the direction of the spacial orientation $\hat{r}_{12} = (\vec{r}_1 - \vec{r}_2)/(|\vec{r}_1 - \vec{r}_2|)$ of the two interacting nucleons.

To consider the correlations induced by the angular dependent tensor force a spin-dependent shift of the two nucleons perpendicular to their distance vector is needed.

The ansatz for the generator of the tensor correlator is

$$g_{\Omega_{ij}} = \frac{3}{2} \vartheta(r_{ij}) \left((\tilde{\sigma}_i \cdot \tilde{\vec{p}}_{\Omega_{ij}})(\tilde{\sigma}_j \cdot \tilde{\vec{r}}_{ij}) + (\tilde{\sigma}_i \cdot \tilde{\vec{r}}_{ij})(\tilde{\sigma}_j \cdot \tilde{\vec{p}}_{\Omega_{ij}}) \right). \quad (2.10)$$

Where $\tilde{\vec{p}}_{\Omega_{ij}} = \tilde{\vec{p}}_{ij} - \tilde{\vec{p}}_{r_{ij}}$ is the orbital part of the relative momentum operator. The strength and range of the tensor correlator is defined by choosing the tensor correlation function $\vartheta(r_{ij})$ appropriately [NF03].

The correlated potential V_{UCOM}

By applying the correlator to the Hamiltonian one obtains the correlated Hamiltonian \hat{H}_e

$$\hat{H}_e = \tilde{C}^\dagger H \tilde{C} = \sum_i \tilde{C}^\dagger T_i \tilde{C} + \sum_{i < j} \tilde{C}^\dagger V_{ij} \tilde{C} \quad (2.11)$$

As the generators in the exponent of the correlators (2.5) are two-body operators a series of n-body operators is generated

$$\sum_i \tilde{C}^\dagger T_i \tilde{C} = \sum_i T_i + \sum_{i < j} \hat{T}_{ij}^{[2]} + \sum_{i < j < k} \hat{T}_{ijk}^{[3]} + \dots \quad (2.12)$$

$$\sum_{i < j} \tilde{C}^\dagger V_{ij} \tilde{C} = \sum_{i < j} \hat{V}_{ij}^{[2]} + \sum_{i < j < k} \hat{V}_{ijk}^{[3]} + \dots \quad (2.13)$$

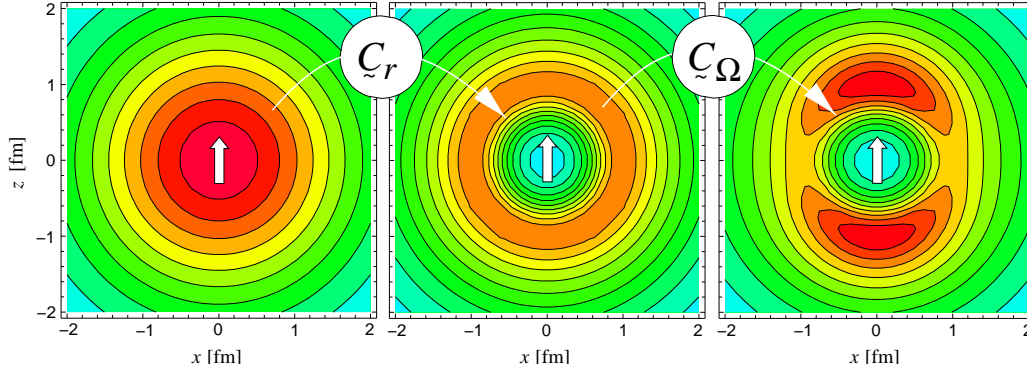


Figure 2.1: Effect of the radial and tensor correlation operator in the case of ${}^4\text{He}$. Shown is the two-body density in dependence on the relative distance $\vec{r}_1 - \vec{r}_2$ of two nucleons $\rho_{S=1, T=0}^{[2]}(\vec{r}_1 - \vec{r}_2)$. This Figure has been taken from [NF03]

The $^{[n]}$ indicates an irreducible n -body operator. If the range of the correlations is small compared to the mean particle distance three- and more-body terms will contribute little. Therefore the two-body approximation of the correlated Hamiltonian

$$\widehat{H} \approx \sum_i \widehat{T}_i + \sum_{i<j} \widehat{T}_{ij}^{[2]} + \sum_{i<j} \widehat{V}_{ij}^{[2]} \quad (2.14)$$

is used. It only consists of one- and two-body operators. In order to keep three- and higher-body terms small the range of the correlation functions $s(r)$ and $\vartheta(r)$ has to be chosen smaller than the mean particle distance.

Like the Hamiltonian all other correlated operators are also truncated at the two-body level.

Besides the three-body forces induced by the correlator there are also three-body forces arising in microscopic derivations of the nucleon-nucleon force [EM02, EM03, EGM05, Epe06]. Those are not unique and depend on the chosen two-body force. The contributions of many-body forces are minimized in the UCOM approach by adjusting the range of the tensor correlator. It has been observed that variations in the range of the tensor correlator result in binding energies for the ${}^3\text{He}$ and ${}^4\text{He}$ system that follow the so-called Tjon line which comes very close to the experimental values [NKG00, RHP⁺05]. The range is fixed at the point where the experimental ${}^3\text{He}$ and ${}^4\text{He}$ binding energies are reproduced best.

The two-body part of the approximated correlated Hamilton operator is called V_{UCOM}

$$V_{\text{UCOM}} = \widehat{T}^{[2]} + \widehat{V}^{[2]} \quad (2.15)$$

The correlated interaction does not show the strong local repulsion but a strong momentum dependence is introduced. Most of the tensor force is transformed into

the central part of the correlated interaction. As an effect the UCOM interaction is pre-diagonalized for the used Hilbert spaces.

It is possible to express the obtained interaction V_{UCOM} in operator representation again [NF08]. The UCOM interaction

$$\tilde{V}_{\text{UCOM}} = \sum_T (\tilde{V}_c^T + \tilde{V}_{ls}^T + \tilde{V}_t^T) \quad (2.16)$$

consists of a radial term

$$\tilde{V}_c^T = \sum_S \left(\hat{V}_c^{ST}(r) + \frac{1}{2} \left(\tilde{p}_r^2 \hat{V}_{p^2}^{ST}(r) + \hat{V}_{p^2}^{ST}(r) \tilde{p}_r^2 \right) + \hat{V}_{\tilde{l}^2}^{ST}(r) \tilde{l}^2 \right), \quad (2.17)$$

a spin-orbit term

$$\tilde{V}_{ls}^T = \hat{V}_{ls}^T(r) \tilde{l} \cdot \tilde{s} + \hat{V}_{\tilde{l}^2}^T(r) \tilde{l}^2 \tilde{l} \cdot \tilde{s} \quad (2.18)$$

and a tensor term

$$\begin{aligned} \tilde{V}_t^T = & \hat{V}_{\tilde{l}\tilde{l}}^T(r) S_{12}(\tilde{l}, \tilde{l}) + \hat{V}_t^T(r) S_{12}(\vec{r}, \vec{r}) + \hat{V}_{\tilde{l}p\Omega}^T(r) S_{12}(\tilde{p}_\Omega, \tilde{p}_\Omega) \\ & + \hat{V}_{\tilde{l}^2 r p\Omega}^T(r) \tilde{l}^2 S_{12}(\tilde{p}_\Omega, \tilde{p}_\Omega). \end{aligned} \quad (2.19)$$

Here in addition to terms present in the bare interaction new momentum dependent terms appear.

FMD corrections

In the FMD model space medium-range correlations are not fully described. To account for this, the range of the tensor correlator is enlarged to make the effective interaction more attractive. An additional phenomenological correction term is added. It contains momentum dependent central parts and a spin-orbit interaction.

The parameters of the correction term are fitted to the binding energies and radii of the double-magic nuclei ${}^4\text{He}$, ${}^{16}\text{O}$, ${}^{40}\text{Ca}$, ${}^{24}\text{O}$, ${}^{34}\text{Si}$ and ${}^{48}\text{Ca}$. A typical contribution of the correction term is 15% of the original V_{UCOM} . However, by now it is known that the chosen corrections in the interaction used throughout this work cause a spin-orbit splitting which is too large. More elaborate Hilbert spaces such as spaces containing the VAP states introduced in subsection 4.1.3 on page 35 can lead to overbinding. Due to these known imperfections of the interaction work on an improved interaction including FMD corrections is currently in progress.

An important numerical issue when using a nonorthogonal basis such as in FMD (3.4) is the consistent calculation of matrix elements of the Hamiltonian and the overlap matrix (3.9). Therefore all FMD matrix elements are calculated analytically. In order to do this radial dependencies of the interaction are represented by sums of Gaussians, since the analytical solutions of the necessary integrals is available.

Fermionic Molecular Dynamics

3.1 The Hilbert Space

3.1.1 Single-particle states

The relevant degrees of freedom that were chosen for FMD are the nucleons. The single-particle Hilbert space consist of a spatial part, a spin part and an isospin part:

$$\mathcal{H}_{\text{sp}} = \mathcal{H}_{\text{Space}} \otimes \mathcal{H}_{\text{Spin}} \otimes \mathcal{H}_{\text{Isospin}} \quad (3.1)$$

In FMD $\mathcal{H}_{\text{Space}}$ is spanned by single-particle states in phase-space. Heisenberg's uncertainty principle $\Delta r \Delta p \geq \frac{\hbar}{2}$ becomes $\Delta r \Delta p = \frac{\hbar}{2}$ for a Gaussian wave packet with a real width parameter. Thus this choice is very descriptive since it is the closest quantum mechanical analog to the mass point used in classical mechanics.

In coordinate space representation the localized FMD single-particle state are of Gaussian shape

$$\langle \vec{x} | a_l, \vec{b}_l \rangle = \exp \left\{ -\frac{(\vec{x} - \vec{b}_l)^2}{2a_l} \right\} \quad (3.2)$$

and will be called Gaussian in the following. The parameters a_l and \vec{b}_l are the complex width and the complex position of the center of the Gaussian in phase-space. The real part of a_l has to be positive and must not be zero.

The imaginary part of \vec{b}_l is related to the velocity and the imaginary part of a_l to the change of the width in time. a_l and b_l are related to the mean position $\vec{\rho}_{ll}$ and the mean momentum $\vec{\pi}_{ll}$ [FS00] as defined in (A.5) and (A.6) on page 95:

3.1 The Hilbert Space

$$\vec{b}_l = \vec{\rho}_l + ia_l \vec{\pi}_l \quad (3.3)$$

These Gaussians span the complete Hilbert space $\mathcal{H}_{\text{Space}}$ and serve as basis states that are neither orthogonal nor normalized. Their overlap is given by

$$R_{kl} = \langle a_k, \vec{b}_k | a_l, \vec{b}_l \rangle = \left(2\pi \frac{a_k^* a_l}{a_k^* + a_l} \right)^{\frac{3}{2}} \exp \left\{ -\frac{(\vec{b}_k^* - \vec{b}_l)^2}{2(a_k^* + a_l)} \right\} \quad (3.4)$$

The Spin-Hilbert-Space $\mathcal{H}_{\text{Spin}}$ is spanned by the most general two-spinor for the parametrization of a non-relativistic spin $\frac{1}{2}$ fermion:

$$|\chi_l^\uparrow, \chi_l^\downarrow\rangle = \chi_l^\uparrow |\uparrow\rangle + \chi_l^\downarrow |\downarrow\rangle \quad (3.5)$$

χ_l^\uparrow and χ_l^\downarrow are the complex amplitudes for the orthonormalized spin $\frac{1}{2}$ basis states $|\uparrow\rangle$ and $|\downarrow\rangle$. $|\uparrow\rangle$ and $|\downarrow\rangle$ are the eigenstates of the third component of the spin operator S_3 . The spin overlap is

$$S_{kl} = \langle \chi_k^\uparrow, \chi_k^\downarrow | \chi_l^\uparrow, \chi_l^\downarrow \rangle = \chi_k^{\uparrow*} \chi_l^\uparrow + \chi_k^{\downarrow*} \chi_l^\downarrow \quad (3.6)$$

The isospin space is parametrized by the 3-component of the isospin: ξ_k , which is here $1/2$ for a proton and $-1/2$ for a neutron. The isospin overlap is:

$$T_{kl} = \langle \xi_k | \xi_l \rangle = \frac{1}{2} + 2\xi_k \xi_l \quad (3.7)$$

T_{kl} is either 1 if particles k and l have the same isospin or 0 if one particle is a proton and the other a neutron. A more general description that involves isospin projection is used in [BFN08]. It is not applied in this work.

In general more than one Gaussian is used for an improved description of nuclear single-particle states. This is especially useful in the description of halo states¹ since their radial density distribution falls off like an exponential and not like a Gaussian. This can be represented much better by a sum of Gaussians.

¹A halo state (or nucleus) is a state in which one or more nucleons are widely distributed and show a rather large probability to be outside the core. This can happen in nuclear systems if one or more nucleons are loosely bound. It also results in a dramatically increased radius. Neutron halos have been found in neutron-rich nuclei close to the neutron drip line and proton halos can be found in proton-rich nuclei close to the proton drip line.

The general single-particle state is given by

$$|q_l\rangle = \sum_{j=1}^m c_{lj} |a_{lj}, \vec{b}_{lj}\rangle \otimes |\chi_{lj}^\uparrow, \chi_{lj}^\downarrow\rangle \otimes |\xi_l\rangle \quad (3.8)$$

The choice of Gaussian basis states has various advantages. The most obvious advantage is that they can be freely placed in phase space and hence easily depict cluster states. As their width is a free parameter and they are a sum of several displaced Gaussians with different width, FMD basis states are more flexible to describe halo states.

Another obvious property of the choice of FMD single-particle basis states is that they are Gaussian such as the s states of a shell model description in a harmonic oscillator. Not so trivial is the fact that linear combinations of slightly displaced Gaussians with the same width parameter a are after antisymmetrization the harmonic oscillator s and p states in the limit where the difference of their centers $\vec{b}_1 - \vec{b}_2$ vanishes.

If more Gaussians are used this is also true for higher shells. Thus the shell model states are already incorporated in the FMD Hilbert space.

The overlap of two Gaussian states is just the product of the space, spin and isospin overlaps R_{kl} , S_{kl} and T_{kl} , respectively. While for single-particle states that are superpositions of more than one Gaussian the overlap becomes:

$$n_{kl} = \langle q_k | q_l \rangle = \sum_{j_k=1}^{m_k} \sum_{j_l=1}^{m_l} c_{kj_k}^* c_{lj_l} R_{kj_k, lj_l} S_{kj_k, lj_l} T_{kj_k, lj_l} . \quad (3.9)$$

The complex coefficients $c_{kj_k}^* c_{lj_l}$ are not used in the code. They are incorporated into the spin amplitudes χ_l^\uparrow and χ_l^\downarrow .

FMD was initially developed to describe heavy-ion reactions in a time-dependent picture. In this work only stationary solutions are considered where the time-dependence resides only in the phase.

3.1.2 Many-body states

The FMD many-body states are expressed in terms of Slater determinants which are antisymmetrized Kronecker products of the single-particle states:

$$|Q\rangle = \mathcal{A} |q_1\rangle \otimes |q_2\rangle \otimes \dots \otimes |q_A\rangle \quad (3.10)$$

\mathcal{A} is the antisymmetrization operator and is chosen to be a projection operator i.e.: $\mathcal{A}\mathcal{A} = \mathcal{A}$ and $\mathcal{A} = \mathcal{A}^\dagger$.

3.1 The Hilbert Space

$$|Q\rangle = \frac{1}{A!} \sum_{\text{all } \rho} \text{sgn}(\rho) |q_{\rho(1)}\rangle \otimes |q_{\rho(2)}\rangle \otimes \dots \otimes |q_{\rho(A)}\rangle \quad (3.11)$$

The sum includes all the possible $A!$ permutations ρ . The sign function $\text{sgn}(\rho)$ is -1 if ρ contains an odd number of transpositions and $+1$ otherwise.

The set of parameters that describe a many-body state $|Q\rangle$ is

$$Q = \{q_1, q_2, \dots, q_A\} . \quad (3.12)$$

It consists of sets which contain the parameters of the single-particle states.

Matrix elements

The overlap of the two Slater determinants $|Q^{(a)}\rangle$ and $|Q^{(b)}\rangle$ is

$$\langle Q^{(a)} | Q^{(b)} \rangle = \frac{1}{A!} \det(n^{ab}) \quad (3.13)$$

with the overlap matrix elements n_{kl}^{ab} between different single particle states represented by (a) and (b)

$$n_{kl}^{ab} = \langle q_k^a | q_l^b \rangle . \quad (3.14)$$

The inverse overlap matrix o^{ab} is:

$$o_{lk}^{ab} = \left((n^{ab})^{-1} \right)_{lk} . \quad (3.15)$$

Like n_{kl}^{ab} o_{lk}^{ab} depends on two sets of parameters $Q^{(a)}$ and $Q^{(b)}$ (3.10). The elements of the set Q that represents the Slater determinant $|Q\rangle$ are the sets q that represent the single-particle states $|q\rangle$ (3.8). These depend on the parameters of the single-particle states (3.8). These parameters a , \vec{b} , χ^\uparrow and χ^\downarrow in the set q_m are called q_μ ($\mu = (m, i)$).

The deduction of the derivative of the inverse overlap matrix

$$\frac{\partial o_{lk}^{ab}}{\partial q_\mu^{a*}} = -o_{lm}^{ab} \sum_j \left(\frac{\partial}{\partial q_\mu^{a*}} \langle q_m^a | q_j^b \rangle \right) o_{jk}^{ab} . \quad (3.16)$$

can be found in [Nef98].

A many-body matrix element of an one-body operator is given by

$$\frac{\langle Q^{(a)} | \tilde{A}^{[1]} | Q^{(b)} \rangle}{\langle Q^{(a)} | Q^{(b)} \rangle} = \sum_{kl} \langle q_k^a | \tilde{a} | q_l^b \rangle o_{lk}^{ab} . \quad (3.17)$$

where \tilde{a} acts in one-body space. For a two-body operator $\tilde{A}^{[2]}$ using the two-body matrix elements the many-body matrix element is given by

$$\frac{\langle Q^{(a)} | \tilde{A}^{[2]} | Q^{(b)} \rangle}{\langle Q^{(a)} | Q^{(b)} \rangle} = \frac{1}{2} \sum_{klrs} \langle q_k^a, q_l^a | \tilde{a} | q_r^b, q_s^b \rangle (o_{rk}^{ab} o_{sl}^{ab} - o_{sk}^{ab} o_{rl}^{ab}). \quad (3.18)$$

where the operator \tilde{a} acts now in the two-body space only. The occurrence of four inverse overlap matrices in the two-body matrix elements is due to antisymmetrization.

To enable the minimization routine to find the correct direction for the minimization the gradients of the involved functions are needed. The gradient of a one-body matrix element is evaluated as follows:

$$\begin{aligned} \frac{\partial}{\partial q_\mu^{a*}} \frac{\langle Q^{(a)} | \tilde{A}^{[1]} | Q^{(b)} \rangle}{\langle Q^{(a)} | Q^{(b)} \rangle} &= \sum_{kl} \frac{\partial}{\partial q_\mu^{a*}} (\langle q_k^a | \tilde{a} | q_l^b \rangle o_{lk}^{ab}) \\ &= \sum_l \left[\frac{\partial \langle q_m^a | \tilde{a} | q_l^b \rangle}{\partial q_\mu^{a*}} \right. \\ &\quad \left. - \sum_{vw} \left(\frac{\partial \langle q_m^a | q_v^b \rangle}{\partial q_\mu^{a*}} \right) o_{vw}^{ab} \langle q_w^a | \tilde{a} | q_l^b \rangle \right] o_{lm}^{ab} \end{aligned} \quad (3.19)$$

$\frac{\partial}{\partial q_\mu^{a*}} \langle q_m^a | \tilde{a} | q_l^b \rangle$ has to be evaluated depending on the operator \tilde{a} which can be found in section 4.5. All other terms of the gradient can be immediately calculated from the parameters q_k . The gradient of a two-body matrix element

$$\begin{aligned} \frac{\partial}{\partial q_\mu^{a*}} \frac{\langle Q^{(a)} | \tilde{A}^{[2]} | Q^{(b)} \rangle}{\langle Q^{(a)} | Q^{(b)} \rangle} &= \frac{1}{2} \sum_{klrs} \frac{\partial}{\partial q_\mu^{a*}} [\langle q_k^a, q_l^a | \tilde{a} | q_r^b, q_s^b \rangle (o_{rk}^{ab} o_{sl}^{ab} - o_{sk}^{ab} o_{rl}^{ab})] \\ &= \sum_{lrs} \left[\frac{\partial}{\partial q_\mu^{a*}} \langle q_m^a, q_l^a | \tilde{a} | q_r^b, q_s^b \rangle \right. \\ &\quad \left. - \sum_{vw} \left(\frac{\partial}{\partial q_\mu^{a*}} \langle q_m^a | q_v^b \rangle \right) o_{vw}^{ab} \langle q_w^a, q_l^a | \tilde{a} | q_r^b, q_s^b \rangle \right] \\ &\quad (o_{rm}^{ab} o_{sl}^{ab} - o_{sm}^{ab} o_{rl}^{ab}). \end{aligned} \quad (3.20)$$

shows the same property: only $\frac{\partial}{\partial q_\mu^{a*}} \langle q_w^a, q_l^a | \tilde{a} | q_r^b, q_s^b \rangle$ needs to be given for each operator while the other terms depend only on the parameters of the Slater determinant but not on the operator.

Symmetries

The nuclear Hamilton operator obeys certain symmetries such as mirror, translational, rotational or time-reversal symmetry. These symmetries are also sym-

metries of its eigenstates. In general the FMD Slater determinants $|Q\rangle$ are not eigenstates of the corresponding symmetry operators. Therefore they are projected on parity, angular momentum and center of mass momentum to fulfill the corresponding symmetry properties. A projection on correct behavior in terms of time-reversal symmetry has yet not been implemented.

Parity

The parity operator $\tilde{\Pi}$ mirrors a state at the origin of the coordinate frame. Whenever parameters of a parity projected state are varied to find a minimum in the energy surface the constraints $\langle \tilde{X}^{\text{CM}} \rangle = 0$ and $\langle \tilde{K}^{\text{CM}} \rangle = 0$ are demanded. This is done to avoid spurious center of mass motion. Details about this procedure can be found in subsection 4.5.1 on page 43.

In the FMD case the parity transformation is just a change of the signs of all the parameters \vec{b}

$$\tilde{\Pi}(|a, \vec{b}\rangle \otimes |\chi\rangle \otimes |\xi\rangle) = |a, -\vec{b}\rangle \otimes |\chi\rangle \otimes |\xi\rangle. \quad (3.21)$$

The projection operator for positive parity $\pi = +1$ or negative parity $\pi = -1$ is

$$\tilde{P}^\pi = \frac{1}{2} (1 + \pi \tilde{\Pi}). \quad (3.22)$$

Center of mass momentum

The translation operator $\exp\{-i\tilde{K}^{\text{CM}} \cdot \vec{X}\}$ translates a state by the vector \vec{X} . The center of mass projection

$$\tilde{P}^{\text{CM}} = \frac{1}{(2\pi)^3} \int d^3X \exp\{-i\tilde{K}^{\text{CM}} \cdot \vec{X}\} = \delta^3(\tilde{K}^{\text{CM}}) \quad (3.23)$$

is a projection on the eigenstate with momentum zero of the total momentum

$$\text{operator } \tilde{K}^{\text{CM}} = \sum_{i=1}^A \tilde{k}_i.$$

In this work two methods of the center of mass projection are used. The first is a numerical evaluation on 100 points. The second is an analytical solution where the center of mass and the intrinsic motion are factorized. This is called approximate center of mass projection since the analytical solution is only correct if all width parameters a of all single-particle states are identical.

Orbital angular momentum

The rotation operator

$$\tilde{R}(\alpha, \beta, \gamma) = \exp\{-i\alpha \tilde{J}_z\} \exp\{-i\beta \tilde{J}_y\} \exp\{-i\gamma \tilde{J}_z\} \quad (3.24)$$

performs the most general rotation by the Euler angles α, β and γ . The generators of these rotations are the angular momentum operators \underline{J}_z and \underline{J}_y .

Acting on a FMD state

$$\underline{R}(\alpha, \beta, \gamma) (|a, \vec{b}\rangle \otimes |\chi\rangle \otimes |\xi\rangle) = |a, R_3(\alpha, \beta, \gamma) \cdot \vec{b}\rangle \otimes \underline{R}^{\frac{1}{2}}(\alpha, \beta, \gamma) |\chi\rangle \otimes |\xi\rangle \quad (3.25)$$

the rotation operator is expressed by the matrix representation of the three dimensional rotation group SO(3)

$$R_3(\alpha, \beta, \gamma) = \begin{pmatrix} c_\alpha c_\beta c_\gamma - s_\alpha s_\gamma & -c_\alpha c_\beta s_\gamma - s_\alpha c_\gamma & c_\alpha s_\beta \\ s_\alpha c_\beta c_\gamma + c_\alpha s_\gamma & -s_\alpha c_\beta s_\gamma + c_\alpha c_\gamma & s_\alpha s_\beta \\ -s_\beta c_\gamma & s_\beta s_\gamma & c_\beta \end{pmatrix} \quad (3.26)$$

acting on \vec{b} and the two dimensional matrix representation of the SU(2) Lie group

$$\underline{R}^{\frac{1}{2}}(\alpha, \beta, \gamma) = \exp\left\{-\frac{i}{2}\alpha\sigma_z\right\} \exp\left\{-\frac{i}{2}\beta\sigma_y\right\} \exp\left\{-\frac{i}{2}\gamma\sigma_z\right\} \quad (3.27)$$

acting only in spin space. The notation used in (3.26) is a compact form where c and s are the cosine and sine functions and the index α, β or γ is the argument of the trigonometric function (details can be found in [EG70] or [Ros57]). σ_z and σ_y are two of the Pauli matrices which together with σ_x are the generators of the SU(2) Lie group. The matrix representation of $\underline{R}^{\frac{1}{2}}(\alpha, \beta, \gamma)$ in the basis:

$$|\uparrow\rangle = \begin{pmatrix} 1 \\ 0 \end{pmatrix}, \quad |\downarrow\rangle = \begin{pmatrix} 0 \\ 1 \end{pmatrix} \quad (3.28)$$

is

$$\underline{R}^{\frac{1}{2}}(\alpha, \beta, \gamma) = \begin{pmatrix} \cos(\frac{\beta}{2}) e^{-\frac{i}{2}(\alpha+\gamma)} & -\sin(\frac{\beta}{2}) e^{-\frac{i}{2}(\alpha-\gamma)} \\ \sin(\frac{\beta}{2}) e^{\frac{i}{2}(\alpha-\gamma)} & \cos(\frac{\beta}{2}) e^{\frac{i}{2}(\alpha+\gamma)} \end{pmatrix}. \quad (3.29)$$

The angular momentum projection operator

$$\underline{P}_{MK}^J = \frac{2J+1}{8\pi^2} \int d\alpha \int \sin\beta d\beta \int d\gamma D_{MK}^{J*}(\alpha, \beta, \gamma) \underline{R}(\alpha, \beta, \gamma) \quad (3.30)$$

$$\underline{P}_{MK}^J = \frac{2J+1}{8\pi^2} \int d^3\Omega D_{MK}^{J*}(\vec{\Omega}) \underline{R}(\vec{\Omega}) \quad (3.31)$$

is a superposition of all possible rotations $\underline{R}(\alpha, \beta, \gamma)$. The weights of the rotated states are the Wigner D-functions

$$D_{MK}^J(\alpha, \beta, \gamma) = \langle JM | \underline{R}(\alpha, \beta, \gamma) | JK \rangle = e^{-iM\alpha} d_{MK}^J(\beta) e^{-iK\gamma} \quad (3.32)$$

3.2 The many-body basis

with the Wigner d-functions

$$d_{MK}^J(\beta) = \langle JM | e^{-i\beta J_y} | JK \rangle . \quad (3.33)$$

The angular momentum projection operator is not a projection operator in the strict mathematical sense [RS00]; it only fulfills the property

$$\left(P_{MK}^J \right)^\dagger P_{M'K'}^{J'} = \delta_{JJ'} \delta_{MM'} P_{KK'}^J \quad (3.34)$$

which is used to reduce the numerical effort for calculating matrix elements of tensor operators.

As an abbreviation the following operator is used for angular momentum and parity projection

$$P_{MK}^{J\pi} := P_{MK}^J P^\pi . \quad (3.35)$$

By applying the parity, center of mass and angular momentum projection on the state $|Q^{(a)}\rangle$ the projected state with a sharp K

$$|Q^{(a)}; J^\pi MK\rangle := P_{MK}^{J\pi} P^{\text{CM}} |Q^{(a)}\rangle \quad (3.36)$$

is obtained.

K-mixing

Depending on the symmetries of the system the K quantum number is generally not a good quantum number for eigenstates of the Hamiltonian, therefore the so-called K -mixing procedure is performed

$$|Q^{(a)}; J^\pi M; \kappa_a\rangle = \sum_{K=-J}^J C_K^{(a, \kappa_a)} |Q^{(a)}; J^\pi MK\rangle ; \quad \kappa_a = 1, \dots, n^{(a)} . \quad (3.37)$$

The $C_K^{(a, \kappa_a)}$ are obtained by solving the eigenvalue problem for the intrinsic Hamiltonian \tilde{H} in the subspace spanned by $|Q^{(a)}; J^\pi MK\rangle$ where $K = -J, -J+1, \dots, J-1, J$. This diagonalization is performed as a singular value decomposition (SVD). The SVD excludes states that are very similar. Additionally the eigenstates with insignificant norms are not used.

3.2 The many-body basis

The many body Hilbert space for given angular momentum J and intrinsic parity π is spanned by $|Q^{(a)}; J^\pi M; \kappa_a\rangle$. For the sake of a more compact notation the following abbreviations are introduced:

$$\mathbf{N}_{(a,\kappa_a),(b,\kappa_b)}^{J^\pi} := \langle Q^{(a)}; J^\pi M; \kappa_a | Q^{(b)}; J^\pi M; \kappa_b \rangle \quad (3.38)$$

$$\mathbf{H}_{(a,\kappa_a),(b,\kappa_b)}^{J^\pi} := \langle Q^{(a)}; J^\pi M; \kappa_a | \tilde{H} | Q^{(b)}; J^\pi M; \kappa_b \rangle \quad (3.39)$$

$$\mathbf{A}_{(a,\kappa_a),(b,\kappa_b)}^{J^\pi} := \langle Q^{(a)}; J^\pi M; \kappa_a | \tilde{A} | Q^{(b)}; J^\pi M; \kappa_b \rangle \quad (3.40)$$

An inverse overlap matrix is also defined in the many-body basis:

$$\mathbf{O}_{(a,\kappa_a),(b,\kappa_b)}^{J^\pi} := \left(\mathbf{N}_{(a,\kappa_a),(b,\kappa_b)}^{J^\pi} \right)^{-1} \quad (3.41)$$

to be able to express a projection operator on this subspace

$$\tilde{\mathbb{1}}^{J^\pi} = \sum_{a,b} \sum_{\kappa_a, \kappa_b} | Q^{(a)}; J^\pi M; \kappa_a \rangle \mathbf{O}_{(a,\kappa_a),(b,\kappa_b)}^{J^\pi} \langle Q^{(b)}; J^\pi M; \kappa_b |. \quad (3.42)$$

For every J^π the energy eigenvalue equation

$$\sum_j \mathbf{H}_{ij} \Psi_j^\alpha = E_\alpha \sum_j \mathbf{N}_{ij} \Psi_j^\alpha \quad (3.43)$$

is to be solved. Here the index $i = (a, \kappa_a)$ represents all combinations of the values a and κ_a and likewise $j = (b, \kappa_b)$. Again a singular value decomposition is applied. Additionally eigenstates with a norm

$$\left| \frac{\langle Q; J^\pi M; \kappa | Q \rangle}{\sqrt{\langle Q; J^\pi M; \kappa | Q; J^\pi M; \kappa \rangle \langle Q | Q \rangle}} \right| \quad (3.44)$$

below a certain threshold are also eliminated to avoid numerical imprecisions.

Chapter4

Many-Body Hilbert-Space

4.1 Ritz variation

Starting from the functional

$$E[\Phi] = \frac{\langle \Phi | \tilde{H} | \Phi \rangle}{\langle \Phi | \Phi \rangle} \geq E_0 \quad (4.1)$$

the energy can be calculated depending on the trial state $|\Phi\rangle$. The energy $E[\Phi]$ is either the ground state energy E_0 or higher. In general $|\Phi\rangle$ depends on a set of parameters $\Phi = \{\phi_1, \phi_2, \dots, \phi_n\}$. As an example these parameters could be the amplitudes ϕ_n of a state $|\Phi\rangle = \sum_n \phi_n |n\rangle$ in a given basis $|n\rangle$, but any other parameter set can also be used. In this work the FMD parameters $Q = \{q_1, q_2, \dots, q_A\}$ are used as variational parameters:

$$\delta \frac{\langle Q | \tilde{H} - \tilde{T}_{\text{CM}} | Q \rangle}{\langle Q | Q \rangle} = 0. \quad (4.2)$$

The isospins ξ_i are fixed throughout this work so they cannot be varied like in [BFN08].

The center of mass kinetic energy \tilde{T}_{CM} is subtracted. The remaining operator is called intrinsic Hamiltonian

$$\tilde{H}_{\text{int}} = \tilde{H} - \tilde{T}_{\text{CM}}. \quad (4.3)$$

The energy functional

$$E[Q] = \frac{\langle Q | \tilde{H}_{\text{int}} | Q \rangle}{\langle Q | Q \rangle} \quad (4.4)$$

is used for the variation in a mean-field or Hartree-Fock sense.

In Figure 4.1 proton and neutron densities of a Slater determinant are shown. The parameters of the Slater determinant were minimized without any projection. In all plots of intrinsic densities the nucleus is aligned such, that the largest principal moment of inertia of the nucleus is the z axis and the second largest is the y axis. The axes are always scaled from -9 to 9 fm. The densities are indicated by contour lines and the intensity of the color in the background. From the densities shown in Figure 4.1 it can be seen that the mean-field state is not an eigenstate of parity or angular momentum. The intrinsic energy of this state is -54.5 MeV. If projected on angular momentum the energy expectation values of this state becomes -42.1 MeV and -58.0 MeV, for the $J^\pi = 1/2^+$ and $J^\pi = 1/2^-$, respectively.

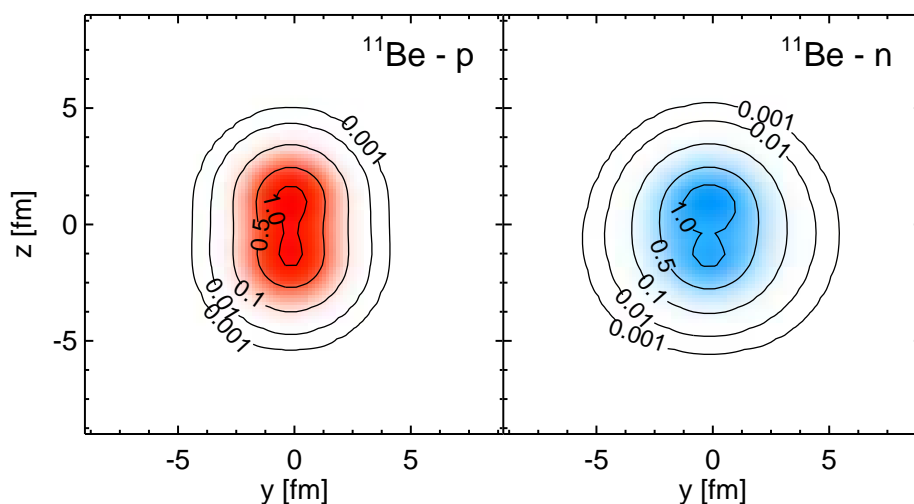


Figure 4.1: Example of the ^{11}Be state obtained by a minimization in the mean field sense. The densities shown are proton (l.h.s) and neutron (r.h.s.) point-densities in units of half the nuclear saturation density $\rho_0/2$.

The Hartree-Fock method might break certain symmetries of the Hamiltonian such as parity, rotational and translational symmetries. This can be seen in Figure 4.1 which shows densities of a ^{11}Be state whose parameters are adjusted in the Hartree-Fock sense. Since the densities are not spherically symmetric it can be seen that the state is not invariant under rotations.

4.1.1 Total parity

The Parity Operator $\tilde{\Pi}$ acting on a physical system performs a point reflection at the origin of the coordinate frame. Applying the parity operator $\tilde{\Pi}$ on the parity

projected state

$$|Q; \pi\rangle := \tilde{P}^\pi |Q\rangle = \frac{1}{2} (|Q\rangle + \pi \tilde{\Pi} |Q\rangle) \quad (4.5)$$

shows that $|Q; \pi\rangle$ is an eigenstate of $\tilde{\Pi}$ with the eigenvalue π :

$$\tilde{\Pi} |Q; \pi\rangle = \pi |Q; \pi\rangle. \quad (4.6)$$

Parity is a good quantum number:

$$[H, \tilde{\Pi}]_- = 0 \quad (4.7)$$

The energy functional for the parity projected state is

$$E^\pi [Q] = \frac{\langle Q | \tilde{H}_{\text{int}} \tilde{P}^\pi | Q \rangle}{\langle Q | \tilde{P}^\pi | Q \rangle} \quad (4.8)$$

$$= \frac{\langle Q | \tilde{H}_{\text{int}} | Q \rangle + \pi \langle Q | \tilde{H}_{\text{int}} \tilde{\Pi} | Q \rangle}{\langle Q | Q \rangle + \pi \langle Q | \tilde{\Pi} | Q \rangle}. \quad (4.9)$$

Minimizing this functional and projecting the obtained state afterwards to fulfill the correct symmetries is called ‘‘Projection After Variation of a parity eigenstate’’ (PAV $^\pi$). The two intrinsic states that can be obtained by this method are called PAV $^\pi$ states. These states might still break the rotational and translational symmetry of the Hamiltonian.

In ^{11}Be the positive parity ground state is of major interest. It is sometimes called an intruder state since one neutron is in an orbit above the p shell. Figure 4.2 shows the mass densities of the two PAV $^\pi$ states for ^{11}Be . The parameters of these states are chosen in order to minimize the PAV $^\pi$ energy functional (4.9). Since these two PAV $^\pi$ states are intrinsic states they do not need to be parity eigenstates. It can clearly be seen, that the PAV $^{\pi=+1}$ state is much more extended than the PAV $^{\pi=-1}$ state. The energies of the PAV $^{\pi=+1}$ state projected on positive parity is -55.1 MeV while it is -56.7 MeV for the PAV $^{\pi=-1}$ state projected on negative parity.

After angular momentum projection of the PAV $^{\pi=+1}$ on $1/2^+$ and of the PAV $^{\pi=-1}$ state on $1/2^-$ the energies obtained are -60.2 MeV and -61.0 MeV, respectively. When comparing the energies of the mean-field state (Figure 4.1) projected on $J^\pi = 1/2^+$ with the result obtained using the PAV $^{\pi=+1}$ an energy difference of 18 MeV is found. The reason for this large gain is that the mean field state has an intrinsic parity of roughly -1 . This example shows how significantly the description of the $J^\pi = 1/2^+$ ground state in ^{11}Be improves when varying (4.8) instead of (4.4).

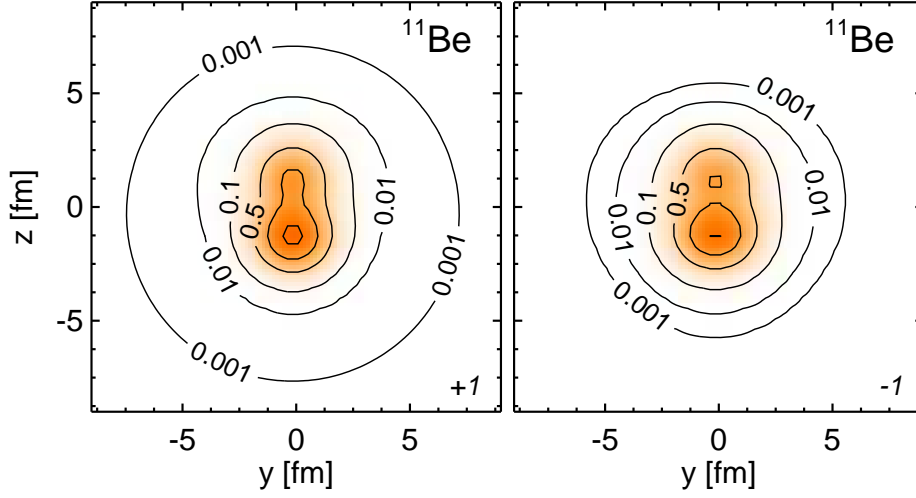


Figure 4.2: Example of intrinsic states obtained for ^{11}Be by minimizing parity projected Slater determinants. The densities shown are mass point densities for the PAV^+ (l.h.s) state and the PAV^- (r.h.s.) in units of the nuclear saturation density ρ_0 .

4.1.2 Separate parity for protons and neutrons

The total parity operator can be written as a product of the parity operator acting only on protons and the parity operator acting only on neutrons

$$\tilde{\Pi} = \tilde{\Pi}_p \tilde{\Pi}_n . \quad (4.10)$$

For a FMD state the neutron-parity operator $\tilde{\Pi}_n$ mirrors every \vec{b} of every Gaussian at the center of the coordinate frame

$$\tilde{\Pi}_n \left(|a, \vec{b}\rangle \otimes |\chi\rangle \otimes |\xi\rangle \right) = \begin{cases} |a, +\vec{b}\rangle \otimes |\chi\rangle \otimes |\xi\rangle & \text{if } \xi = +\frac{1}{2} \\ |a, -\vec{b}\rangle \otimes |\chi\rangle \otimes |\xi\rangle & \text{if } \xi = -\frac{1}{2} \end{cases} \quad (4.11)$$

if the Gaussian is describing a neutron. As the whole argumentation is analog for the proton-parity operator $\tilde{\Pi}_p = \tilde{\Pi} \tilde{\Pi}_n$ it is not again explicitly mentioned.

The nuclear Hamiltonian commutes with the parity operator, but not with the neutron-parity operator. While the kinetic energy

$$T = \frac{1}{A} \sum_{i=1}^A \frac{\vec{p}(i)^2}{2m(i)} \quad (4.12)$$

does commute with the neutron-parity operator

$$[T, \tilde{\Pi}_n]_- = 0 \quad (4.13)$$

4.1 Ritz variation

any component of the nuclear interaction does not

$$[H, \tilde{\Pi}_n]_- \neq 0. \quad (4.14)$$

One example that does not commute

$$\tilde{\Pi}_n \tilde{T}_{\text{CM}} \tilde{\Pi}_n \neq \tilde{T}_{\text{CM}} \quad (4.15)$$

is the center of mass kinetic energy

$$\tilde{T}_{\text{CM}} = \frac{1}{2M} \left(\sum_{i=1}^A \tilde{\vec{p}}(i) \right)^2. \quad (4.16)$$

which is always subtracted from the Hamiltonian.

The state

$$|Q; \pi_p \pi_n\rangle = \frac{1}{4} \left(|Q\rangle + \pi_p \tilde{\Pi}_p |Q\rangle + \pi_n \tilde{\Pi}_n |Q\rangle + \pi_p \pi_n \tilde{\Pi}_p \tilde{\Pi}_n |Q\rangle \right) \quad (4.17)$$

is an eigenstate of $\tilde{\Pi}_p$ and $\tilde{\Pi}_n$ and hence also of $\tilde{\Pi} = \tilde{\Pi}_p \tilde{\Pi}_n$.

$$\tilde{\Pi} |Q; \pi_p \pi_n\rangle = \pi_p \pi_n |Q; \pi_p \pi_n\rangle \quad (4.18)$$

$$= \pi |Q; \pi_p \pi_n\rangle \quad (4.19)$$

This proves that $|Q; \pi_p \pi_n\rangle$ is an eigenstate of $\tilde{\Pi}$ with the eigenvalue $\pi = \pi_p \pi_n$. While the eigenvalues of the neutron- and proton-parity operators are

$$\tilde{\Pi}_n |Q; \pi_p \pi_n\rangle = \pi_n |Q; \pi_p \pi_n\rangle \quad \text{and} \quad (4.20)$$

$$\tilde{\Pi}_p |Q; \pi_p \pi_n\rangle = \pi_p |Q; \pi_p \pi_n\rangle. \quad (4.21)$$

Minimizing the energy functional

$$E^{\pi_p \pi_n} [Q] = \frac{\langle Q; \pi_p \pi_n | \tilde{H}_{\text{int}} | Q; \pi_p \pi_n \rangle}{\langle Q; \pi_p \pi_n | Q; \pi_p \pi_n \rangle} \quad (4.22)$$

using the proton- and neutron-parity projected state $|Q; \pi_p \pi_n\rangle$ is called PAV $^{\pi_p \pi_n}$.

As in a PAV $^\pi$ variation after minimization the parameters of a Slater determinant $|Q\rangle$ are obtained. The parity projected state varied in the PAV $^\pi$ minimization is restored as a part of the projection performed prior to every configuration mixing calculation. The proton- and neutron-parity of $|Q; \pi_p \pi_n\rangle$ is not restored in the projections performed on the Slater determinant $|Q\rangle$ afterwards. In general only the PAV $^{\pi_p \pi_n}$ state with the same π_p and π_n as the shell model ground state

contributes significantly to the ground state. The other three of the four states that can be obtained using $\text{PAV}^{\pi_p \pi_n}$ are related to excited states.

$\text{PAV}^{\pi_p \pi_n}$ states are used to create configurations with a defined proton and neutron parity. Most nuclear physicists think in a shell model like picture when describing the structure of a nucleus. These shell model states are eigenstates of Π_n and Π_p . To create an FMD state that is supposed to resemble a shell model the $\text{PAV}^{\pi_p \pi_n}$ state are a good starting point.

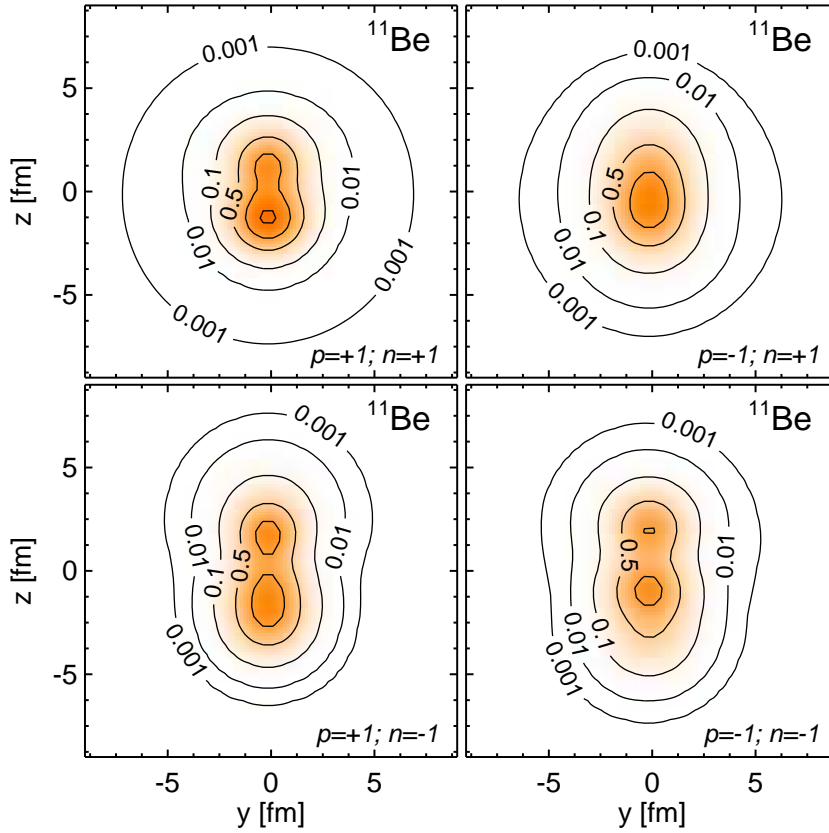


Figure 4.3: ^{11}Be intrinsic states obtained by minimizing the energy expectation values of proton- and neutron-parity projected Slater determinants. The densities shown are point-densities in units of the nuclear saturation density ρ_0 . As indicated in the lower right corner of the plots the left hand side shows densities of intrinsic states that were projected onto positive proton-parity p and the upper panels show the positive neutron-parity n case.

By using the relation

$$\tilde{\Pi}_p \tilde{H}_{\text{int}} = \tilde{\Pi}_n \tilde{\Pi} \tilde{H}_{\text{int}} = \tilde{\Pi}_n \tilde{H}_{\text{int}} \tilde{\Pi} \quad (4.23)$$

4.1 Ritz variation

and the properties of the parity operator the energy functional of the state $|Q; \pi_p \pi_n\rangle$ can be simplified to

$$\frac{\langle Q; \pi_p \pi_n | \tilde{H}_{int} | Q; \pi_p \pi_n \rangle}{\langle Q; \pi_p \pi_n | Q; \pi_p \pi_n \rangle} = \frac{\langle Q; \pi_n | \tilde{H}_{int} | Q; \pi_p \pi_n \rangle}{\langle Q; \pi_n | Q; \pi_p \pi_n \rangle} \quad (4.24)$$

$$= \frac{\langle Q; \pi_n | \tilde{H}_{int} | Q; \pi_p \pi_n \rangle}{\langle Q | Q; \pi_p \pi_n \rangle}. \quad (4.25)$$

The state

$$|Q; \pi_n\rangle := \frac{1}{2} (|Q\rangle + \pi_n \tilde{\Pi}_n |Q\rangle) \quad (4.26)$$

is introduced to get a more compact notation.

The numerator can be expressed using six many-body matrix elements

$$\begin{aligned} \langle Q; \pi_n | \tilde{H}_{int} | Q; \pi_p \pi_n \rangle &= \frac{1}{8} \left[\langle Q | \tilde{H}_{int} | Q \rangle + \langle Q | \tilde{\Pi}_n \tilde{H}_{int} \tilde{\Pi}_n | Q \rangle \right. \\ &\quad + \pi \left(\langle Q | \tilde{H}_{int} \tilde{\Pi} | Q \rangle + \langle Q | \tilde{\Pi}_n \tilde{H}_{int} \tilde{\Pi}_p | Q \rangle \right) \\ &\quad + 2\pi_p \operatorname{Re} \left(\langle Q | \tilde{H}_{int} \tilde{\Pi}_p | Q \rangle \right) \\ &\quad \left. + 2\pi_n \operatorname{Re} \left(\langle Q | \tilde{H}_{int} \tilde{\Pi}_n | Q \rangle \right) \right] \end{aligned} \quad (4.27)$$

while the denominator simplifies to four overlaps

$$\begin{aligned} \langle Q | Q; \pi_p \pi_n \rangle &= \frac{1}{4} \left(\langle Q | Q \rangle + \pi_p \langle Q | \tilde{\Pi}_p | Q \rangle \right. \\ &\quad \left. + \pi_n \langle Q | \tilde{\Pi}_n | Q \rangle + \pi_p \pi_n \langle Q | \tilde{\Pi}_p \tilde{\Pi}_n | Q \rangle \right). \end{aligned} \quad (4.28)$$

Originally 16 matrix elements of the Hamiltonian would have been needed to be evaluated.

In Figure 4.3 the four $\text{PAV}^{\pi_p \pi_n}$ states obtained for ^{11}Be are depicted. In the left panels intrinsic densities of positive proton-parity states are shown while in the upper panels states with positive neutron-parity are shown. After projecting the states on angular momentum and parity $1/2^+$ the energy eigenvalues of the $\text{PAV}^{\pi_p=+1, \pi_n=+1}$, $\text{PAV}^{\pi_p=+1, \pi_n=-1}$, $\text{PAV}^{\pi_p=-1, \pi_n=+1}$ and $\text{PAV}^{\pi_p=-1, \pi_n=-1}$ are -60.2 MeV, -42.1 MeV, -52.5 MeV and -38.2 MeV, respectively.

The $\text{PAV}^{\pi=+1}$ and the $\text{PAV}^{\pi_p=+1, \pi_n=+1}$ states are similar. While the energy calculated with parity projection from the $\text{PAV}^{\pi=+1}$ state is -55.1 MeV the corresponding energy for the $\text{PAV}^{\pi_p=+1, \pi_n=+1}$ state is 0.124 MeV. After projecting

the states on angular momentum and parity $1/2^+$ the situation changes and the $\text{PAV}^{\pi_p=+1, \pi_n=+1}$ is lower in energy by 66 KeV.

For the $\text{PAV}^{\pi=-1}$ no roughly equivalent state is found in the $\text{PAV}^{\pi_p, \pi_n}$ states. The energies for the $\text{PAV}^{\pi_p=+1, \pi_n=-1}$ and $\text{PAV}^{\pi_p=-1, \pi_n=+1}$ after projection on $1/2^-$ are -41.7 MeV and -30.1 MeV, respectively.

4.1.3 Variation after projection

Discrete K

A straightforward way to find for a given angular momentum J and parity π a state $|Q^{(a)}; J^\pi MK\rangle$ that leads to minimal energy is the ‘‘Variation After angular momentum Projection for a pre-defined K ’’ (VAP^K).

$$E_K^{J^\pi}[Q] = \frac{\langle Q | H_{\text{int}} P_{KK}^{J^\pi} | Q \rangle}{\langle Q | P_{KK}^{J^\pi} | Q \rangle}. \quad (4.29)$$

In this procedure the state is projected (numerically) in each step of the minimization. This and the fact that the derivative of the functional with respect to all parameters also has to be projected leads to a significant increase in computing time. It is about three orders of magnitude larger than in the PAV^π case. This is why this method is not used very often. If it is used in this work the state obtained might not be fully converged.

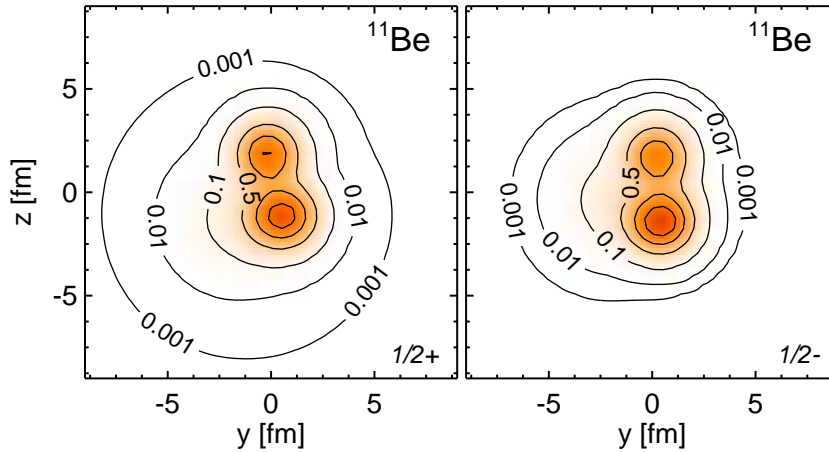


Figure 4.4: Example of intrinsic states for ^{11}Be obtained by a variation after angular momentum and parity projection. The densities shown are nucleon densities in units of the nuclear saturation density ρ_0 .

In this approach a center of mass projection is not performed. In principle it is also possible to perform a variation after numerical center of mass and angular momentum projection. However, due to an additional increase in computing time of up to two orders of magnitude in comparison with VAP this variation after angular momentum and center of mass projection is not used.

In Figure 4.4 the intrinsic densities of the two VAP states obtained for ^{11}Be are pictured. The energies obtained by projecting the VAP states on the angular momentum and parity they were optimized for are -66.2 MeV for the $1/2^-$ and -63.8 MeV for the $1/2^+$ VAP state.

After K mixing

The minimized energy $E_K^{J^\pi} [Q]$ still depends on the K quantum number. Therefore K -mixing is applied for states with $J > 1/2$.

The first way to perform this, is to create one VAP^K state for each possible K and do the K -mixing only during diagonalization of this Hilbert space. The advantage of this method is that several Slater determinants might be able to describe the correlations in the physical state better.

The second way is to do a ‘‘Variation After angular momentum Projection and K -mixing’’ (VAP). The energy functional to be minimized is

$$E^{J^\pi} [Q] = \frac{\langle Q; J^\pi M; \kappa = 1 | H_{\text{int}} | Q; J^\pi M; \kappa = 1 \rangle}{\langle Q; J^\pi M; \kappa = 1 | Q; J^\pi M; \kappa = 1 \rangle}. \quad (4.30)$$

The main advantage in this case is, that the best suited Slater determinant is obtained and the dimension of the Hilbert space for the final configuration mixing is kept small. Due to the increase in computing time a numerical center of mass projection is again not performed.

Orthogonal rest

The aforementioned VAP procedures cannot be used to obtain an intrinsic Slater determinant that describes a second 0^+ state. In this case the Wigner D-function $D_{M=0, K=0}^{0^+ *}(\alpha, \beta, \gamma)$ (Eq. (3.32) page 25) is constant and does not depend on the rotation angles α, β or γ . More importantly K and M have to be zero. Hence only one 0^+ state can be obtained by projecting a single Slater determinant.

To get a second 0^+ state configuration mixing has to be used and the Hilbert space must at least be 2-dimensional. In such a calculation the excited 0^+ is orthogonal to the lowest 0^+ state. Due to this the best way to describe a 0_2^+ state in a VAP approach is to use the 0_1^+ VAP state and minimize the energy of the orthogonal rest of a second Slater determinant with respect to the 0_2^+ state.

The variation of the orthogonal rest without angular momentum projection has turned out not to be successful. This variation tends to produce an intrinsic state that is a rotation of the Slater determinant that it is supposed to be orthogonal to. The energy of the varied state converges to the value of the ground state and after projection the overlap between the two states can become so large that numerical problems occur. Due to this the orthogonal rest is never used without angular momentum projection.

4.2 Configuration mixing

The whole configuration mixing procedure consists of several steps. First a set of Slater determinants $|Q^{(a)}\rangle$ is created to span the many-body Hilbert space. These intrinsic states are projected on parity, angular momentum and a center of mass momentum of zero. A set of states fixed $|Q^{(a)}; J^\pi MK\rangle$ is obtained. The K-mixing diagonalization (Eq. (3.37) on page 26) is performed. The states are mixed by introducing the amplitudes $\Psi_{a\kappa_a}^{J^\pi\alpha}$:

$$|\Psi; J^\pi M\alpha\rangle = \sum_{a,\kappa_a} \Psi_{a\kappa_a}^{J^\pi\alpha} |Q^{(a)}; J^\pi M; \kappa_a\rangle. \quad (4.31)$$

By determining the minimum of the energy functional for a given J^π

$$E^{J^\pi\alpha}[\Psi] = \frac{\sum_{ij} \Psi_i^* H_{ij} \Psi_j}{\sum_{ij} \Psi_i^* N_{ij} \Psi_j}. \quad (4.32)$$

the energy eigenvalue problem (3.43) can be derived. $i = (a, \kappa_a)$ and $j = (b, \kappa_b)$ are again representing all combinations of the indices they are replacing. The superscripts $J^\pi\alpha$ have been partially omitted to improve readability.

By solving the eigenvalue problem (3.43) for every J^π the energy spectrum is obtained. Using a fixed interaction the energies of the states in the spectrum depend on how well the states describe the structure. The following sections describe how the set of states is created.

4.3 Parameterizations

It is possible to restrict the variation in the degrees of freedom during minimization by using parameterizations where q_l depends on a set of real variables x_i . These different parameterizations x_i are describing subsets of the FMD parameter set that can be mapped onto the FMD parameter set q_l . The gradient of an expectation

4.4 Constraint minimization

value of a many-body operator \underline{A} with respect to the parameterization is calculated as

$$\frac{\partial}{\partial x_i} \frac{\langle Q | \underline{A} | Q \rangle}{\langle Q | Q \rangle} = \sum_l \left(\frac{\partial}{\partial q_l^*} \frac{\langle Q | \underline{A} | Q \rangle}{\langle Q | Q \rangle} \cdot \frac{\partial q_l^*}{\partial x_i} + \frac{\partial}{\partial q_l} \frac{\langle Q | \underline{A} | Q \rangle}{\langle Q | Q \rangle} \cdot \frac{\partial q_l}{\partial x_i} \right) \quad (4.33)$$

For hermitian operators \underline{A} a factor of two can be saved in computing time by using

$$\frac{\partial}{\partial x_i} \frac{\langle Q | \underline{A} | Q \rangle}{\langle Q | Q \rangle} = 2\text{Re} \left(\sum_l \left[\frac{\partial}{\partial q_l^*} \frac{\langle Q | \underline{A} | Q \rangle}{\langle Q | Q \rangle} \cdot \frac{\partial q_l^*}{\partial x_i} \right] \right). \quad (4.34)$$

The parameterization that is easiest to imagine is the Antisymmetrized Molecular Dynamics (AMD) parameterization [KEH03]. In the AMD parameterization the width parameter a is real and identical for all Gaussians.

$$a_l(\vec{x}) = x_1 \quad \forall l \quad (4.35)$$

Using this parameterization enables the FMD-code to use the same basis states like the AMD model.

As another example one could use a core parameterization in which one keeps fixed parameters for several nucleons while varying only the parameters for the other nucleons. E.g. by using an α -particle from a separate calculation as a fixed core and adding two neutrons. Minimizing this Slater determinant creates a state where the parameters of the Gaussians for the α -particle are unaltered while the two additional neutrons are described by the wave-functions that are energetically most favorable. A comparison between this state and a ${}^6\text{He}$ PAV $^\pi$ state or a shell model like state can help understanding the physics of this system.

To obtain results which are equivalent to α cluster calculations, the so-called cluster parameterization is used. In this parameterization several fixed clusters are defined. Most often these are α clusters, but it is also possible to use any other Slater determinant as a cluster. The degrees of freedom of these are restricted to rotation and translations. Additional single-particle wave functions can be added to describe individual nucleons in a different parameter set. Whenever the term cluster state is used for an FMD Slater determinant in this thesis an intrinsic state created by using this cluster parameterization is meant. These cluster states can have a large overlap with shell model states.

Other parameterisations as fixing the spin of a nucleon are also possible, however, not used in this work.

4.4 Constraint minimization

Another variational method, that needs much less numerical effort than the VAP procedure, is to define a generator coordinate and create a set of different states

as a function of this coordinate. This is generally done by performing a PAV^π minimization with a given constraint on the generator coordinate. After variation each state in this set is projected onto angular momentum and center of mass. For a given J^π the state that has the lowest energy is chosen. Since this is the Generator Coordinate Method (GCM) this approach is labelled VAP^{GCM} . The term VAP^{GCM} state refers to the Slater determinant with the lowest energy expectation value after angular momentum projection.

The radius, quadrupole moments, octupole moments and number of oscillator quanta are used as generator coordinates. Their exact definition can be found in section 4.5.

Figure 4.5 shows energies of different ^8Be configurations before and after angular momentum projection. A set of 14 Slater determinants is used. These were created by placing two α particles at relative distances d from 0.5 fm to 7.0 fm using a step size of 0.5 fm. It turned out that at a relative distance of ≈ 7.5 fm the maximum of the Coulomb barrier is reached. Therefore states with a relative distance of more than 7 fm have not been included in the Hilbert space. The α particles are parameterized by four Gaussians located at the center of the coordinate frame in phase space $\vec{b} = \vec{0}$. Their width parameters a are all fixed to 2.0 fm^2 . The spins of the nucleons with identical isospin are orthogonal.

This example shows the effect of the projection and that the minimum of the angular momentum projected energy in general is not at the same value of the generator coordinate (here d) as the minimum of the intrinsic energy. An extended version of this example also using the width a as a generator coordinate can be found in section 4.6.

The example is a very simple one. The parameter space has only one degree of freedom d which is also the constrained value. This parameter is only evaluated on few grid points.

This example is used here since it shows that it is possible to create a Slater determinant, which after projection has an energy expectation value below the energy obtained, by using the projected PAV^π state. The extension of this example in section 4.6 also shows how a set of intrinsic states created by applying different constraints can help to provide important configurations needed for configuration mixing calculations.

The algorithms to find numerically the minimum of a function that depends on many variables are faster and more stable if the gradient of this function is also provided. In a simple gradient approach one would move from the starting point in the direction of the negative gradient. The size of this step in the multidimensional parameter space has to be chosen small enough to avoid missing relevant changes in the slope of the function. On the other hand it has to be chosen big enough to avoid calculating unnecessary many points.

For each constraint that is employed its gradient is also provided. The direction

4.4 Constraint minimization

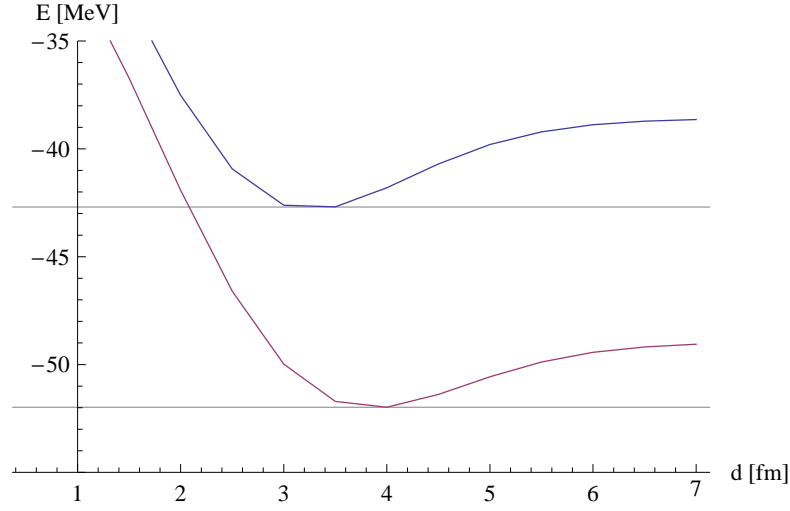


Figure 4.5: Energies of two α particles located at relative distances d as generator coordinate. Shown in upper curve is the energy projected on positive parity and in the lower curve the energy projected on angular momentum 0^+ .

of the step depends on the difference between the value the constraint is supposed to have after optimization and the value it has at the starting point. If the actual value is too high a step is chosen in the direction of the gradient to lower the value. If it is too low the opposite direction is chosen and if the two values match, the step is performed perpendicular to the gradient of the constraint, to stay on the subspace that fulfills the condition.

The actual implementation of the constraint optimization problem is done using the sequential quadratic programming routine “donlp2” [Spe][Spe98]. As input this routine needs a function $f(\vec{x})$ which is to be minimized and a function $\vec{h}(\vec{x})$ which constrains the possible parameter set. In the applications of this routine in FMD $f(\vec{x})$ is always an energy expectation value, \vec{x} is always the parametrization and

$$\vec{h}(\vec{x}) = (C_1(\vec{x}) - c_1, C_2(\vec{x}) - c_2, \dots, C_m(\vec{x}) - c_m)^T \quad (4.36)$$

is a vector whose components contain the calculated constraints $C_j(\vec{x})$. c_j is the value the j^{th} constraint is supposed to have. The $h_j(\vec{x})$ are the difference between the calculated value for the constraint $C_j(\vec{x})$ at the given point \vec{x} and the value this constraint is supposed to have c_j . Thus all $h_j(\vec{x})$ have to become zero i.e.

$$\vec{h}(\vec{x}) = \vec{0}. \quad (4.37)$$

If the dimension of the unrestricted parameter space is n and m is the number of components in $\vec{h}(\vec{x})$ the submanifold for which the condition Eq. (4.37) can be satisfied is $n - m$ dimensional.

To stay on the $\vec{h}(\vec{x}) = \vec{0}$ hypersurface the routine chooses the next point perpendicular to the gradient of every $h_j(\vec{x})$ and to minimize $f(\vec{x})$ it moves in the direction of the gradient of $f(\vec{x})$. At the minimum of $f(\vec{x})$ in the $\vec{h}(\vec{x}) = \vec{0}$ subspace the gradients $\vec{\nabla}f(\vec{x})$ and all $\vec{\nabla}h_j(\vec{x})$ have to be parallel. This means there is no component of $\vec{\nabla}f(\vec{x})$ orthogonal to any $\vec{\nabla}h_j(\vec{x})$ or

$$\vec{\nabla}f(\vec{x}) - \frac{(\vec{\nabla}f(\vec{x}) \cdot \vec{\nabla}h_j(\vec{x}))}{\vec{\nabla}h_j(\vec{x}) \cdot \vec{\nabla}h_j(\vec{x})} \vec{\nabla}h_j(\vec{x}) = \vec{0} \quad (4.38)$$

By satisfying both conditions eq. (4.37) and (4.38) a local extremum can be obtained. When also calculating points close to the extremum it is ensured that a minimum has been found. As an attempt to obtain the global minimum of the hypersurface given by the constraint the minimization routine is invoked several times using a random modification of the previous result as a starting point. The strength of this random modification is reduced each time.

It is also possible to specify constraints in a different function $\vec{g}(\vec{x})$. The condition that the routine aims to achieve is

$$\vec{g}(\vec{x}) \geq \vec{0}. \quad (4.39)$$

This way it does not reduce the dimension of the submanifold for which eq. (4.39) is fulfilled. Each condition $g_j(\vec{x})$ restricts the parameters to a half-space.

$\vec{g}(\vec{x})$ is not used to create a constraint with a minimal value, however, this might be done in the future. Here it is only used to enforce the stipulation, that the real part of all single particle width parameters a is positive. This ensures that the single particle wave functions are Gaussian in phase-space (see Eq.:(3.2)) and avoids numerical issues.

To further avoid numerical issues and increase the performance of the process, the gradient of $f(\vec{x})$ and the derivatives of $h(\vec{x})$ with respect to all variational parameters \vec{x} are also provided analytically.

The constraints are chosen to be rotationally and translationally invariant scalars to ensure that states with different values for a constraint are also different after projection and K-mixing. If this would not be demanded a Slater determinant $|Q^{(b)}\rangle$ that is obtained by a rotation (or translation) of a different one $|Q^{(b)}\rangle \approx \tilde{R}(\alpha, \beta, \gamma)|Q^{(a)}\rangle$ could be obtained for a different value of the same constraint. After projection and K-mixing these would become very similar: $|Q^{(b)}; J^\pi M; \kappa_b\rangle \approx |Q^{(a)}; J^\pi M; \kappa_a\rangle$.

The VAP^{GCM} state is used here as a starting point for an actual VAP minimization. Due to the increase in computing time a VAP minimization needs, VAP states might only be a slight improvement to the VAP^{GCM} state.

4.4.1 Lagrange multiplier

Another approach commonly used in nuclear physics is to apply a Lagrange multiplier:

$$\vec{\nabla}f(\vec{x}) - \lambda\vec{\nabla}h(\vec{x}) = \vec{0}. \quad (4.40)$$

Since this only states that $\vec{\nabla}f(\vec{x})$ and $\vec{\nabla}h(\vec{x})$ are parallel to each other this method is equivalent to the constrained minimization introduced in section 4.4.

When using this method the Lagrange multiplier λ has to be fixed first and $f(\vec{x}) - \lambda h(\vec{x}) = \vec{0}$ is varied to obtain the extremum $\vec{x}(\lambda)$. The main difference between the two methods is that in the Lagrange approach the minimum $\vec{x}(\lambda)$ depends on λ and not on c . The value the actual constraint has $C(\vec{x}(\lambda))$ can only be calculated after variation, thus several iterations might be needed to fulfill $C(\vec{x}(\lambda)) = c$.

The usual approach is to obtain $\vec{x}(\lambda)$ by solving (4.40) for a set of different λ 's. The λ_e that yields the wanted constraint has the side condition $C(\vec{x}(\lambda_e)) - c = 0$. $\vec{x}_e = \vec{x}(\lambda_e)$ is the extremum that can be obtained by using

$$\lambda_e = \frac{\vec{\nabla}f(\vec{x}) \cdot \vec{\nabla}h(\vec{x})}{\vec{\nabla}h(\vec{x}) \cdot \vec{\nabla}h(\vec{x})}. \quad (4.41)$$

4.5 Constraints

In general the constraints are calculated either as the one body expectation value eq. (3.17), the two body expectation value eq. (3.18) or both.

The derivatives of the constraints are needed to improve the convergence behavior of the minimization routine and save computing time.

Many constraints can also be restricted in terms of isospin i.e. they act only on protons or neutrons. The p,n -notation in this chapter is meant to be understood as either p protons only, n neutrons only or both without any further indication. The appropriate projectors on protons and neutrons are:

$$\tilde{P}^p(l) = \frac{1}{2}(1 + \tau_3(l)) \quad (4.42)$$

$$\tilde{P}^n(l) = \frac{1}{2}(1 - \tau_3(l)). \quad (4.43)$$

To achieve a more compact notation the proton or neutron projection operator without superscripts has to be understood as

$$\tilde{P}(l) := \tilde{P}^p(l) + \tilde{P}^n(l) = 1. \quad (4.44)$$

Using these projectors to project on protons (4.42) and on neutrons (4.43) to consistently replace all three cases¹ for the constraints by a single general expression is only possible if the number of nucleons A is also defined with an index:

$$A^p := Z; \quad A^n := N. \quad (4.45)$$

The matrix elements are evaluated in the FMD basis as

$$P_{kl}^p = \langle q_k | \tilde{P}^p | q_l \rangle = \frac{1}{4} (1 + \xi_k) (1 + \xi_l) \langle q_k | q_l \rangle \quad (4.46)$$

$$P_{kl}^n = \langle q_k | \tilde{P}^n | q_l \rangle = \frac{1}{4} (1 - \xi_k) (1 - \xi_l) \langle q_k | q_l \rangle \quad (4.47)$$

These allow for the usage of constraints that act on protons or neutrons only; e.g. the electrical dipole moment.

4.5.1 Center of mass

The center of mass constraint is a rather important constraint as it is always used when varying parameters of a parity projected state (PAV $^\pi$, PAV $^{\pi_p \pi_n}$ and VAP). This is done to avoid spurious center of mass excitations. The term *center of mass constraint* refers here to a constraint on the center of mass in phase space i.e. in coordinate and momentum space at the same time. To be able to calculate the center of mass one needs an operator that yields the mass of the nucleon l

$$m(l) = m_p \tilde{P}^p(l) + m_n \tilde{P}^n(l), \quad (4.48)$$

and the expectation value of the total mass operator

$$M := \langle \tilde{M} \rangle = \left\langle \sum_{l=1}^A m(l) \right\rangle = Zm_p + Nm_n. \quad (4.49)$$

In close analogy to classical mechanics the center of mass and center of mass velocity operators are defined as

$$\tilde{\vec{X}}^{\text{CM}} = \frac{1}{M} \sum_{l=1}^A m(l) \tilde{\vec{x}}(l) \quad (4.50)$$

$$\tilde{\vec{V}}^{\text{CM}} = \frac{1}{M} \tilde{\vec{K}}^{\text{CM}} = \frac{1}{M} \sum_{l=1}^A \tilde{\vec{k}}(l). \quad (4.51)$$

The corresponding expectation values are

$$\langle \tilde{\vec{X}}^{\text{CM}} \rangle = \frac{1}{M} \sum_{k,l=1}^A \langle q_k | m \tilde{\vec{x}} | q_l \rangle o_{lk} \quad (4.52)$$

¹The third case is without isospin dependent projection (4.44)

and

$$\left\langle \vec{V}^{\text{CM}} \right\rangle = \frac{1}{M} \sum_{k,l=1}^A \langle q_k | \vec{k} | q_l \rangle o_{lk}. \quad (4.53)$$

The derivatives of a one- or two-body operator are always calculated in the approach mentioned in (3.19) and (3.20). Since the inverse overlap matrix and the first derivative of it depend only on the state there is only one unknown term left in these expressions. This term is

$$\frac{\partial \langle q_k | m_{\vec{x}} | q_l \rangle}{\partial q_{\mu}^*} = m_l \delta_{mk} \frac{\partial}{\partial q_{\mu}^*} \left(\vec{\rho}_{kl} \langle q_k | q_l \rangle \right) \quad (4.54)$$

for the center of mass in coordinate space and

$$\frac{\partial \langle q_k | \vec{k} | q_l \rangle}{\partial q_{\mu}^*} = \delta_{mk} \frac{\partial}{\partial q_{\mu}^*} \left(\vec{\pi}_{kl} \langle q_k | q_l \rangle \right) \quad (4.55)$$

for the center of mass in momentum space. The values $\vec{\rho}_{kl}$ and $\vec{\pi}_{kl}$ are the matrix elements of the position and momentum operator, respectively. These can be found in the appendix in equations (A.10) and (A.9).

The value, this constraint is supposed to have, is fixed to zero

$$\left\langle \vec{X}^{\text{CM}} \right\rangle^2 = 0 \quad (4.56)$$

$$\left\langle \vec{K}^{\text{CM}} \right\rangle^2 = 0, \quad (4.57)$$

to have a well-defined intrinsic parity at the center of the coordinate frame and to minimize the center of mass kinetic energy of the intrinsic state. The square of the expectation value is used to have a rotationally invariant constraint. All the other constraints are flexibly adjusted to the nucleus. It is always used when any kind of parity projection is employed during minimization.

4.5.2 Radius

Most constraints are evaluated relatively to the center of mass to ensure translational invariance. In the radius constraint

$$(R^{p,n})^2 = \frac{1}{A^{p,n}} \sum_{l=1}^A \left(\vec{x}(l) - \vec{X}^{\text{CM}} \right)^2 P^{p,n}(l) \quad (4.58)$$

the center of mass operator is not replaced by its expectation value.

To evaluate the center of mass operator \tilde{X}^{CM} the approximation that nucleons have the same mass is used:

$$\tilde{X}^{\text{CM}} = \frac{1}{A} \sum_{k=1}^A \tilde{x}(k). \quad (4.59)$$

Using this relation $(R^{p,n})^2$ can be expressed as

$$(R^{p,n})^2 = \frac{1}{A^{p,n}} \sum_{l=1}^A \left(\tilde{x}(l)^2 - \frac{2}{A} \tilde{x}(l) \cdot \sum_{k=1}^A \tilde{x}(k) + \frac{1}{A^2} \sum_{k,m=1}^A \tilde{x}(k) \cdot \tilde{x}(m) \right) P^{p,n}(l). \quad (4.60)$$

The one-body term of this operator is

$$\left((R^{p,n})^2 \right)^{[1]} = \frac{1}{A^{p,n}} \sum_{l=1}^A \left(\tilde{x}(l)^2 - \frac{2}{A} \tilde{x}(l) \cdot \tilde{x}(l) \right) P^{p,n}(l) \quad (4.61)$$

$$+ \frac{1}{A^2} \sum_{l=1}^A \tilde{x}(l)^2. \quad (4.62)$$

While the two-body term is:

$$\left((R^{p,n})^2 \right)^{[2]} = -\frac{2}{AA^{p,n}} \tilde{x}(l) \cdot \sum_{k \neq l=1}^A \left(\tilde{x}(l) \cdot \tilde{x}(k) \right) P^{p,n}(l) \quad (4.63)$$

$$+ \frac{1}{A^2} \sum_{k \neq n=1}^A \tilde{x}(k) \cdot \tilde{x}(n). \quad (4.64)$$

It is a mean square of the deviations of the nucleons from the center of mass. Whenever values given for the radius constraint are square roots of $\langle R^2 \rangle$.

The expectation value of the $\tilde{x}(l) \cdot \tilde{x}(l)$ is a special case of equation (A.13).

Increasing the value of this constraint results in spatially more extended states. For large radii clustering often occurs. This clustering generally helps the description of the Hilbert space but it is also possible to create a state where a single nucleon² is located very far away from the other cluster. In the latter case the energy obtained is the energy of the ground state of the second cluster with a nucleon located somewhere to fulfill the constraint. Such states are not used here.

²Due to the Coulomb repulsion of equally charged particles like protons this nucleon often is a neutron.

4.5.3 Multipoles

Several of the used constraints are derived from the multipole expansion

$$Q_{lm} = \sqrt{\frac{4\pi}{2l+1}} \int d^3r Y_{lm}^*(\theta, \phi) r^l \rho(\vec{r}). \quad (4.65)$$

$l = 0, 1, 2, 3$ corresponds to the monopole, dipole, quadrupole and octupole respectively. l is also the rank of the tensor operator that describes the corresponding deformation. As an example the monopole $l = 0$ term is a scalar while the dipole term is a vector.

Dipole

The square $\langle \vec{D} \rangle^2$ of the expectation value of the electrical dipole operator

$$\vec{D} = \sum_{l=1}^A \left(\vec{x}^{(l)} - \langle \vec{X}^{\text{CM}} \rangle \right) P_l^p(l) \quad (4.66)$$

is used as a constraint. The electrical dipole is not used directly to ensure rotational and translational invariance and obtain a scalar value.

Since the mass dipole operator vanishes it is not used. A neutron dipole operator could also be implemented but is not used here. Increasing the value of this constraint leads to a state in which the proton center of mass and the total (and neutron) center of mass are separated. A set of these states can describe a vibration of the protons against the neutrons.

Quadrupole

The quadrupole operator

$$Q_{ij}^{p,n} = \sum_{l=1}^A \left[3 \left(x_i^{(l)} - \langle X_i^{\text{CM}} \rangle \right) \left(x_j^{(l)} - \langle X_j^{\text{CM}} \rangle \right) - \delta_{ij} \left(\vec{x}^{(l)} - \langle \vec{X}^{\text{CM}} \rangle \right)^2 \right] P_l^{p,n} \quad (4.67)$$

has 9 components of which 5 are independent. To just get a single scalar for the quadrupole moment the square root of the sum of squares of the expectation values

$$\sqrt{\sum_{ij} \langle Q_{ij} \rangle^2} \quad (4.68)$$

is used throughout this work. Alternatively the determinant $\det \left(\langle Q_{ij} \rangle \right)$ can be used.

Octupole

The octupole operator

$$\begin{aligned}
\mathcal{O}_{ijk}^{p,n} &= \sum_{l=1}^A \left[5 \left(x_i(l) - \langle X_i^{\text{CM}} \rangle \right) \left(x_j(l) - \langle X_j^{\text{CM}} \rangle \right) \left(x_k(l) - \langle X_k^{\text{CM}} \rangle \right) \right. \\
&\quad - \delta_{ij} \left(\vec{x}(l) - \langle \vec{X}^{\text{CM}} \rangle \right)^2 \left(x_k(l) - \langle X_k^{\text{CM}} \rangle \right) \\
&\quad - \delta_{jk} \left(\vec{x}(l) - \langle \vec{X}^{\text{CM}} \rangle \right)^2 \left(x_i(l) - \langle X_i^{\text{CM}} \rangle \right) \\
&\quad \left. - \delta_{ik} \left(\vec{x}(l) - \langle \vec{X}^{\text{CM}} \rangle \right)^2 \left(x_j(l) - \langle X_j^{\text{CM}} \rangle \right) \right] P^{p,n}(l)
\end{aligned} \tag{4.69}$$

has 27 components of which 7 are independent. Similar to the quadrupole constraint the invariant scalar is obtained by calculating the square root of the sum of the squares of all elements

$$\sqrt{\sum_{ijk} \langle \mathcal{O}_{ijk} \rangle^2}. \tag{4.70}$$

4.5.4 Single particle angular momentum

In this work the single particle angular momentum \vec{j} is used in combination with the oscillator constraint to generate shell model ground states or shell model like excited states.

It is calculated as an expectation value of the sum of the single particle operators $\vec{j}(k)$:

$$\vec{j}^2 = \sum_{k=1}^A \vec{j}(k)^2 \tag{4.71}$$

which are calculated using

$$\vec{j}(k)^2 = \vec{l}(k)^2 + \vec{s}(k)^2 + 2\vec{l}(k) \cdot \vec{s}(k). \tag{4.72}$$

This expression is just the square of the definition of j : $\vec{j} = \vec{l} + \vec{s}$.

j is evaluated relatively to the center of mass in phase space. Like expected from classical mechanics \vec{l} is defined as

$$\vec{l}(k) = \left(\vec{r}(k) - \langle \vec{X}^{\text{CM}} \rangle \right) \times \left(\vec{k}(k) - m \langle \vec{V}^{\text{CM}} \rangle \right). \tag{4.73}$$

4.5.5 Oscillator quanta

In the three dimensional harmonic oscillator one defines the two ladder operators:

$$a_i^\dagger = \frac{1}{\sqrt{2}} \left(\frac{x_i}{\xi_i} - i\xi_i k_i \right) \quad (4.74)$$

$$a_i = \frac{1}{\sqrt{2}} \left(\frac{x_i}{\xi_i} + i\xi_i k_i \right) \quad (4.75)$$

The raising operator a_i^\dagger increases the number of oscillator quanta in the i direction of the system by one. Its hermitian adjoint, the lowering operator a_i lowers it by one.

The number operator that counts the number of oscillator quanta in each direction is defined to be the product of the creation operator a_i^\dagger and the raising operator a_i :

$$N_i = a_i^\dagger a_i . \quad (4.76)$$

Its expectation value $N_i = \langle N_i \rangle$ is the number of oscillator quanta contained in the used state.

To express N_i in terms of x_i and k_i (4.74) and (4.75) are used in (4.76):

$$N_i = \frac{1}{2} \left(\frac{x_i}{\xi_i} - i\xi_i k_i \right) \left(\frac{x_i}{\xi_i} + i\xi_i k_i \right) \quad (4.77)$$

$$= \frac{1}{2} \left(\frac{x_i^2}{\xi_i^2} + \xi_i^2 k_i^2 - i[k_i, x_i]_- \right) \quad (4.78)$$

$$= \frac{\xi_i^2 k_i^2}{2} + \frac{x_i^2}{2\xi_i^2} - \frac{1}{2} . \quad (4.79)$$

The expectation value of this operator is

$$N_i := \frac{1}{2} \left[\frac{1}{\xi_i^2} \langle x_i^2 \rangle + \xi_i^2 \langle k_i^2 \rangle - 1 \right] . \quad (4.80)$$

The length scales ξ_i for the three spatial directions may be different for a triaxially deformed oscillator. In general they are eigenvalues of a 3×3 -length matrix L . In an isotropic oscillator with only one oscillator frequency ω this matrix would be $L = \frac{1}{\sqrt{m\omega}} \mathbb{1}_3$. Where $\mathbb{1}_3$ is the unit matrix in three dimensions. In the case where the major axes are aligned with the coordinate frame axes, but not necessarily identical this matrix becomes

$$L = \begin{pmatrix} \xi_1 & 0 & 0 \\ 0 & \xi_2 & 0 \\ 0 & 0 & \xi_3 \end{pmatrix} . \quad (4.81)$$

In general the used matrix L can also have off-diagonal elements which can account for arbitrary rotations of the oscillator:

$$L = \begin{pmatrix} L_{11} & L_{12} & L_{13} \\ L_{21} & L_{22} & L_{23} \\ L_{31} & L_{32} & L_{33} \end{pmatrix}. \quad (4.82)$$

The idea is to generalize equation (4.79) using L . To achieve this first the variance matrices $\tilde{X}_{ij}^{p,n}$ and $\tilde{K}_{ij}^{p,n}$ are defined as:

$$\tilde{X}_{ij}^{p,n} := \sum_{l=1}^A \tilde{P}^{p,n}(l) \left(\tilde{x}_i(l) - \langle \tilde{X}_i^{\text{CM}} \rangle \right) \left(\tilde{x}_j(l) - \langle \tilde{X}_j^{\text{CM}} \rangle \right) \quad (4.83)$$

$$\tilde{K}_{ij}^{p,n} := \sum_{l=1}^A \tilde{P}^{p,n}(l) \left(\tilde{k}_i(l) - \tilde{m}(l) \langle \tilde{V}_i^{\text{CM}} \rangle \right) \left(\tilde{k}_j(l) - \tilde{m}(l) \langle \tilde{V}_j^{\text{CM}} \rangle \right). \quad (4.84)$$

$\tilde{X}_{ij}^{p,n}$ and $\tilde{K}_{ij}^{p,n}$ replace x_i^2 and k_i^2 thus the units are [fm²] and [fm⁻²], respectively.

$$\tilde{X}_{ij} = \tilde{X}_{ij}^p + \tilde{X}_{ij}^n \quad (4.85)$$

$$\tilde{K}_{ij} = \tilde{K}_{ij}^p + \tilde{K}_{ij}^n \quad (4.86)$$

The matrices $\tilde{X}_{ij}^{p,n}$ and $\tilde{K}_{ij}^{p,n}$ are defined as the expectation values of the corresponding operators:

$$\tilde{X}_{ij}^{p,n} := \langle \tilde{X}_{ij}^{p,n} \rangle, \quad \tilde{K}_{ij}^{p,n} := \langle \tilde{K}_{ij}^{p,n} \rangle. \quad (4.87)$$

Equation (4.80) represents the eigenvalues of a matrix

$$N = \begin{pmatrix} N_1 & 0 & 0 \\ 0 & N_2 & 0 \\ 0 & 0 & N_3 \end{pmatrix}. \quad (4.88)$$

and is generalized to

$$N := \frac{1}{2} \left(L^{-1} \cdot X \cdot L^{-1} + L \cdot K \cdot L - A \mathbb{1}_3 \right). \quad (4.89)$$

This relation is valid for nucleons, protons or neutrons. Only for the sake of readability the superscripts p and n are left out. The definition of $A^{p,n}$ can be found in (4.45). From the term $-A^{p,n} \mathbb{1}_3$ in the generalization it can be seen, that not only the alignment of the oscillator has been generalized, but the description is now in the many-body space.

4.5 Constraints

The length matrix L is undetermined. As will later become obvious it need not be determined explicitly. Like X and K , L is also a symmetric, positive matrix.

To obtain a single rotationally invariant value from the generalized form of this matrix the trace is used:

$$N = \text{Tr}(N) . \quad (4.90)$$

N represents the number of oscillator quanta in a given many-body state. This is, however, not unique as it depends on L . The elements L_{ij} of L depend on the orientation and the three eigenfrequencies $\omega_i = \frac{1}{m\xi_i^2}$ of the chosen oscillator. Therefore L is chosen such that the minimal N is obtained. This is achieved by demanding N to be stationary under variations with respect to L .

$$\frac{\delta N}{\delta L} = 0 \quad (4.91)$$

$$\delta N = \delta \text{Tr}(N) = \text{Tr}(\delta N) \quad (4.92)$$

The following relations are used to obtain the minimal N :

$$\delta L = \delta L^T \Rightarrow (L \cdot X \cdot \delta L)^T = \delta L \cdot X \cdot L \quad (4.93)$$

$$\text{Tr}(X^T) = \text{Tr}(X) \quad (4.94)$$

$$\delta L^{-1} = -L^{-1} \cdot \delta L \cdot L^{-1}, \quad (4.95)$$

They also hold true if X is replaced by K . The variation of $\text{Tr}(N)$ becomes:

$$\begin{aligned} \text{Tr}(\delta N) &= \frac{1}{2} \text{Tr}(\delta L^{-1} \cdot X \cdot L^{-1} + L^{-1} \cdot X \cdot \delta L^{-1} + \delta L \cdot K \cdot L + L \cdot K \cdot \delta L) \\ &= \text{Tr}(\delta L^{-1} \cdot X \cdot L^{-1} + (\delta L^{-1})^T \cdot X^T \cdot (L^{-1})^T + \delta L \cdot K \cdot L + \delta L^T \cdot K^T \cdot L^T) \\ &= 2 \text{Tr}(\delta L^{-1} \cdot X \cdot L^{-1} + \delta L \cdot K \cdot L) \\ &= \text{Tr}(-L^{-1} \cdot \delta L \cdot L^{-1} \cdot X \cdot L^{-1} + \delta L \cdot K \cdot L) \\ &= \text{Tr}(-\delta L \cdot L^{-1} \cdot X \cdot L^{-2} + \delta L \cdot K \cdot L) \\ &= \text{Tr}(\delta L \cdot \{-L^{-1} \cdot X \cdot L^{-2} + K \cdot L\}) \\ &= 0 . \end{aligned} \quad (4.96)$$

Since the trace of N has to vanish for all variations δL one obtains:

$$L^{-1} \cdot X \cdot L^{-2} = L \cdot K \quad (4.97)$$

or

$$L^{-1} \cdot X \cdot L^{-1} = L \cdot K \cdot L \quad (4.98)$$

This implies

$$N = L^{-1} \cdot X \cdot L^{-1} - \frac{A}{2} \mathbb{1}_3 \quad (4.99)$$

$$= L \cdot K \cdot L - \frac{A}{2} \mathbb{1}_3 . \quad (4.100)$$

$N + \frac{A}{2} \mathbb{1}_3$ can be expressed as a sum:

$$L^{-1} \cdot X \cdot L^{-1} = L \cdot K \cdot L \quad (4.101)$$

$$= \frac{1}{2} (L^{-1} \cdot X \cdot L^{-1} + L \cdot K \cdot L) . \quad (4.102)$$

or using

$$(L^{-1} \cdot X \cdot L^{-1} \cdot L \cdot K \cdot L)^{\frac{1}{2}} = (L^{-1} \cdot X \cdot K \cdot L)^{\frac{1}{2}} \quad (4.103)$$

and the square root of

$$L^{-1} \cdot X \cdot K \cdot L = (L^{-1} \cdot (X \cdot K)^{\frac{1}{2}} \cdot L)^2 \quad (4.104)$$

it can be written as

$$L^{-1} \cdot X \cdot L^{-1} = L \cdot K \cdot L = L^{-1} \cdot (X \cdot K)^{\frac{1}{2}} \cdot L . \quad (4.105)$$

From the definition of N in equation (4.90) and equation (4.101)

$$N = \text{Tr} \left(\frac{1}{2} (L^{-1} \cdot X \cdot L^{-1} + L \cdot K \cdot L) - A \mathbb{1}_3 \right) \quad (4.106)$$

is obtained. Using expression (4.103) and $\text{Tr}(\mathbb{1}_3) = 3$ it becomes:

$$N = \text{Tr} \left((L^{-1} \cdot X \cdot K \cdot L)^{\frac{1}{2}} \right) - \frac{3}{2} A . \quad (4.107)$$

After exploiting equation (4.105) and the similarity-invariance from the cyclic property of the trace

$$\text{Tr} (L^{-1} \cdot (X \cdot K)^{\frac{1}{2}} \cdot L) = \text{Tr} ((X \cdot K)^{\frac{1}{2}} \cdot L \cdot L^{-1}) = \text{Tr} ((X \cdot K)^{\frac{1}{2}}) \quad (4.108)$$

the final expression for N becomes:

$$N = \text{Tr} ((X \cdot K)^{\frac{1}{2}}) - \frac{3}{2} A . \quad (4.109)$$

4.5 Constraints

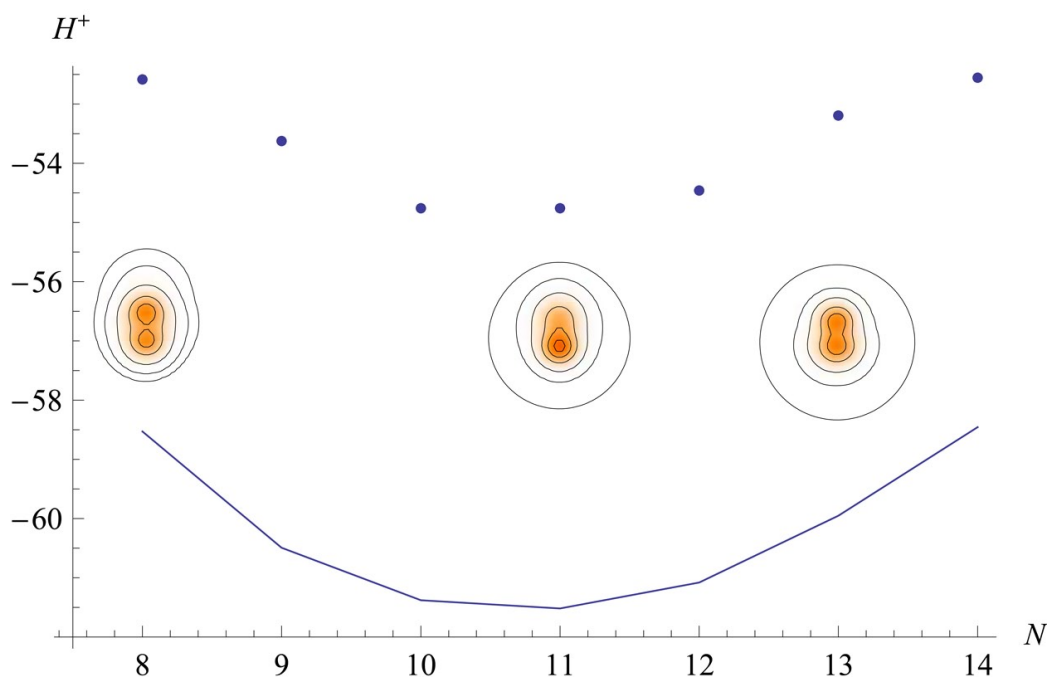


Figure 4.6: Energies of ^{11}Be GCM states projected on parity, before and after projection on angular momentum $1/2^+$. The dots represent energies of the parity projected states while the line indicates the energy of the angular momentum and center of mass projected states.

Evaluating N in this form has the major advantage it does not depend on L . It is not necessary to determine the L for which N becomes minimal and calculate N in the next step.

The number of oscillator quanta is zero for each nucleon in the s -shell, one for each nucleon in the p -shell, two for each nucleon in the sd -shell. For higher shells this sequence continues.

To create a set of states the number of oscillator quanta is used as a generator coordinate while the energy is minimized under the constraint N .

The lowest number of oscillator quanta consistent with the Pauli principle is $N = 7$ for ^{11}Be in the naively expected negative parity ground state. For a ground state having positive parity as observed in experiments it is $N = 8$.

Figure 4.6 shows the energy of 7 states for ^{11}Be . These states were created by minimizing the energy after projecting on positive parity and demanding $N = 8$ to 14. The energies as occurring after variation are indicated as dots, while the energy of the same states after projection on $J^\pi = 1/2^+$ is indicated by a connecting line. Additionally for three of the seven states the densities of the intrinsic states are also shown. The neutron occupation numbers of the ^{11}Be positive parity

ground state show an admixture of s and $d_{5/2}$ states over several shells. In this discussion only shells with single-particle n from 2 to 8 are included, the $0s$ shell is occupied by neutrons in the core and thus explicitly excluded. In the $N = 8$ Slater determinant the contribution from the s and $d_{5/2}$ shells is 0.19 and 0.21, respectively. While it becomes strongly s dominated in the $N = 13$. The occupation numbers are 0.71 for the s shells and 0.09 for the $d_{5/2}$ shells.

4.5.6 Spin-orbit coupling

The way that has turned out to be most useful for constructing states with different spin-orbit strengths $\langle \vec{\tilde{L}} \cdot \vec{\tilde{S}} \rangle$ is not a constraint on $\langle \vec{\tilde{L}} \cdot \vec{\tilde{S}} \rangle$ but minimizing the parameters of the Slater determinant using an interaction $\tilde{H}(\lambda_{LS})$ with a reduced $\vec{\tilde{L}} \cdot \vec{\tilde{S}}$ correction term:

$$\tilde{H}(\lambda_{LS}) = \tilde{H} - (1 - \lambda_{LS}) \sum_T \hat{V}_{ls}^{T,\text{corr}}(r) \vec{\tilde{L}} \cdot \vec{\tilde{S}}. \quad (4.110)$$

$1 - \lambda_{LS}$ is a Lagrange multiplier as explained in subsection 4.4.1. λ_{LS} is the parameter that is used to express that a state was created using this approach. A λ_{LS} of 100% is equivalent to the interaction using the full correction term, while a λ_{LS} of 0% means the correction term was not used at all.

λ_{LS} is mainly used when creating states. For the angular momentum and center of mass projection the interaction containing the full $\vec{\tilde{L}} \cdot \vec{\tilde{S}}$ strength is used if nothing else is stated. At the end of section 5.2 a spectrum that was calculated using 25% of the correction term in the interaction is presented in addition to the usual spectrum. Combining this method using λ_{LS} of 0%, 25%, 50% and 75% with different constraints on the number of oscillator quanta results in four additional states per chosen oscillator quantum. Generally one of them turns out to be the best single Slater determinant description of the ground state.

4.6 Selecting states

Given a large³ set of n Slater determinants $|Q^{(a)}\rangle$ it is generally not useful to calculate the n^2 projected matrix elements $H_{ij} = \langle Q^{(a)}; J^\pi M; \kappa_a | \tilde{H} | Q^{(b)}; J^\pi M; \kappa_b \rangle$ and diagonalize the Hamiltonian. The most obvious reason is that some states might contribute only very little to the lowest eigenstates and thus should be excluded from the calculation to save computing time. States $|Q^\pi\rangle$ whose parameters have been adjusted to a certain parity $\{Q^{\pi=\pm 1}\}$ generally do not strongly contribute if

³Large in this context is in the order of 100 states. For each Beryllium isotope the size of this set of intrinsic states is mentioned.

projected on the opposite parity. In other words the energy calculated using a state $\tilde{P}^-|Q^+\rangle$ or $\tilde{P}^+|Q^-\rangle$ is often outside the energy region of interest. Therefore, and to save computing time, the positive and negative parities are in some cases calculated individually.

An important reason for carefully selecting the appropriate states for the multiconfiguration calculation is to avoid numerical issues. These problems often occur if very similar states or states that are linearly depending on others are used to span the same Hilbert space.

Therefore the states are selected sequentially for a given J_α^π subspace. The index α represents the number of the state in the J^π subspace. The states are ordered by energy. In the example below this is the first 0^+ -state of ${}^8\text{Be}$. First all n projected diagonal matrix elements H_{ii} are calculated. Again the index $i = (a, \kappa_a)$ represents all combinations of the values a and κ_a and likewise $j = (b, \kappa_b)$. The one with the lowest energy is chosen to be the first member of the Hilbert space.

Figure 4.7 shows the energies with and without angular momentum projection. Again, the effect of the angular momentum projection and the difference between the PAV^π state and a VAP^{GCM} state can be seen. In both cases the states are projected on positive parity. It is an extension of the example from page 38. Here the width a is also used as a parameter. Widths ranging from 1 fm^2 to 3 fm^2 with a step size of 0.1 fm^2 have been used. In total 294 states have been provided. The state, with the parameters $a = 1.9 \text{ fm}^2$ and $d = 4.0 \text{ fm}$, shows the lowest energy $E^{0^+} = -52.21 \text{ MeV}$ after projection. It can be regarded as a VAP^{GCM} state in the two generator coordinates a and d . This state is selected as the first member of the Hilbert space.

The valley emerging from the deepest point for increasing distance d indicates the possibility of a vibrational mode.

After selection of the first state an iterative process is started. The overlap between the states in the Hilbert space and each of the remaining states

$$\mathcal{N}_{n,(a,\kappa_a)}^{J^\pi} = \frac{\langle Q^{(a)}; J^\pi M; \kappa_a | \mathbb{1}_{n-1}^{J^\pi} | Q^{(a)}; J^\pi M; \kappa_a \rangle}{\langle Q^{(a)}; J^\pi M; \kappa_a | Q^{(a)}; J^\pi M; \kappa_a \rangle} \quad (4.111)$$

is calculated. The identity operator $\mathbb{1}_{n-1}^{J^\pi}$ in the Hilbert space spanned by the selected $n-1$ states is defined in (3.42) on page 27. The index a in equation (4.111) indicates the tested intrinsic state. States yielding an overlap $\mathcal{N}_{n,(a,\kappa_a)}^{J^\pi}$ for one κ_a above a certain threshold value are excluded. If no other value is mentioned this overlap threshold is 0.95 throughout this work.

For each of the states $|Q\rangle$ that are not already excluded the lowest eigenvalue of the Hamiltonian is calculated after adding the state to the Hilbert space. Finally the Hilbert space is extended by the state that leads to the largest gain in energy of the state of interest. This state is a Slater determinant $|Q^{(a)}\rangle$. But since all config-

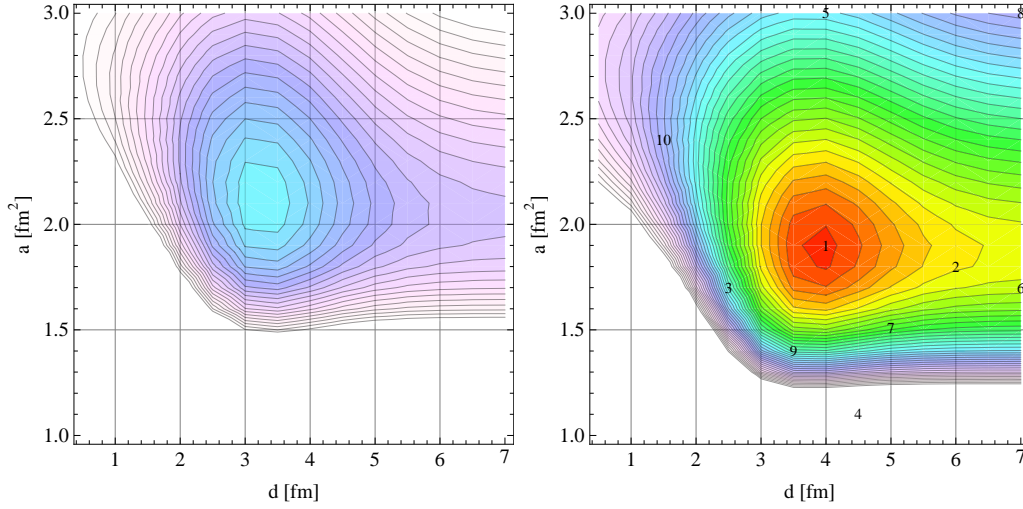


Figure 4.7: Energies of two α particles as function of the width parameter a and the relative distance d . Shown on the left hand side is the energy of the parity projected states and on the right hand side the energy of the same intrinsic states projected on 0^+ . Contour lines are shown from -33.5 MeV to -52 MeV in steps of 0.5 MeV. The graphs shown in Figure 4.5 are cuts through the $a = 2$ fm² plane of these plots.

uration mixing results shown are also projected this Slater determinant $|Q^{(a)}\rangle$ will contribute to the J^π state of interest after projection. Additionally it is projected on the other relevant angular momenta as well and can also contribute to them.

If the gain in energy obtained by adding an additional state is below a threshold the routine stops. When nothing else is stated this energy threshold value is 0.05 MeV. This iterative process is repeated until all remaining states are excluded by the overlap or energy thresholds.

In the left panel of Figure 4.8 the overlap $\frac{|N_{1i}|^2}{N_{11}N_{ii}}$ of all states with the VAP^{GCM} ($i = 1$) state selected first is shown for the example ${}^8\text{Be}$. The index i represents the state at the point in the a - d plane for which the overlap is depicted. The matrix element N_{ij} is the overlap of the angular momentum projected states i and j . It is defined in equation (3.38) on page 27. It can be observed that states with parameters similar to those of the VAP^{GCM} state show large overlaps.

The right hand side panel of Figure 4.8 depicts the energy of the lowest eigenstate of the Hamiltonian in a 2-dimensional Hilbert space spanned by the VAP^{GCM} state and the state described by the two generator coordinates a and d . It is recognizable that states with a large overlap with the VAP^{GCM} state do not result in a significant gain in energy. The same is true for states that are high in energy. A applicable contribution is coming from states that are low in energy and show a small overlap with the selected Hilbert space. As can be seen from Figure 4.8 the state that is the most valuable contribution in terms of the projected energy is

4.6 Selecting states

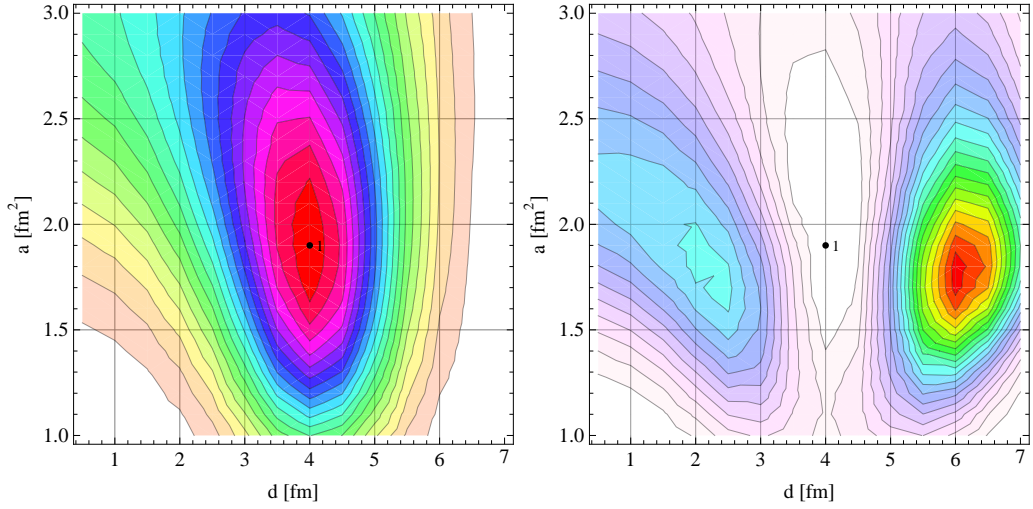


Figure 4.8: In the graph on the left hand side the overlap with respect to the VAP^{GCM} state is shown. On the right hand side the energy calculated by diagonalizing the Hamiltonian in the space spanned by the VAP^{GCM} state and the state that corresponds to the position in the a - d plane after projection on 0^+ is shown. Contour lines are shown from 0.05 to 0.95 in steps of 0.05 for the overlap and from $\Delta E \approx -0.16$ MeV to $\Delta E \approx -2.04$ MeV in steps of ≈ 0.1 MeV for the energy. The numbers on the right hand side indicate the Slater determinant chosen and the order they are chosen in.

described by the parameters $a = 1.8 \text{ fm}^2$ and $d = 6.0 \text{ fm}$. Adding this state to the VAP^{GCM} state Hilbert space results in a new Hilbert space with a 0^+ ground state energy of $E^{0^+} = -54.31 \text{ MeV}$. This is a gain of 2.1 MeV compared to the $E^{0^+} = -52.21 \text{ MeV}$ for the VAP^{GCM} state.

The overlaps and energies that occur when adding the third state to the Hilbert space are shown in Figure 4.9. The third state chosen by this technique has the width parameter $a = 1.7 \text{ fm}^2$ and an α - α distance of $d = 2.5 \text{ fm}$. The 0^+ ground state energy after selecting the third state is $E^{0^+} = -54.87 \text{ MeV}$. One can interpret these three configurations to approximately describe a vibrational degree of freedom.

If the example is continued a total of 10 states are found to contribute to the ground state. This number strongly depends on the overlap and energy thresholds. Using the default thresholds an energy of $E^{0^+} = -55.91 \text{ MeV}$ is obtained finally⁴. In the example the Hilbert space is reduced from 294 states to ten. In terms of the number of matrix elements of the Hamiltonian that have to be evaluated numerically this is a reduction from 86436 matrix elements to 100. During the

⁴In section 5.3 further configurations that are not restricted to these simple cluster-model states are used and lead to a lowest eigenvalue of $E^{0^+} = -57.985 \text{ MeV}$ which is actually somewhat overbound compared to the experimental value of $E^{0^+} = -56.499 \text{ MeV}$

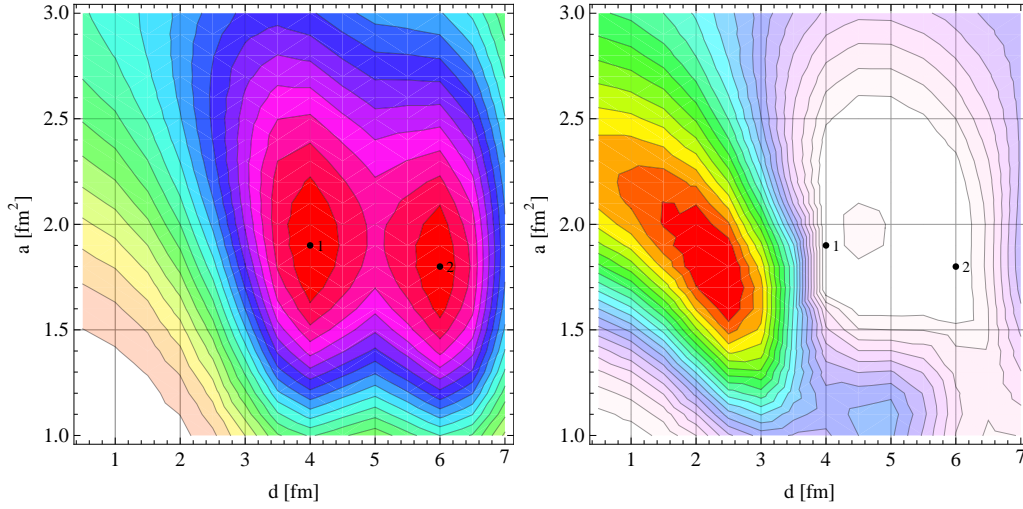


Figure 4.9: In the left graph the overlap with respect to the two states that already span the chosen Hilbert space. In the right plot the energy of a 3-dimensional Hilbert space is shown. This Hilbert space is spanned by the 2-dimensional Hilbert space chosen in the previous iteration and the state that corresponds to the position is shown. Contour lines are shown from 0.05 to 0.95 in steps of 0.05 for the overlap and from $\Delta E \approx -0.03$ MeV to $\Delta E \approx -0.52$ MeV in steps of ≈ 0.025 MeV for the energy.

selection process up to 5780 Hamiltonian matrix elements are needed.

The numerical center of mass projection needs roughly 100 times the computing time that a calculation with the approximate center of mass projection takes. Additionally the sequence of the states usually is barely altered by the center of mass projection. These are the reasons why for the selection only an approximate center of mass projection is applied while finally, after selecting the proper subspace, the full projection is performed.

Figure 4.10 shows the convergence of the energy of the ${}^8\text{Be}$ ground state depending on the number of states in the Hilbert space. It additionally shows the behavior of the first two excited states with $J^\pi = 2^+$ and $J^\pi = 4^+$ using the same intrinsic states $|Q^{(a)}\rangle$ as for the 0^+ ground state. These intrinsic states are projected onto all angular momenta used in the calculation, but only the $J^\pi = 2^+$ and $J^\pi = 4^+$ states are shown. Thus states selected for the 0^+ ground state do also contribute to other J^π states. These ${}^8\text{Be}$ states are known to form a rotational band.

On the right hand side of 4.7 the 10 states chosen are indicated by the number of the state. It can be seen that the third and fourth state are rather compact while the sixth state is very extended. For the 4^+ state compact configurations do not contribute strongly because of the centrifugal barrier. These are shifted high in energy and do barely contribute to the lowest 4^+ state. In Figure 4.10 this effect can be seen. The compact third state does hardly change the energy of the 4^+ state

while the very extended sixth state contributes very strongly.

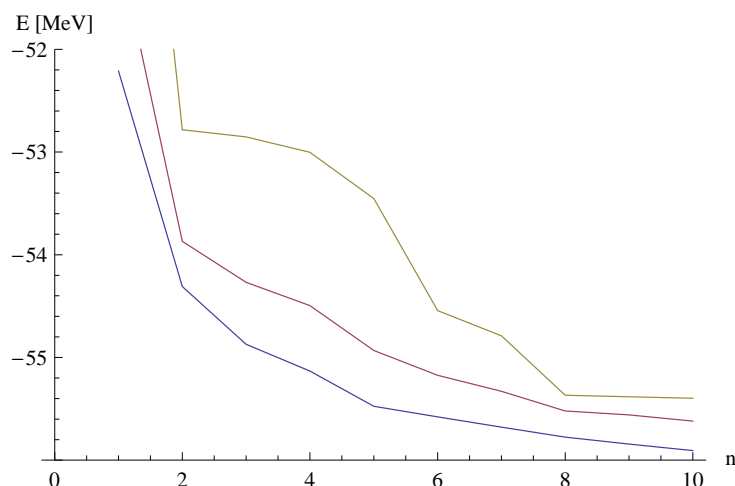


Figure 4.10: Lowest eigenvalues of the Hamiltonian for $J^\pi = 0^+, 2^+, 4^+$ using the Hilbert subspace depending on the number of states n in it. The states in the Hilbert space are the 10 states chosen for the ${}^8\text{Be}$ ground state. The 0^+ ground state (blue), the first 2^+ state (cyan) and the first 4^+ state (yellow) are plotted. The excited states are shifted by 2.5 MeV and 7.5 MeV respectively to show them in the same plot range.

It is possible to start the selection of intrinsic states by expanding an existing fixed Hilbert space. To study the second eigenstate for a given J^π it might be necessary to enlarge the Hilbert space found for the first eigenstate. This is in particular the case if the second state is of different structure than the first one. An example would be the first and the second 0^+ state in ${}^{10}\text{Be}$. In the case of a second 0^+ state a suitable Hilbert space for the first 0^+ state has to be provided first. If for example the second 2^+ differs essentially only in the K quantum number from the first 2^+ it should already be described well with the selection obtained for the first 2^+ .

The scheme used in this work is to start describing the ground state and let the routine add more intrinsic states to the Hilbert space until the remaining intrinsic states are all excluded by the overlap threshold or the energy threshold. In the second step this space is fixed as a starting Hilbert space when selecting the states for an excited J^π state in the spectrum. By doing this only intrinsic states are selected, which are useful in addition to the Hilbert space that was fixed to describe the ground state. Usually the order in which states in the spectrum are selected to be optimally described by this method is to use the expected order. This order can be taken from an experimentally known spectrum or from other considerations like the result of a PAV^π calculation or an already existing configuration mixing calculation for the ground state. Alternatively the Hilbert space can be selected to

describe the physically most interesting states from the spectrum.

4.7 Spanning the Hilbert space

To describe a given nucleus first a Slater determinant is created as a starting point. The parameters of the wavefunctions are selected to be reasonable. This means they should roughly resemble the expected properties of the nucleus and not be too broad or too separated. Finding a suitable starting point is often done by using a Slater determinant that describes a similar nucleus and adding or removing the appropriate amount of protons and neutrons. Alternately it can be done by joining two Slater determinants with a certain relative distance. This is especially useful when describing cluster states. Choosing the right starting point to find a minimum can be crucial.

The PAV^π states for both parities are obtained by minimizing the value of the PAV^π energy functional (4.9). After minimization the variation is repeated up to 14 times with the Slater determinant. The parameters of the Slater determinant are randomly modified before invoking the next minimization process. The strength of this modification is lowered, roughly by a factor of two, each time the minimization process is started. This is done to try to avoid getting in a local minimum or at least find a better one.

If the result seems to be unphysical or describe a different problem the starting point is obtained by a constraint minimization on the lowest possible number of oscillator quanta. Additionally using the single-particle j^2 as a constraint with the appropriate value for the shell model ground state one can obtain a state that corresponds directly to the shell model state. This method is very robust for creating a starting point and also works well even for unbound systems (like ${}^5\text{He}$ or ${}^{13}\text{Be}$, see 5.8). Unconstrained variational methods often resemble the physics of these unbound systems by separating a neutron or a cluster. Such a separated state is not a good starting point since the nucleus to be described often remains separated.

An example of an unphysical result in this context is a state, which was produced out of numerical noise. This can happen if two single-particle states $|q_1\rangle$ and $|q_2\rangle$ are very similar:

$$\frac{|\langle q_1 | q_2 \rangle|^2}{\langle q_1 | q_1 \rangle \langle q_2 | q_2 \rangle} \approx 1.$$

Since $|q_1\rangle \otimes |q_2\rangle \approx |q_2\rangle \otimes |q_1\rangle$ antisymmetrising the product state $|q_1\rangle \otimes |q_2\rangle$ leaves only numerical noise:

$$\mathcal{A}|q_1\rangle \otimes |q_2\rangle = \frac{1}{2} \left[|q_1\rangle \otimes |q_2\rangle - |q_2\rangle \otimes |q_1\rangle \right] \approx 0 \quad (4.112)$$

To calculate an expectation value the (pseudo-)inverse \mathbf{o} of the overlap matrix \mathbf{n} is needed. Inverting an overlap matrix that contains aforementioned tiny antisymmetrized states and numerical noise of the same order leads to unwanted results.

A typical example for a state that describes a different system is when at least one nucleon is far (≈ 10 fm) away from the others. Such an intrinsic state is not useful to describe the low-energy spectrum in the bound state approximation, which is used in this work for every resonance. This is also the reason why a decay width or time cannot be estimated.

If a set of different states is created using the oscillator quanta constraint the lowest possible number of oscillator quanta is used first. Intrinsic states are created to obey this number and up to 10 quanta more in steps of one. This choice is very natural since it represents the lowest excitations for the oscillator quanta constraint. For other constraints like the radius and the multipole moments it is not that natural how c_j is chosen. These are either chosen by experience or by using variations of the PAV^π states. Choosing the values the constraint is supposed to have c_j by experience means for example the radius is chosen from 2.0 fm to 3.0 fm for light nuclei. For halo nuclei 2.5 fm to 3.5 fm are reasonable values. Choosing these values c_j variations of the PAV^π means the expectation value of the corresponding operator is calculated using the PAV^π and a set of states is created with a c_j that is 40%, 60%, 80%, 120%, 140% or 160% of the calculated value.

As described in section 4.6 a subset of these states is selected, that describes the low energy spectrum. This selection of states is used to span the Hilbert space as described in section 4.2.

Results

5.1 Beryllium

The Beryllium isotopes have the special property that shell model like and cluster model like states appear [vFKE06] in their excitation spectra at a similar energy region. Since $Z = 4$ is close to the middle of the proton p -shell the Beryllium isotopes are typically deformed. This can also be observed by the splitting of the energy levels found by deforming the potential. Due to this influence from the protons the neutron distribution can also become deformed. This effect continues even for the neutron number $N = 8$ which is “magic” for a spherically symmetric potential.

With a binding energy of more than 7 MeV per nucleon [AWT03] the α -particle is much tighter bound than neighboring nuclei. Its energy is below every $A = 5$ system and the energy of two α -particles is below every $A = 8$ system. Thus no stable elements with $A = 5$ or $A = 8$ exist.

Having a first excited state at more than 20 MeV the α -particle is also a very rigid object. It has no particle stable excited state. Thus it will hardly deform or excite under normal perturbations. The Beryllium isotopes with $A \geq 8$ are therefore predestined to show strong $\alpha + \alpha$ -clustering already in energetically low lying states.

All other clusters such as a deuteron, triton, ${}^3\text{He}$ or a ${}^6\text{He}$ cluster are theoretically also possible, but since their binding energy is significantly higher they are in general rather high in energy.

Similar to atomic physics where two atoms can form a covalently bound diatomic molecule [Her50] Beryllium isotopes with $A \geq 9$ can be described as two α -particles hold together by one or more valence nucleons [vFKE06]. In close analogy to molecular physics the valence nucleon orbits are called σ -orbits if the valence particle is aligned with two (α) clusters and π -orbits if not. Theoretically

5.1 Beryllium

	$1n$	$2n$	$3n$	p	α
${}^7\text{Be}$	10.676			5.606	1.586
${}^8\text{Be}$	18.900	29.667		17.255	-0.092
${}^9\text{Be}$	1.665	20.565	31.332	16.888	2.464
${}^{10}\text{Be}$	6.812	8.478	27.337	19.637	7.413
${}^{11}\text{Be}$	0.503	7.316	8.982	20.165	8.352
${}^{12}\text{Be}$	3.169	3.673	10.485	23.010	8.946
${}^{13}\text{Be}$	-0.100	3.069	3.573	24.138	10.117
${}^{14}\text{Be}$	1.365	1.265	4.434		11.280

Table 5.1: Particle thresholds in MeV. Data taken from [TKG⁺04, TCG⁺02] or calculated using masses from [AWT03]. Missing values are due to missing masses for the tetraproton “ ${}^4\text{Be}$ ”, “ ${}^5\text{Be}$ ” and “ ${}^{13}\text{Li}$ ”.

these molecular orbits can hold 12 valence particles of which 6 would be “antibinding”¹. This implies that this simple analogy to atomic physics predicts all Be isotopes heavier than ${}^{14}\text{Be}$ to be neutron unstable.

The oscillator constraint does not distinguish the $p_{3/2}$ and the $p_{1/2}$ shell. To describe the Be isotopes in FMD the oscillator constraint acting only in the proton shell N^p is not used as often as N^n to create intrinsic states with significantly more excitation. Beryllium isotopes are in a shell model picture expected to fully occupy the $0s$ proton shell and to have two protons in the $p_{3/2}$ shell in the lowest lying states. Moving a $p_{3/2}$ proton into the sd shell leads to intrinsic states that are high in energy. Hence these do not strongly contribute to states in the low energy spectrum.

On the other side it is possible to describe every Be isotope in a cluster picture. Separating two charged clusters in coordinate space from each other results in a higher number of oscillator quanta in the proton shell. This contribution is generally less than $\Delta N^p = 0.5$ for the ground state. In the calculation this is often explicitly included using some intrinsic states that were created while applying the N^p constraint.

The main use of the N^p constraint is in combination with N and N^n to keep all nucleons in the lowest shells. For a state minimized by applying this combination of constraints two protons fill the first s shell and two are in the p shell. By additionally restricting the value of the single-particle j^2 these nucleons can be forced to be in the $p_{1/2}$ or $p_{3/2}$ shell or a mixture of both. This procedure is used to create states that account for these shell model like proton excitations. The usage

¹The term antibinding should not be misinterpreted here. It refers to the common notation known from chemistry and only says that the energy of this molecular orbit is higher than the energy of the corresponding atomic orbits.

of N , N^p and N^n at the same time increases the convergence of the minimization.

All FMD states used here to describe the Beryllium isotopes use two Gaussians per nucleon.

5.2 Beryllium-7

${}^7\text{Be}$ is the only Beryllium isotope studied in this work that cannot have an $\alpha + xn + \alpha$ substructure. x is here a positive integer or zero. The ${}^7\text{Be}$ nucleus decays in the presence of electrons via electronic conversion to the ground or the first excited state of ${}^7\text{Li}$.

In a cluster picture ${}^7\text{Be}$ is described as ${}^3\text{He} + \alpha$. A detailed investigation on applying FMD, to describe the first two resonances of ${}^7\text{Be}$ properly, as well as a calculation of the cross section of the ${}^3\text{He}(\alpha, \gamma){}^7\text{Be}$ reaction, can be found in [Cri05] and [Cus08].



Figure 5.1: Depiction of the intrinsic densities of the 13 states that were used for the description of ${}^7\text{Be}$. The sixth state was minimized in a $\text{PAV}^\pi = -1$ sense using a constraint on a quadrupole moment of zero.

The number of Slater determinants provided for the description of ${}^7\text{Be}$ is 55. As no low lying positive parity states are expected, only three intrinsic states were minimized as $\text{PAV}^{\pi=+}$ states. Additionally only the two $\text{PAV}^{\pi_p \pi_n}$ states exhibiting negative total parity were supplied. 20 of the negative parity states were minimized with a constraint on oscillator quanta N or oscillator quanta in the neutron

5.2 Beryllium-7

shell N^n . 15 states with different (electrical) dipole moments and five states with higher mass multipoles are used.

Four of the supplied states were created as shell model p states. In this case all three oscillator quanta constraints were applied to obtain shell model ground state like configurations. Additionally a constraint on the single particle j^2 was used. The shell model states that have been used are the possible combinations in the $p_{3/2^-}$ and $p_{1/2^-}$ -shells. Since the j^2 constraint does not distinguish between protons and neutrons the number of these combinations is four. The values for the j^2 constraint were chosen to be the same as in a shell model state with three, two, one or zero nucleons in the $p_{3/2^-}$ -shell. By calculating the harmonic oscillator occupation numbers it can be seen that the intrinsic FMD states, that are supposed to represent a shell model state in which all nucleons are in the $p_{3/2^-}$ or $p_{1/2^-}$ -shell, accord very well with the shell model states. The FMD states for which j^2 was chosen to correspond to a shell model configuration in which one nucleon is in the $p_{3/2^-}$ or $p_{1/2^-}$ -shell do not resemble shell model states but are a mixture of the $p_{3/2^-}$ and $p_{1/2^-}$ shell model states.

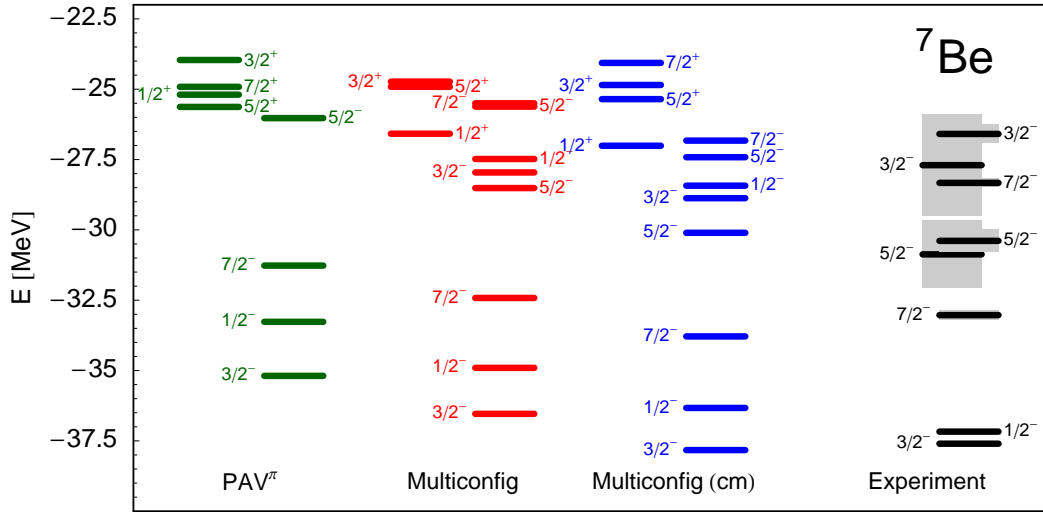


Figure 5.2: ${}^7\text{Be}$ energy levels. The states labeled PAV^π were obtained using only the two PAV^π states. States labeled *Multiconfig* are the result of a configuration mixing calculation using states which are approximately projected on the center of mass. While states labeled *Multiconfig (cm)* are projected numerically on the center of mass. The experimental values are taken from [TCG⁺02]. Experimentally known states with very high excitation energy and very short lifetime might have been omitted.

The basis was successively selected to describe the low lying spectrum. First five intrinsic states were added to the Hilbert space to describe the $3/2^-$ ground state. The second step was using the $3/2^-$ Hilbert space and trying to find more

states to add and improve the description of the $1/2^-$ state in the spectrum. In this second step all intrinsic states were excluded by one of the thresholds i.e. no states were added. Thirdly three states were added to account for the structure of the $7/2^-$ state. Finally two and three states were added to enhance the description for the $5/2_1^-$ and $5/2_2^-$ states respectively. The spectrum coming from this description is shown in Figure 5.2 in red.

The Hilbert space finally used is not optimized for the other states like the ones with positive parity for example. Nevertheless positive parity states are obtained in the final calculation. Positive parity states would be better described if more positive parity intrinsic states were included. Due to the fact that these states are in the continuum and seem to be unobserved in experiments one may presume that they are broad resonances that need a more intricate description than the bound state approximation. This is underlined by the fact that some positive parity states have large amplitudes from wide intrinsic states. These states will probably move higher in terms of energy if treated properly using boundary conditions. From table 5.1 a ${}^3\text{He} + \alpha$ structure appears most probable.

The best single FMD Slater determinant to describe the ground state is the $\text{PAV}^{\pi=-1}$ state that was minimized using the interaction with $\lambda_{LS} = 50\%$. Of the 13 states four were created using a constraint on the total number of oscillator quanta, two using only neutron shells, and one by constraining the number of oscillator quanta in the proton shells. In addition to one radius- and two quadrupole-constrained states the two aforementioned states with one nucleon in p -shell were also chosen.

In Figure 5.2 the energy levels of the PAV^π calculation and the angular momentum projected configuration mixing calculations are shown. In all similar Figures in this work the results labeled as PAV^π are actually also coming from a multiconfiguration calculation using only the two intrinsic FMD states that were generated by minimization on positive and negative parity. In general the contribution of a state that was minimized after projection on the parity π is negligible if projected on the opposite parity $-\pi$. Thus this method gives only slightly improved results which are very similar to a PAV^π calculation without configuration mixing.

It can be seen that by increasing the dimension of the Hilbert space and applying a numerical center of mass projection the energies of the states decrease. However, the energy splitting of the individual states does not change much. It especially does not seem to converge toward the experimental values. This is a known issue, which is caused by the $\vec{\tilde{L}} \cdot \vec{\tilde{S}}$ correction term of the interaction and can also be seen in the spectra of other Be isotopes presented in this work.

Using an interaction with less $\vec{\tilde{L}} \cdot \vec{\tilde{S}}$ splitting results in better agreement with the experimentally observed splitting. Thus the calculation was repeated using the same Hilbert space but an interaction where the strength of the $\vec{\tilde{L}} \cdot \vec{\tilde{S}}$ correction term is reduced to a quarter of its original value. From Figure 5.3 it can be seen

5.3 Beryllium-8

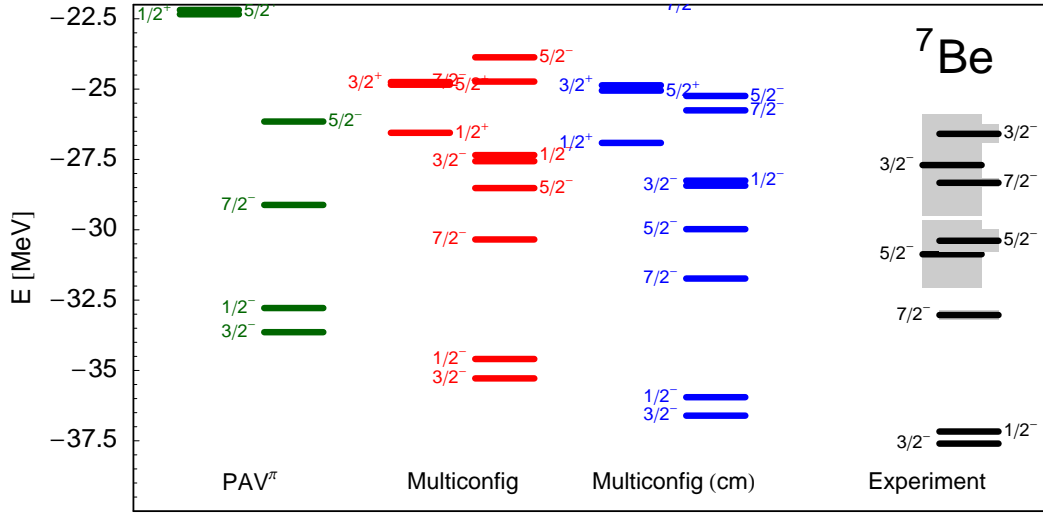


Figure 5.3: ${}^7\text{Be}$ energy levels calculated using an interaction with the $\vec{L} \cdot \vec{S}$ correction term reduced to 25% of the full strength. States labeled PAV^π were obtained using only the two PAV^π states. States labeled *Multiconfig* were approximately projected on the center of mass and states labeled *Multiconfig (cm)* were projected numerically on the center of mass.

that the splitting of the $3/2^-$ ground state and the first $1/2^-$ is significantly reduced and the agreement with the experimentally found energies improves. In general the *ab initio* approach is preferred and Figure 5.3 is meant as example or estimation of an outlook for interactions that might be used in the future.

5.3 Beryllium-8

${}^8\text{Be}$ is particle unbound. Within the $N = Z$ nuclei ${}^8\text{Be}$ is the only unstable nucleus with $A < 18$, the only unstable even-even nucleus with $A < 40$ and the only particle unstable even-even nucleus with $A \leq 100$.

The ground state is a 0^+ resonance only 0.0918 MeV above the $\alpha + \alpha$ threshold. The first 2^+ and the first 4^+ state are related to a rotation of the deformed 0^+ ground state resonance. Since ${}^8\text{Be}$ has an axis ratio of 2 : 1 it is called the first superdeformed nucleus [von03]. Like most of the Be isotopes ${}^8\text{Be}$ shows a prolate deformation. In the Nilsson model four is predicted to be a “magic” number in a deformed harmonic oscillator that has an axis ratio of 2 : 1 [BM75]. All Be isotopes would be “magic” in the proton shell at this axis ratio. ${}^8\text{Be}$ would even be doubly magic in that sense.

Above 17 MeV excitation energy shell model like narrow states are observed. Due to their different structure these states generally do not decay into two α 's but

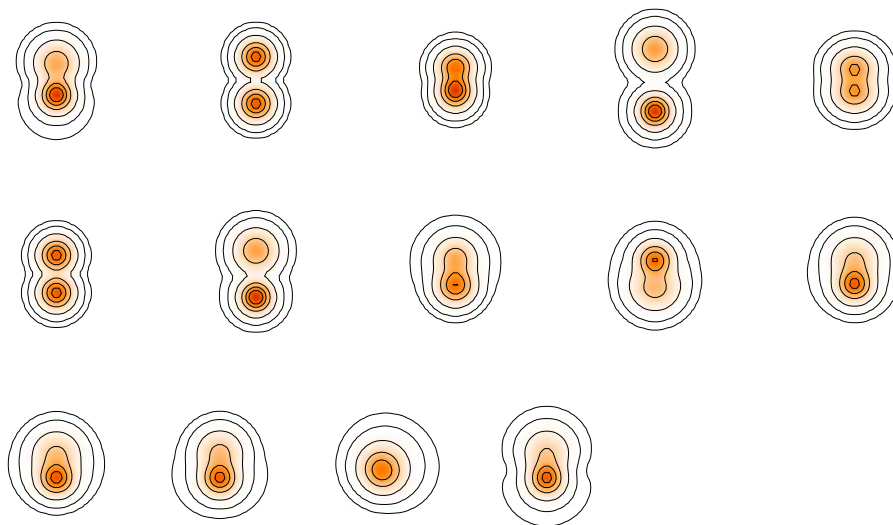


Figure 5.4: Depiction of the intrinsic densities of the 14 states that are used for the description of ${}^8\text{Be}$

by emitting a γ , proton or neutron.

In a p -shell calculation the ground state band was already described moderately well in 1965, but two still unobserved states, an additional 1^+ , $T = 0$ state and a 2^+ , $T = 0$ state at roughly 14 MeV are also found [CK65].

104 states are used in case of ${}^8\text{Be}$. These contain the mean-field state, the $\text{PAV}^{\pi=+1}$ state and the two $\text{PAV}^{\pi_p\pi_n}$ states with positive total parity. A $\text{PAV}^{\pi=-1}$ was not included since all attempts to create one ended up in a ${}^7\text{Be}+n$ configuration with rather large distance. Eleven α cluster states were created by placing two α clusters at a relative distance d . d is chosen to be less than 5 fm to try to avoid states that lie in the continuum. The α used was created as a shell model ground state by using the N^p , N^n , j^2 and projecting on positive parity. In a harmonic oscillator with a frequency of $\hbar\omega = 23.302$ MeV this state shows 100% occupation of the $0s$ levels.

100 states are created by enforcing different constraints during minimization. A large number of these were created by combining different λ_{LS} and a constraint on the number of oscillator quanta. Radius and quadrupole constrained intrinsic states are also included. To describe the excited shell model like $T \neq 0$ and $S \neq 0$ states in ${}^8\text{Be}$ a combination of the \tilde{S}^2 and \tilde{T}^2 constraint was used. Slater determinants with large radii have been excluded. These are known to be able to form two separated α clusters which can yield every energy above the α - α threshold.

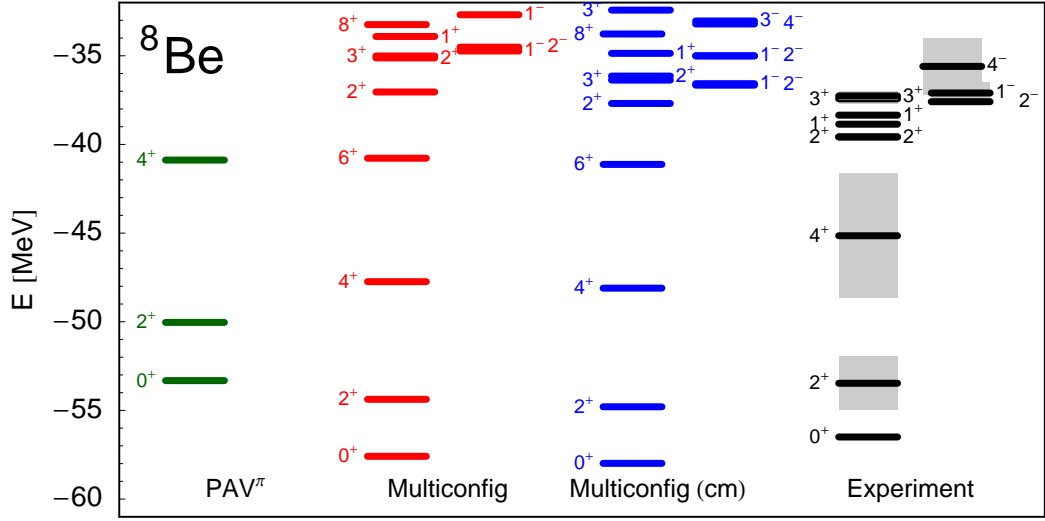


Figure 5.5: ${}^8\text{Be}$ energy levels. The states labeled PAV^π are obtained using only the $\text{PAV}^\pi = +1$ state. States labeled *Multiconfig* are approximately projected on the center of mass and states labeled *Multiconfig (cm)* are projected numerically on the center of mass.

From this set 7 Slater determinants were selected to describe the ground state. These are four N constrained intrinsic states of which two are combined with λ_{LS} , two α cluster states and the Slater determinant that was constrained on $R = 2$ fm. Other J^π states that are explicitly included in the calculation are the first 1^+ state, the 1_2^+ state, the first 3^+ state and the negative parity ground state, the 2^- state. To describe these three, two, one and again one Slater determinant are selected respectively. Most of these Slater determinants were spin- and isospin-constrained. The penultimate intrinsic state in Figure 5.4 is asymmetric. It was created to have a quadrupole moment of zero but higher multipole moments are not zero.

The ground state rotational band is relatively well reproduced. The second and third 0^+ are too low because they already lie in the $\alpha - \alpha$ continuum and are not properly described without the use of boundary conditions. These states, as well as the rotational bands build on them, are omitted in Figure 5.5 since they cannot be properly described in the bound state approximation. The narrow shell model like states can only be properly described by using the Slater determinants that were created using \tilde{S}^2 and \tilde{T}^2 as a constraint. If these are not provided the energy of these states is roughly 5 MeV higher.

The first 3^+ is one of the shell model like states. In the calculation it is located 22.575 MeV above the ground state. When studying the occupation numbers one can see that the $0s$ shell is almost filled, the $p_{3/2}$ proton and neutron shells have an occupation of 1.83 each and the $p_{1/2}$ proton and neutron shells show an

occupation of 0.12 each. Higher shells are hardly filled, the sd and the pf shell show occupation numbers of less than 0.05.

A comparison with the 0^+ ground state shows that proton and neutron shells are filled in a very similar way. This is due to the fact that the ground state is much more cluster like and the two α clusters show these similar occupations of proton and neutron shells. The proton occupation in the s shell is 1.56, in the $p_{3/2}$ shell 1.36 and in the $p_{1/2}$ shell 0.48. The sum of all proton occupation numbers in the sd shell is 0.41 and for the pf shell it is 0.16.

When comparing these two states one can see that the total occupation for the 3^+ state in the s and $p_{3/2}$ shell is 7.54 whereas for the ground state it is only 5.85. The total occupation outside the s and the p shell is 0.23 in case of the 3^+ state and 1.21 for the ground state. Since this occupation originated equally from protons and neutrons it cannot be interpreted as a single nucleon outside a core

5.4 Beryllium-9

${}^9\text{Be}$ is the only Beryllium isotope that is stable with respect to beta decay. It is a *Borromean*² nucleus. This means the $3/2^-$ ground state is bound, consists of three constituents and any combination of two of them is unbound. In ${}^9\text{Be}$ the constituents are $\alpha + n + \alpha$ and all possible combinations of two constituents can only form the particle unstable ${}^5\text{He}$ or ${}^8\text{Be}$. Since ${}^8\text{Be}$ is unbound the lowest particle decay threshold in ${}^9\text{Be}$ is the $\alpha + \alpha + n$ threshold at 1.57 MeV.

${}^9\text{Be}$ is sometimes described in a molecular picture. In this picture the two α -particles are bound together by a valence neutron like in atomic or molecular physics where two protons can be bound to H_2^+ by adding a valence electron³. The valence neutron, which binds two α particles is in a molecular orbit [vFKE06]. For the ground state this orbit is a σ -orbit. Two neutrons can fill the same σ -orbit. This also explains why ${}^8\text{Be}$ is not bound while ${}^{10}\text{Be}$ is more tightly bound than ${}^9\text{Be}$ in terms of energy and spacial dimensions.

Deformed shell model calculations have proven useful for ${}^9\text{Be}$.

For the characterization of ${}^9\text{Be}$ in FMD a total of 140 Slater determinants are supplied. 63 of these were created by applying a combination of the oscillator quanta constraint and interactions with different $\tilde{L} \cdot \tilde{S}$ strengths in the correction term. The excitation in proton or neutron shells is constrained for 13 states in each

²In knot theory the general term Brunnian link is used for any set of nontrivial links of n loops if all the subsets consisting of $n - 1$ loops are trivially unlinked [CAA⁺08]. The Borromean rings are the easiest and most famous special case of a Brunnian link.

³Besides the obvious differences like the masses and the interaction the main difference is that the protons in H_2^+ are spin 1/2 fermions while the α particles in ${}^9\text{Be}$ are spin 0 bosons. He_2^{3+} is not used as an example here since it not such a descriptive textbook example as H_2^+ .

5.4 Beryllium-9

case. 18 states were constrained on radii from 2.1 fm to 3.3 fm. A quadrupole constraint is restricting the parameters of 12 states while 11 are made to obey certain octupole moments. Five states obey the same excitation and single-particle \vec{j}^2 as the five possible shell model p -state configurations.

In Figure 5.6 one can see the densities of the intrinsic states that are selected to span the Hilbert space. The first eight states were selected to describe the $3/2^-$ ground state while the other five are selected to improve the first $1/2^+$ state.

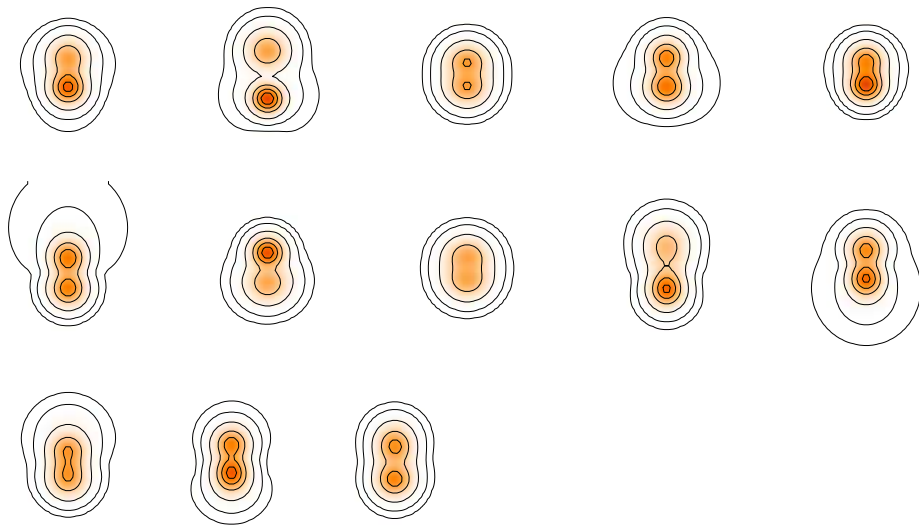


Figure 5.6: *Densities of the 13 intrinsic states that are used for the description of the ${}^9\text{Be}$ spectrum*

Although the 13 states in the Hilbert space were only selected to describe the lowest states for each parity a wealth of states is found in the final calculation (see Figure 5.7).

By comparing the harmonic oscillator occupation numbers of the positive and negative parity ground states it can be seen, that the occupation of the $p_{3/2}$ neutron shell is 2.34 in the $3/2^-$ state and 1.44 for the $1/2^+$ state. On the other hand an occupation of many also high-lying s shells is observed in the $1/2^+$ state. This is in general an indication of the existence of a neutron halo. The neutron point density distribution shown in Figure 5.20 on page 89 underlines the interpretation of a neutron that is excited from the $p_{3/2}$ in a halo orbit.

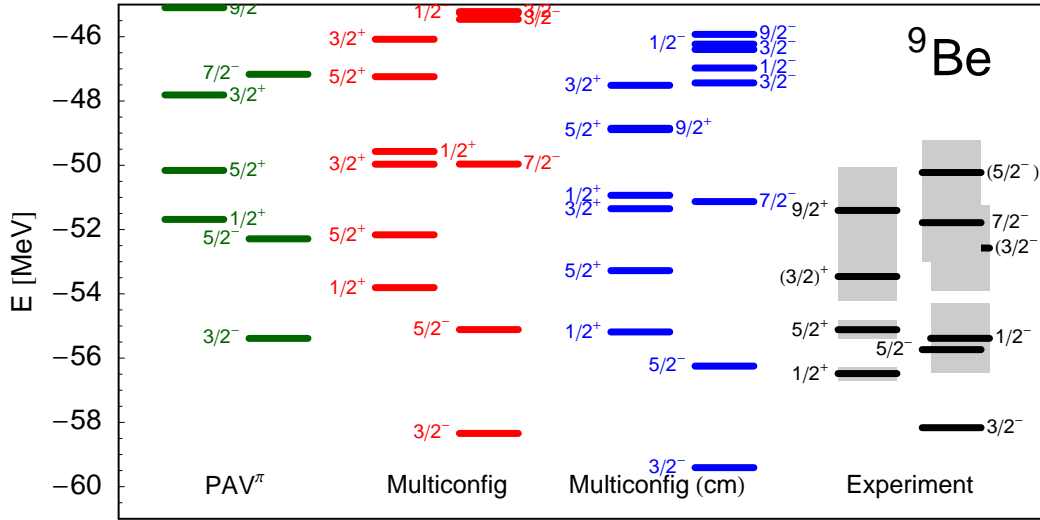


Figure 5.7: ${}^9\text{Be}$ energy levels. The states labeled PAV^π are obtained using only the two PAV^π states. States labeled *Multiconfig* are approximately projected on the center of mass and states labeled *Multiconfig (cm)* are projected numerically on the center of mass.

5.5 Beryllium-10

The ${}^{10}\text{Be}$ ground state is more tightly bound than ${}^9\text{Be}$. This can be seen by comparing the energies and the proton and neutron radii which become smaller by adding the additional neutron. ${}^{10}\text{Be}$ is particle stable but unstable with respect to β^- decay. It is said that the ground state forms a rotational band that includes the 2_1^+ state. However the associated 4^+ member was never observed [BDK⁺07]. Experiments using one-nucleon transfer reactions observe that these two states are strongly populated. This suggests similarities in the structure of these two states and the ${}^{10}\text{Be}$ neighbors in their ground states [MSB⁺02].

The 0_2^+ level at 6.18 MeV was predicted to be the molecular-type (σ^2) state [von97]. Simple shell-model configurations fail to describe it [vG84, WvG90, WB92]. Admixture of $2\hbar\omega$ states significantly improve the energy of the calculated state. Therefore it is considered to be an intruder state. The rotational band associated with this state includes the 2^+ state at 7.54 MeV and probably the state at 10.15 MeV which is expected to be a 4^+ state. The 10.15 MeV state shows a significant cluster structure that is as well developed as in the ${}^8\text{Be}$ ground state rotational band. Its probability to decay into the ${}^9\text{Be}_{\text{g.s.}}$ is much lower than naively expected [FCA⁺06]. The very small spectroscopic factor $S = 0.03$ of the 0_2^+ state in the ${}^9\text{Be}_{\text{g.s.}} + n$ channel also suggests the 0_2^+ state to be an intruder [Mug85].

Ito *et al.* are using a generalized two-center α cluster model to describe ${}^{10}\text{Be}$ and its excited states [IYKI05, Ito06]. Four 0^+ states within the first 15 MeV are

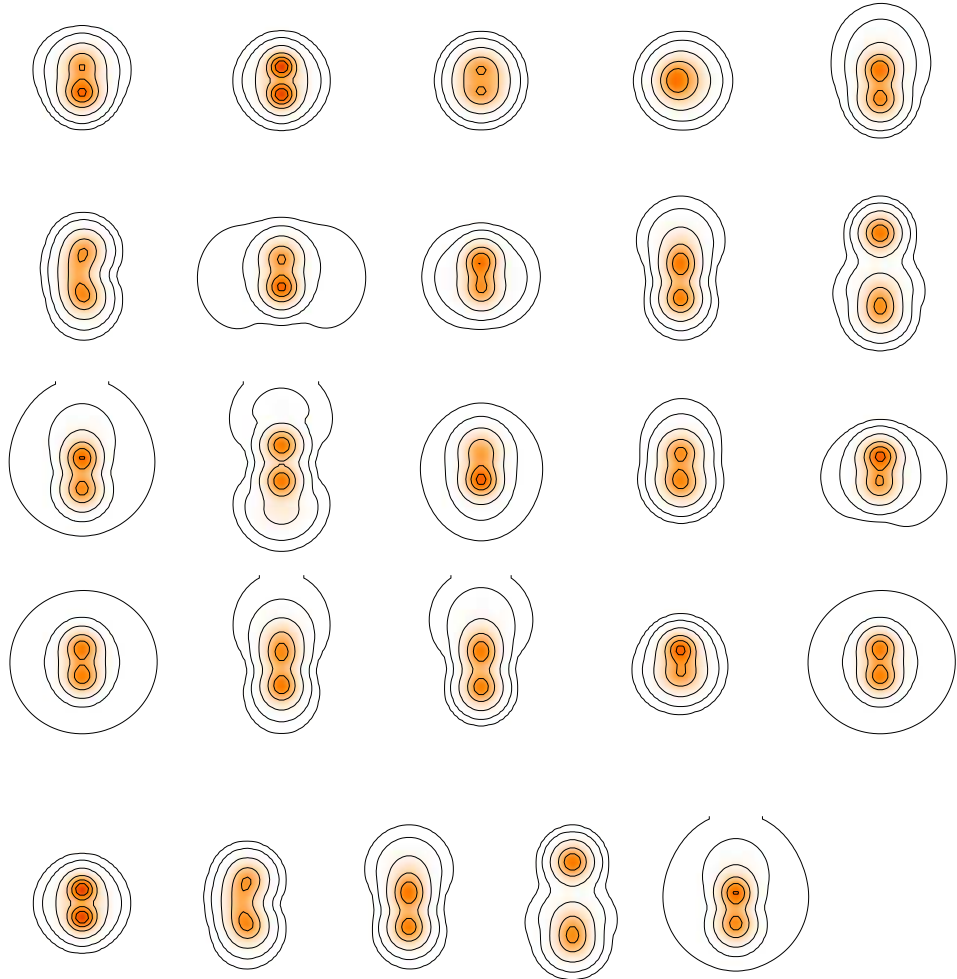


Figure 5.8: *Depiction of the intrinsic densities of the 25 states that are used for the description of the ^{10}Be spectrum*

found. The second 0^+ state is confirmed to be of molecular $(\sigma_{1/2}^+)^2$ nature. The first and fourth state are described in terms of molecular orbitals as $(\pi_{3/2}^-)^2$ and $(\pi_{1/2}^-)^2$ respectively. The third 0^+ state is different. It has an admixture with a $\alpha + {}^6\text{He}(2^+)$ structure.

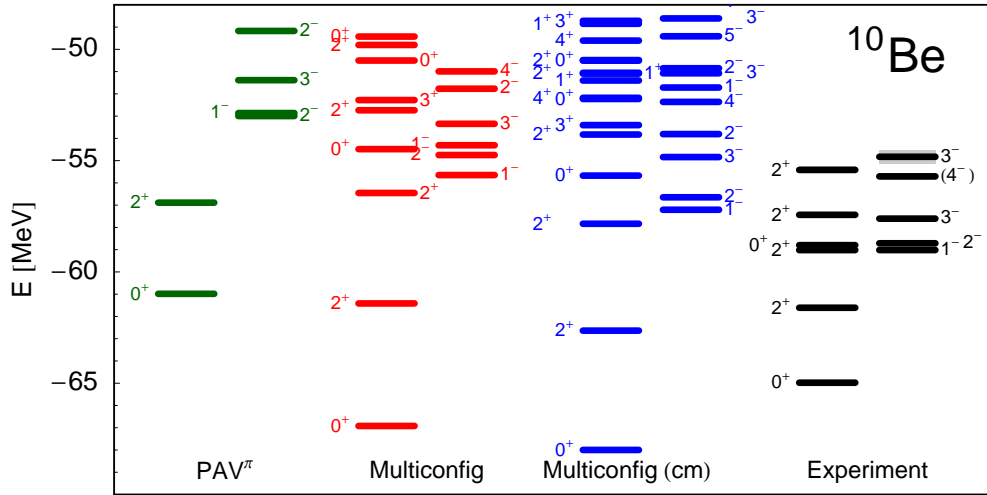


Figure 5.9: ${}^{10}\text{Be}$ energy levels. The states labeled PAV^π are obtained using only the two PAV^π states. States labeled *Multiconfig* are approximately projected on the center of mass and states labeled *Multiconfig (cm)* are projected numerically on the center of mass.

For the description of ${}^{10}\text{Be}$ a total of 94 Slater determinants were supplied. From these 45 were constrained by a combination of N and different λ_{LS} . The oscillator constraints acting only protons or neutrons were not combined with λ_{LS} thus a total of four and seven intrinsic states were created respectively. By combining N and the single particle j a shell model like ground state has been created. Its occupation numbers show only a tiny $d_{5/2}$ admixture in a harmonic oscillator with $\hbar\Omega = 16.4$ MeV. 12, eight, four and three intrinsic states were constrained on their dipole, quadrupole, octupole moment or radius respectively. The mean-field state, the two PAV^π states, a VAP 0^+ state and two α cluster states were also supplied. Most of these Slater determinants were projected on positive parity, only ten were minimized after projection on negative parity.

In this work ${}^{10}\text{Be}$ is described using a set of 25 Slater determinants. These are selected as the best representation for the first 0^+ state, the first 1^- state, the first 2^+ state and the 0_2^+ state. Again a large variety of additional states is found which might get improved by using a larger basis that was also optimized for them.

5.6 Beryllium-11

The ^{11}Be ground state is a $1/2^+$ state. In the simple $0\hbar\omega$ shell model the lowest state would be a $1/2^-$ state thus the actual ground state is called an intruder state. Due to the very low binding energy of the last neutron 0.503 MeV the corresponding single-particle state is very wide spread and therefore called an archetype of a halo nucleus [SPO⁺07]. The $1/2^-$ state is denoted as a p -shell state and is located 0.32 MeV above the ground state [TKG⁺04]. These two states are the only known particle bound states in ^{11}Be .

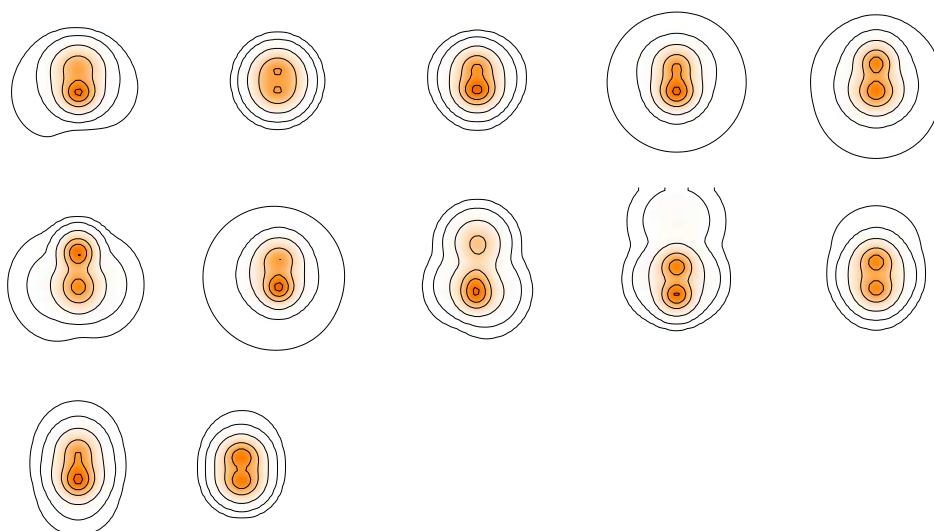


Figure 5.10: Densities of the 12 intrinsic states used for the description of the ^{11}Be spectrum.

The E1 transition between these two bound states is the strongest known transition between low-lying states [FNOC05]. The data has first been published in [MOWH83].

The recent no core “large basis *ab initio* shell model investigation of ^9Be and ^{11}Be ” [FNOC05] states a linear increase of the E1 strength with the model space. Their $9\hbar\omega$ “result is far from converged”. The experimental value is $0.116(12)e^2 \text{ fm}^2$ while the NCSM calculation returns the 18 times lower value $0.0065e^2 \text{ fm}^2$. Extrapolation of the energy of the $1/2^+$ state indicates that a convergence of its energy in the shell model might be achieved at $\approx 30\hbar\omega$ model space size but the correct level ordering is still off by $\approx 1.5 \text{ MeV}$. The $B(E1)$ transition strength obtained in the FMD calculation is $0.026 e^2 \text{ fm}^4$.

The selection of Slater determinants to span the Hilbert space for the description of ^{11}Be is different from the techniques used for other nuclei. The main difference is that most effort was made to describe the ground state for positive parity. To do this a set of intrinsic states with positive parity was created first and the most relevant states were selected. For comparison with the negative parity ground state the same was done for negative parity. Since the negative parity ground state is a shell model like ground state while the positive parity ground state has features of clusterisation and a halo a larger basis is needed to properly describe the positive parity. Due to this it becomes complicated to describe both parities on a similar level. To describe both parities on a similar level and to be able to quantitatively compare both ground states more elaborate VAP states were finally included to improve the description of the $1/2^+$ and the $1/2^-$ state.

A set of 74 Slater determinants was created in order to describe the positive and negative parity ground states. 47 of these were minimized while restricting the parameter space to certain numbers of oscillator quanta in combination with different λ_{LS} . For each parity five intrinsic states were minimized with a constraint on the radius and two Slater determinants with a constraint on their octupole moment. For the positive parity two intrinsic states were created which obey certain quadrupole moments and four Slater determinants with different λ_{LS} and without further constraints. The PAV^π states are also included. For each parity two VAP states were minimized. Since VAP states are not fully minimized, due to their increase of computing time, two VAP states are obtained per parity. This way four different VAP states and 2 PAV^π states are included.

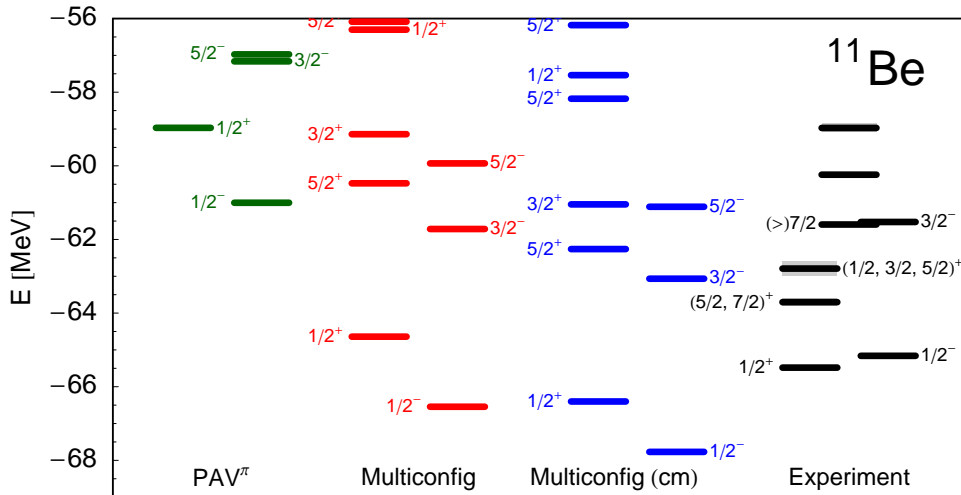


Figure 5.11: ^{11}Be energy levels. The states labeled PAV^π are obtained using only the two PAV^π states. States labeled Multiconfig are approximately projected on the center of mass and states labeled Multiconfig (cm) are projected numerically on the center of mass.

Most occupation numbers of the harmonic oscillator are close to the shell model ground state. The differences worth mentioning are for the $1/2^-$ state an occupation of the $0p_{1/2}$ proton shell of 0.182 and an occupation of the $1p_{3/2}$ and $1p_{1/2}$ neutron shells of 0.11 and 0.15 respectively. The $1/2^+$ state shows more significant differences when compared to a shell model ground state. The occupation of the proton $0p_{1/2}$ shell is 0.28. It can be interpreted as an indicator of the deformation in the alpha distribution. The total occupation of the neutron p shell is 3.76. The highest probability to find this neutron is in the $1s$ (occupation of 0.36) or the $2s$ (0.19) shells. The $1p_{3/2}$ (0.13) and the $d_{5/2}$ (0.08) follow. The occupation outside the first five major shells is 0.42.

The shell model ground state with positive parity is obtained from the negative parity shell model ground state by lifting a neutron from the $p_{1/2}$ shell into the $d_{5/2}$ shell. In the FMD calculation this neutron occupation is 80% from the $p_{1/2}$ and 20% from the $p_{3/2}$ shell. In the shell model picture it mainly goes into a coherent superposition of many higher lying s shells. The $d_{5/2}$ contribution is also enlarged by a factor of three in comparison to the negative parity state, but the contribution is still very small. This can mean that it is an s shell in an oscillator with a different oscillator frequency.

The experimentally known level ordering could not be reproduced in a calculation that aims at a description that shows similar thoroughness for both parities. However it is known from other calculations, that a halo state needs a more thorough description than a state that is shell model like. The angular momentum and center of mass projected VAP state that was optimized on the $1/2^-$ state has an energy expectation value for the $1/2^-$ state 2 MeV below the experimentally known value of the ^{11}Be ground state. Thus it is not unexpected that the $1/2^+$ state could not be described in a way that makes it the ground state.

Repeating the diagonalization as in section 5.2 with the same Hilbert space and the interaction with 25% of the $\vec{L} \cdot \vec{S}$ correction term does barely change the splitting.

5.7 Beryllium-12

^{12}Be is also particle stable, but unstable with respect to β^- decay. The number of neutrons in ^{12}Be is the “magic number” $N = 8$ but unlike heavier isotones ^{12}Be does not seem to have a closed neutron shell.

Assuming a prolate deformation with an axis ratio of roughly 1 : 2 shows that in the Nilsson model [Nil55, BM75] one of the $d_{5/2}$ levels is coming down very strongly. From a Nilsson model point of view $N = 8$ cannot be expected to show any shell closure at large prolate deformation. The deformation is caused by the strong α clustering [von03]. The last neutron pair is stated to be dominantly in

the ($1s^2 + 0d^2$) intruder configuration [NAA⁺00, KEH03]. In close analogy to the ^{11}Be ground state this is not unexpected. A second 0^+ state at 2.24 ± 0.02 MeV was found recently. Its existence underlines the missing of the “magic” neutron number $N = 8$ [SOD⁺07].

In highly excited states $^6\text{He}+^6\text{He}$, $^5\text{He}+^7\text{He}$ or $\alpha+^8\text{He}$ structures are expected [IISI08].



Figure 5.12: *Depiction of the densities of the 11 intrinsic states that are used for the description of the ^{12}Be spectrum*

In order to describe ^{12}Be a set of 182 states was created. To describe the first and second 0^+ it was especially demanded that some of these show shell model like ground state properties. Others have one or two neutrons in the s shell. d shell configurations are also included.

In combination with different λ_{LS} terms 59, 14 and 20 Slater determinants were created with different constraints on the number of oscillator quanta in total N , in the neutron shells only N^n and in the proton shells only N^p . Additionally eleven intrinsic states were created using N but without applying a λ_{LS} and eight use different λ_{LS} but no other constraints. 16, four, 12 and nine Slater determinants

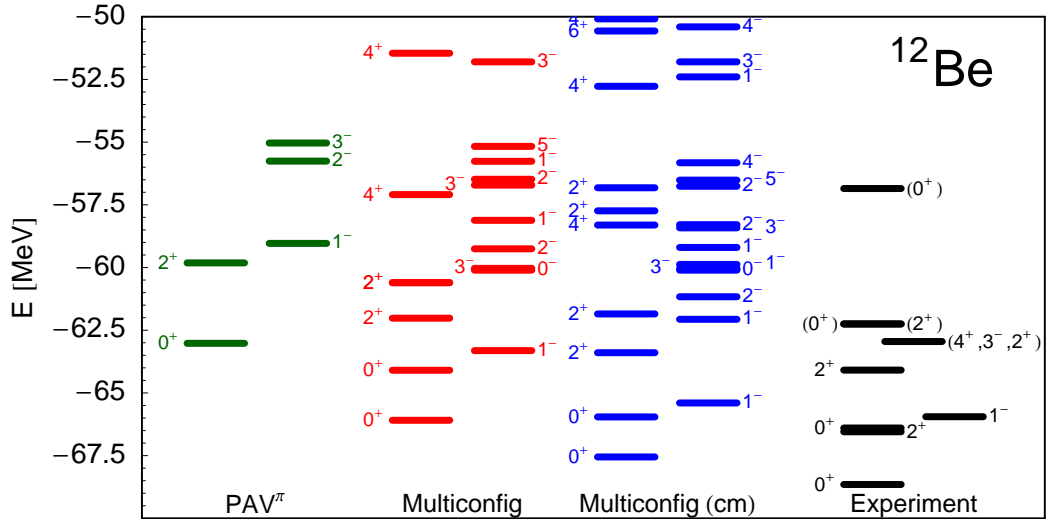


Figure 5.13: ^{12}Be energy levels. The states labeled PAV^π are obtained using only the two PAV^π states. States labeled *Multiconfig* are approximately projected on the center of mass and states labeled *Multiconfig (cm)* are projected numerically on the center of mass. The energy of the second 0^+ state has been taken from [SOD⁺07]

are constrained on certain radii, electrical dipole moments, mass quadrupole moments and mass octupole moments respectively. The mean-field, both PAV^π states and all four $\text{PAV}^{\pi_p\pi_n}$ are also provided.

Nine, seven and two Slater determinants were selected for the description of the 0^+ ground state, the 0_2^+ state and the 2^+ state respectively. For the ground state mainly intrinsic states that combine N and λ_{LS} and different radii are selected. For the excited states Slater determinants were created by applying N and λ_{LS} , N^p and λ_{LS} or a quadrupole constraint.

The first 0^+ state is rather close to the shell model ground state, but it shows one neutron outside the inner shells. It is distributed with an occupation of 0.12, 0.12, 0.16, 0.15 and 0.04 for the $0d_{5/2}$, $1s$, $1p_{3/2}$, $1p_{1/2}$ and $2s$ respectively. The 0_2^+ state has two neutrons outside the shell model like ^{10}Be core. They are distributed in the higher shells with occupation numbers of $n(0d_{5/2}) = 0.28$, $n(1s) = 0.66$, $n(0d_{3/2}) = 0.06$, $n(1p_{3/2}) = 0.14$, $n(2s) = 0.24$, $n(1d_{5/2}) = 0.07$ and even higher.

5.8 Beryllium-13

The most recent TUNL compilation [AS91] mentions shell model calculations, which are predicting a $1/2^-$ ground state and a $5/2^+$ state only at 0.05 MeV excitation energy [PWG85]. The lowest $1/2^+$ state was expected 1.55 MeV above the ground state. In 1992 an experiment observed a $5/2^-$ state but the expected

$1/2^+$ ground state remained unseen [OBD⁺92]. Later that year a shell model calculation using a density dependent Skyrme interaction and Hartree-Fock single-particle wave functions found that ^{13}Be is particle unbound with respect to neutron emission in its ground state also in the model [GPP92] (See Table: 5.1). In 1994 a $^{12}\text{Be} + n$ description of ^{13}Be predicted in a microscopic cluster model, that the ground state is a $1/2^+$ neutron-halo state which would be slightly bound [Des94]. In 1998 the ground state was experimentally found to be unstable [BKP⁺98] but due to a possible $1p_{1/2}2s_{1/2}$ inversion the parity was unclear and a $1/2^-$ ground state was proposed [LMSV99].

The experimental data shown in Figure 5.15 has been taken from [SMA⁺07].

In the calculations presented for this work a total of 127 Slater determinants are supplied as a basis for the description of ^{13}Be . The parameters of the variables in these intrinsic states are selected by minimizing the energy in the parity projected space. The Slater determinant that is created in the mean-field variation and the two PAV^π states are also included. 65 Slater determinants were created by combining different constraints on the number of oscillator quanta and using interactions with different $\vec{L} \cdot \vec{S}$ strengths in combination with projections on both parities. 16 intrinsic states obey the oscillator quanta in the two lowest proton shells. On the neutron side only three Slater determinants are provided since most of the Slater determinants created by applying the full oscillator constraint show mainly neutron excitations already. 15 intrinsic states obey different values for the radius constraint, eight Slater determinants were created by using the quadrupole constraint, six intrinsic states were minimized while constraining the octupole deformation and five further Slater determinants are made to fulfill given dipole moments. Three shell-model like intrinsic states were created using constraints on oscillator quanta and single-particle \vec{j}^2 . They correspond very well to the $^{12}\text{Be} + n$ $d_{5/2}$ shell model ground state, the $s_{1/2}$ state and a $(d_{5/2})^2$ state with a hole in the neutron $p_{1/2}$ shell. Additionally one Slater determinant was created by adding an extra neutron to the fixed core that is the best Slater determinant from the ^{12}Be calculation. This intrinsic state with the fixed core is the dominant contribution for the $1/2^+$ state and the first state in Figure 5.14.

The PAV^π states are usually starting points for the constraint minimization but trying to obtain a reasonable PAV^π state in ^{13}Be is much more demanding than in most other nuclei. The minimization routine tries to separate one neutron from the ^{12}Be core to obtain the minimal energy. This resembles the experimental observation that ^{13}Be is unstable with respect to neutron emission on a PAV^π level. To get a sensible starting point for the PAV^π minimization the ^{12}Be intrinsic state with the lowest ground state energy was fixed and one neutron (two Gaussians) was added by hand.

Firstly this Slater determinant was minimized while constraining the number

of oscillator quanta in the neutron shell to a low value but without changing the ^{12}Be core. That way the parameters of the wavefunction for the additional neutron are chosen to describe a neutron in a low shell model orbit and have a low energy. Secondly this intrinsic state was minimized by varying all parameters of all nucleons, while applying the constraint. Thirdly it was minimized again, without any constraint to obtain a state that can be interpreted as the PAV^π state.

In this PAV^π state one neutron orbit is very broad but the state seems to be a local minimum. Most of the other states, that were created using the PAV^π state as a starting point, are made to be more compact than this PAV^π state, in terms of the value of the corresponding constraint. The Slater determinant that gives the lowest energy of the ground state is a state that was created out of the aforementioned state with the fixed ^{12}Be core by performing a PAV^π minimization, again without applying any constraints.



Figure 5.14: *Depiction of the intrinsic densities of the 24 intrinsic states that were used for the description of the ^{13}Be spectrum. The first 15 states are used to describe the positive parity while the last nine are to describe the negative parity.*

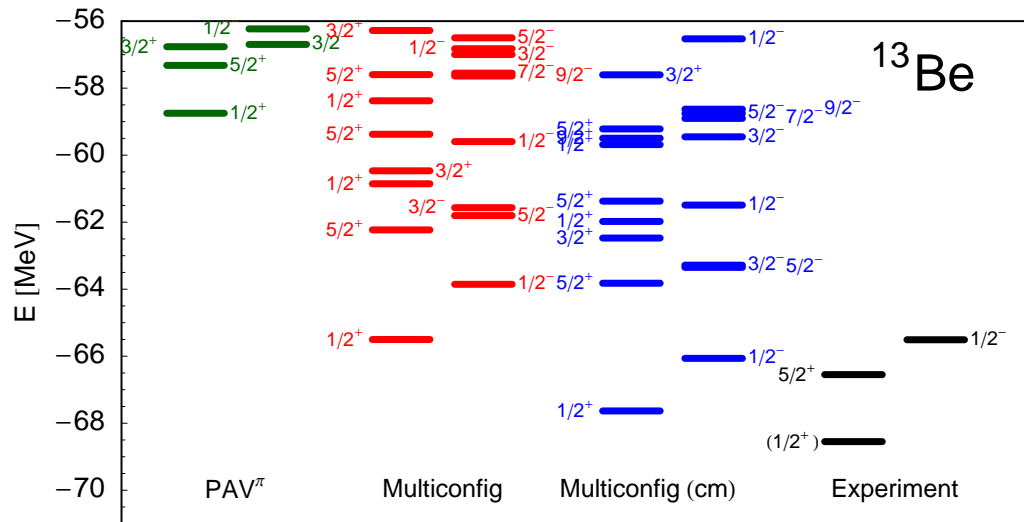


Figure 5.15: ^{13}Be energy levels. The states labeled PAV^π were obtained using only the two PAV^π states. States labeled Multiconfig are approximately projected on the center of mass. While states labeled Multiconfig (CM) are projected numerically on the center of mass.

5.9 Beryllium-14

^{14}Be also is a Borromean nucleus [MLO⁺01]. That is why it is often described as having a $^{12}\text{Be} + 2n$ structure [TTT04, Nun05].

Experimental data for ^{14}Be has been taken from [SMA⁺07].

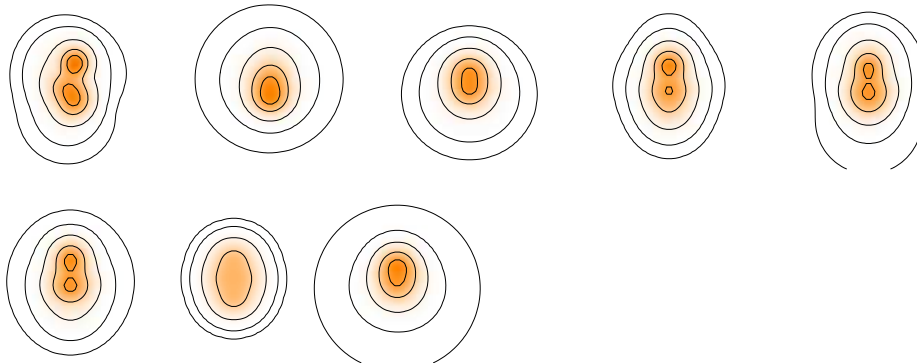


Figure 5.16: *Depiction of the intrinsic densities of the 8 states that were used for the description of the ^{14}Be spectrum.*

To describe ^{14}Be within the FMD model a set of 104 Slater determinants was created. 70 of these were minimized while projecting on positive parity and 33 were projected on negative parity before variation. The Hartree-Fock or mean-field state that is obtained without any projection is also supplied. 37 of the provided Slater determinants were created by applying a combination of N and λ_{LS} .

The intrinsic states for describing ^{14}Be are all selected to improve the 0^+ ground state. A reason for that is the computing time: calculating a single Hamiltonian matrix element with numerical center of mass projection for an FMD-state with 28 Gaussians takes roughly one week on a single CPU. For this Hilbert space spanned by eight Slater determinants 64 matrix elements were calculated. The energy of the 1^- state would be lowered to at least -62 MeV by adding appropriate states.

The selected intrinsic states are the VAP state, one state with $N^n = 13$ and six states that were created by using a combination of N and λ_{LS} .

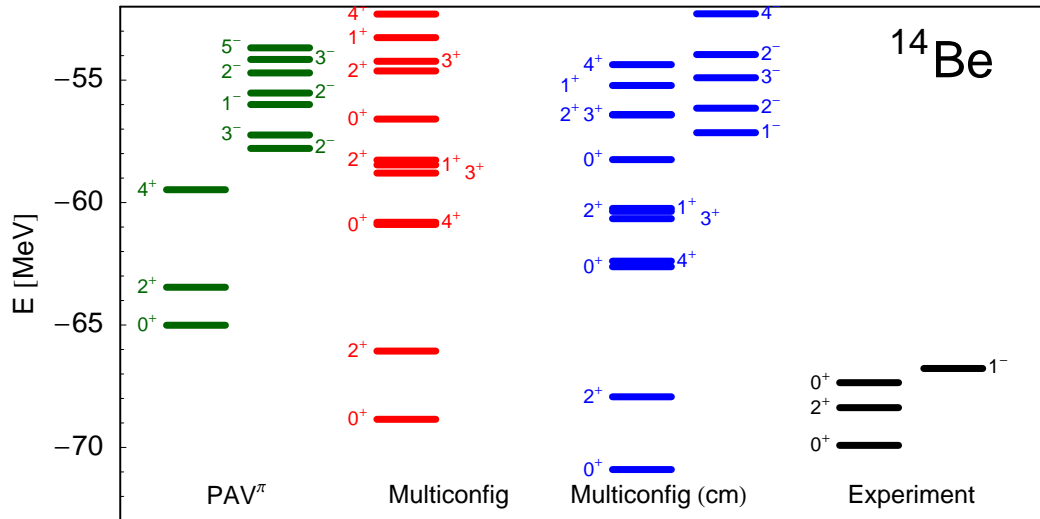


Figure 5.17: ^{14}Be energy levels. The states labeled PAV π were obtained using only the two PAV π states. States labeled Multiconfig were approximately projected on the center of mass. As energy of the 2 $^+$ state the value mentioned in [SNK $^+$ 07] is used. Experimental data has been taken from [SMA $^+$ 07].

	1n	2n	3n
⁸ Be	20.20		
⁹ Be	1.38	21.58	
¹⁰ Be	6.30	7.68	27.88
¹¹ Be	0.93	7.22	8.60
¹² Be	0.89	1.82	8.11
¹³ Be	0.11	1.00	1.93
¹⁴ Be	3.27	3.38	4.27

Table 5.2: Neutron thresholds in MeV as calculated in this work.

5.10 Overview

This section provides an overview about the obtained results on Beryllium isotopes and their ground state properties.

Table 5.10 shows the neutron separation energies as calculated from the ground state energies obtained from the FMD calculations. A direct comparison between these is not perfect since VAP states are not always equally well minimized for all isotopes. VAP states are the dominant contribution to the ground state.

In Figure 5.18 the differences in energy between the experimentally observed and the calculated ground states are shown. A positive energy difference corresponds to a calculated energy above the experimentally observed while a negative value indicates an overbound nucleus. In ¹²Be and ¹³Be the calculated energies are above the experimentally measured values. A reason for this is the usage of VAP states. The dominant contribution to describe ground state energies comes from the VAP states. In the case of ¹²Be one VAP state was provided. This state was made to have a large *d* shell occupation to account for the $1s_{1/2} d_{5/2}$ admixture. For ¹³Be no numerically sensible VAP state was obtained at all.

In Figure 5.19 the matter radii for particle stable Beryllium isotopes are shown.

In Table 5.3 the point radii as calculated for the particle stable Be isotopes are shown. In the case of ¹¹Be radii are shown for the calculated ground state $1/2^-$ and the experimentally known ground state $1/2^+$.

Table 5.4 lists the calculated charge radii and the experimentally observed charge radii as found in [NTZ⁺09]. In comparison to other contemporary models the charge radii obtained in this work are largest calculated values for ⁷Be, ⁹Be, ¹⁰Be and ¹¹Be [NTZ⁺09].

In table 5.5 the nuclear magnetic moments for the stable even *A* nuclei are shown. Again to ease comparison, the experimentally known magnetic moments from [NTZ⁺09] are also listed. Values in parenthesis are the error of the last given digit. Nuclear magnetic moments are given in units of $\mu_0 = \frac{e\hbar}{2m_p}$.

5.10 Overview

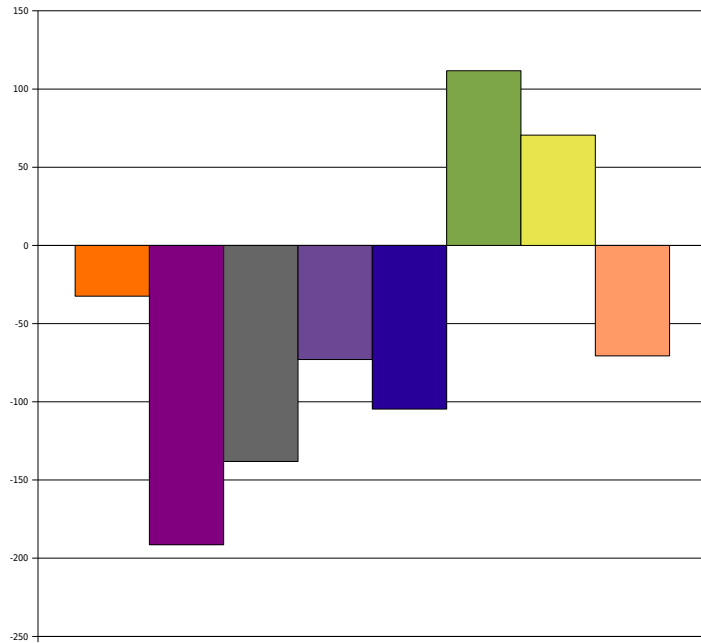


Figure 5.18: Differences between the experimentally observed and the calculated ground state energies of ^7Be (l.h.s) to ^{14}Be (r.h.s.). The differences are given in KeV/u.

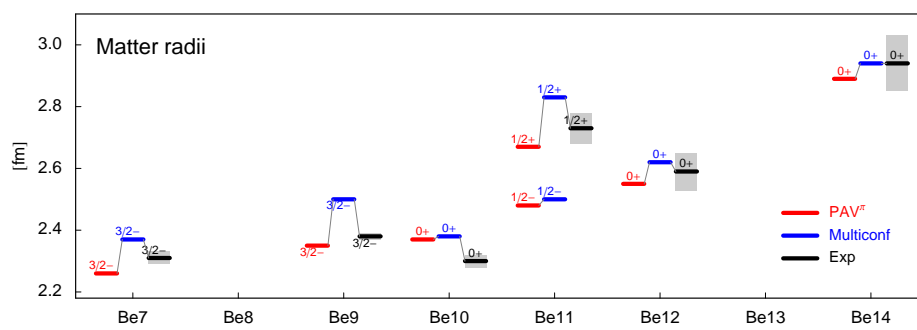


Figure 5.19: Matter radii of the Beryllium isotopes as calculated. The red lines indicate the radii as obtained from a PAV π calculation while the blue lines indicate the radii calculated from the configuration mixing calculation. The black lines represent experimentally known radii while the gray band indicates experimental uncertainties.

	mass	proton	neutron	experiment
${}^7\text{Be}$	2.37	2.46	2.25	2.31
${}^8\text{Be}$				
${}^9\text{Be}$	2.50	2.42	2.55	2.38
${}^{10}\text{Be}$	2.38	2.24	2.47	2.30
${}^{11}\text{Be} (1/2^+)$	2.83	2.33	3.09	2.73
${}^{11}\text{Be} (1/2^-)$	2.50	2.22	2.65	
${}^{12}\text{Be}$	2.62	2.30	2.76	2.59
${}^{13}\text{Be}$				
${}^{14}\text{Be}$	2.94	2.42	3.12	2.89

Table 5.3: Point radii in fm as calculated in this work. Additionally experimentally known radii are also given.

	FMD	Experiment
${}^7\text{Be}$	2.60	2.647 (15)
${}^8\text{Be}$		
${}^9\text{Be}$	2.56	2.519(12)
${}^{10}\text{Be}$	2.33	2.357(16)
${}^{11}\text{Be}$	2.44	2.460(16)
${}^{12}\text{Be}$	2.42	
${}^{13}\text{Be}$		
${}^{14}\text{Be}$	2.52	

Table 5.4: Charge radii in fm as calculated in this work and as known from recent experiments. Experimental values have been taken from [NTZ⁺09] or references therein.

	FMD	Experiment
${}^7\text{Be}$	-1.33	-1.3996(8)
${}^9\text{Be}$	-0.99	-1.177432(3)
${}^{11}\text{Be}$	-1.75	-1.6819(4)

Table 5.5: Nuclear magnetic moments in μ_0 as calculated in this work and as known from recent experiments. Experimental values have been taken from [NTZ⁺09] or references therein.

5.10 Overview

In Figures 5.20 and 5.21 point densities of the ground states are shown as, obtained after configuration mixing. Ground state densities for unstable nuclei are not plotted. These are calculated as a Fourier transform of a form factor using a δ -like ansatz. Details about the calculation of point densities, using the form factor and the decomposition into angular momenta, can be found in the appendix in subsection A.3.3.

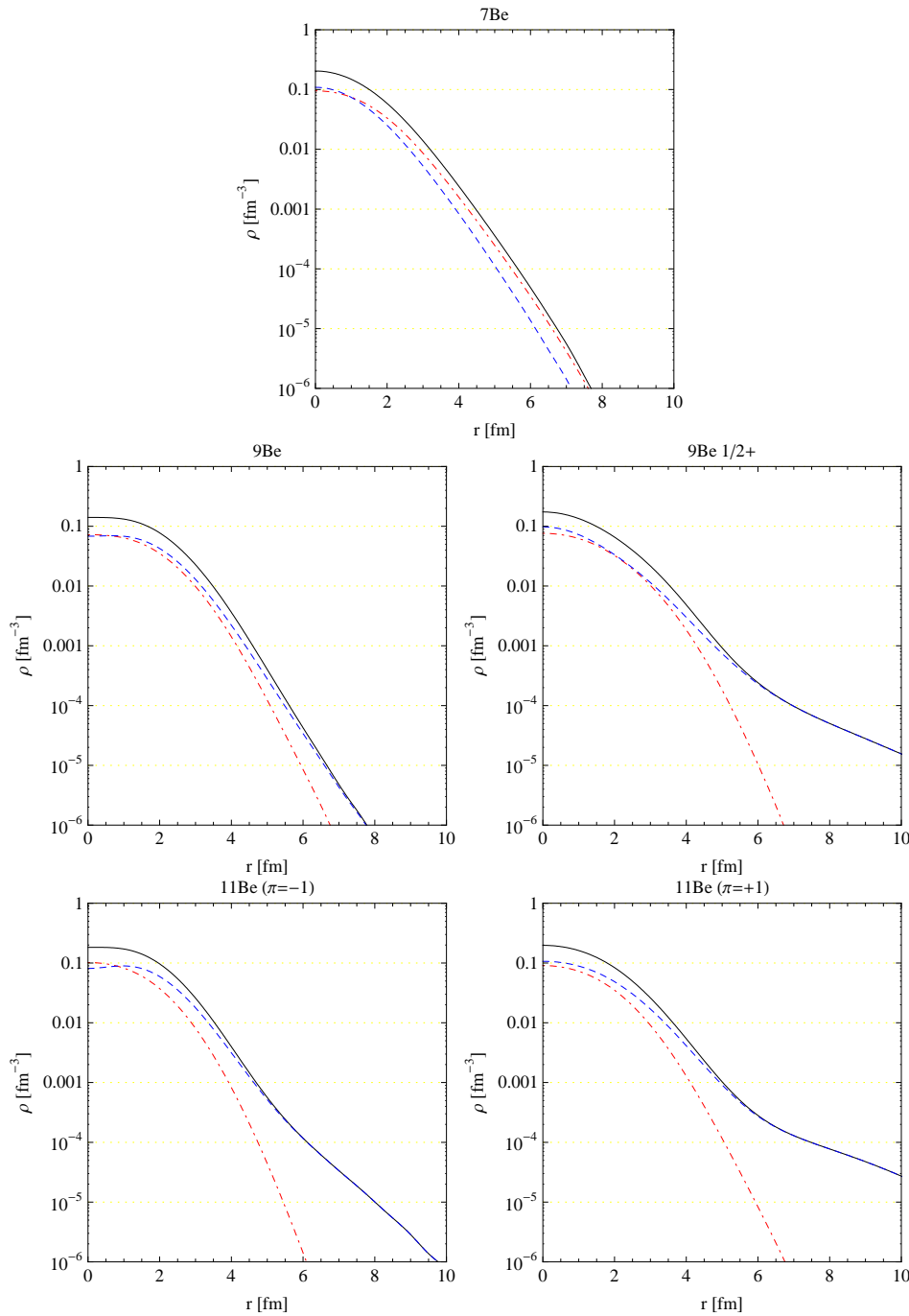


Figure 5.20: Point density distributions for the ground states of the stable odd Be nuclei ${}^7\text{Be}$, ${}^9\text{Be}$ and ${}^{11}\text{Be}$ in units of fm^{-3} . The line styles are representing the density distribution. They abide by the following scheme: matter: continuous black line, neutron: dashed blue line and proton: dot-dashed red line. For ${}^9\text{Be}$ and ${}^{11}\text{Be}$ the positive (l.h.s) and negative parity (r.h.s.) point densities are given.

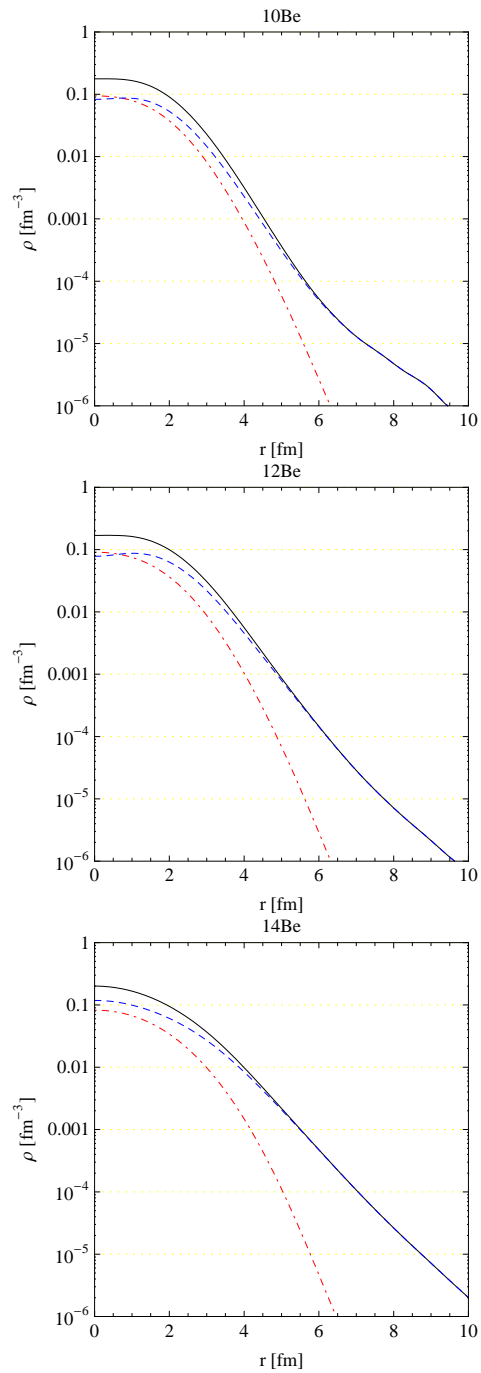


Figure 5.21: Point density distributions for the ground states of the stable even Be nuclei ^{10}Be , ^{12}Be and ^{14}Be in units of fm $^{-3}$. The line styles are representing the density distribution. They abide by the following scheme: matter: continuous black line, neutron: dashed blue line and proton: dot-dashed red line.

The electromagnetic transitions between the obtained states are also calculated. In the appendix in subsection A.3.1 the definitions of the transition amplitudes and the reduced transition strengths are given.

As a subset of the calculated reduced transition strengths is shown in the following Tables. In Table 5.6 they are listed for the E1 transitions to the ground state. Table 5.7 shows M1 transitions to the ground state and Table 5.8 shows the dominant E2 reduced transition strengths to the ground state.

	from	to	approx. CM	CM
⁷ Be	1/2 ⁻	3/2 ⁻	0.097	0.132
⁸ Be	1 ⁻	0 ⁺	0.011	0.012
⁹ Be	1/2 ⁺	3/2 ⁻	0.000	0.000
¹⁰ Be	1 ⁻	0 ⁺	0.003	0.016
¹¹ Be	1/2 ⁻	1/2 ⁺	0.003	0.026
¹² Be	1 ⁻	0 ⁺	0.004	0.001
¹³ Be	1/2 ⁻	1/2 ⁺	0.000	0.000
¹⁴ Be	1 ⁻	0 ⁺	0.037	0.001

Table 5.6: Reduced $B(E1)$ transition strengths to the ground state. Units are in e^2 fm.

	from	to	approx. CM	CM
⁷ Be	1/2 ⁺	3/2 ⁻	3.161	3.200
⁸ Be	1 ⁺	0 ⁺	0.189	0.001
⁹ Be	5/2 ⁺	3/2 ⁻	0.510	0.517
¹⁰ Be	1 ⁺	0 ⁺	0.002	0.011
¹¹ Be	3/2 ⁻	1/2 ⁺	0.002	0.002
¹² Be	1 ⁺	0 ⁺	0.001	0.001
¹³ Be	3/2 ⁻	1/2 ⁺	0.000	0.000
¹⁴ Be	1 ⁺	0 ⁺	0.001	0.001

Table 5.7: Reduced $B(M1)$ transition strengths to the ground state. In units of the nuclear magneton μ_0^2 .

	from	to	approx. CM	CM
⁷ Be	1/2 ⁻	3/2 ⁻	34.949	36.333
⁸ Be	2 ⁺	0 ⁺	29.306	28.530
⁹ Be	5/2 ⁻	3/2 ⁻	25.701	27.043
¹⁰ Be	2 ⁺	0 ⁺	9.399	8.134
¹¹ Be	5/2 ⁺	1/2 ⁺	8.744	9.086
¹² Be	2 ⁺	0 ⁺	4.223	4.427
¹³ Be	5/2 ⁺	1/2 ⁺	8.298	8.298
¹⁴ Be	2 ⁺	0 ⁺	6.045	11.185

Table 5.8: Reduced $B(E2)$ transition strengths. Units are in $e^2 \text{ fm}^4$.

Chapter 6

Outlook

In this work the nuclear structure of the Beryllium isotopes in the mass range from $A = 7$ to $A = 14$ is presented. The results are calculated using the same quasi realistic interaction. FMD is a versatile model to solve the nuclear many-body problem. Since it is a microscopic description further properties like radii, magnetic moments, deformation parameters and electromagnetic transitions have been directly calculated from the obtained energy eigenstates.

Despite all possibilities the FMD model provides, there are many ideas on how to extend the existing implementation of Fermionic Molecular Dynamics.

A first approach is to improve known imperfections of the two-body interaction. Recent attempts [RRH08] to extract the UCOM correlation functions from the so called Similarity Renormalization Group (SRG) will result in an improved UCOM interaction. Such an interaction might be used as a foundation for a new FMD interaction.

Altering the strength of the $\vec{L} \cdot \vec{S}$ correction term induces corrections for other terms. To account for more elaborate Hilbert spaces these corrections will be altered as well. Since the states as created in variational methods depend on the interaction and the fit of the interaction terms depends of the chosen Hilbert space, a self-consistent treatment of this problem is not straightforward.

By choosing the range of the tensor the contribution of three-body forces is minimized. This does not imply that three-body forces do not improve the description. Ideas exist to introduce three-body forces in the interaction. For the FMD code this would connote the need for several extensions. Since the amount of computing time needed would dramatically increase this interaction could only be used for describing very light nuclei.

With the ongoing increase of available computing time it becomes possible to also increase the numerical complexity of the calculations. Increasing the size of the Hilbert space is one way to improve the convergence of the energies, but the

numerical effort grows with the square of the number of states. In order to keep the number of Slater determinants small, more and more converged VAP states could be used. Using converged VAP states will eventually require the use of an adapted interaction.

By using only one Gaussian per nucleus, nuclei up to $A = 30$ are in the range of FMD configuration mixing calculations.

As shown in [BFN08] it is possible, but not yet common to vary isospin mixed states and apply isospin projection afterwards.

By extending the model to account for strangeness hyperons could be included in the calculations to describe hypernuclei. To do this consistently, single-particle spin and isospin values possible could also be generalized.

Appendix **A**

Appendix

A.1 General relations

The abbreviations

$$\lambda_{kl} = \frac{1}{a_k^* + a_l} \quad (\text{A.1})$$

$$\alpha_{kl} = \frac{a_k^* a_l}{a_k^* + a_l} = \lambda_{kl} a_k^* a_l \quad (\text{A.2})$$

$$\vec{\rho}_{kl} = \frac{a_l \vec{b}_k^* + a_k^* \vec{b}_l}{a_k^* + a_l} = \lambda_{kl} (a_l \vec{b}_k^* + a_k^* \vec{b}_l) \quad (\text{A.3})$$

$$\vec{\pi}_{kl} = i \frac{\vec{b}_k^* - \vec{b}_l}{a_k^* + a_l} = i \lambda_{kl} (\vec{b}_k^* - \vec{b}_l) \quad (\text{A.4})$$

are defined to get a shorter notation and especially for using them in the code to save computing time. The quantities $\vec{\rho}_{kl}$ and $\vec{\pi}_{kl}$ are the one body matrix elements of the position operator and the momentum operator:

$$\vec{\rho}_{kl} := \frac{\langle q_k | \vec{x} | q_l \rangle}{\langle q_k | q_l \rangle} \quad (\text{A.5})$$

$$\vec{\pi}_{kl} := \frac{\langle q_k | \vec{k} | q_l \rangle}{\langle q_k | q_l \rangle}. \quad (\text{A.6})$$

A.1 General relations

Their derivatives with respect to a_k^* are

$$\frac{\partial \lambda_{kl}}{\partial a_k^*} = -\frac{1}{(a_k^* + a_l)^2} = -\lambda_{kl}^2 \quad (\text{A.7})$$

$$\frac{\partial \alpha_{kl}}{\partial a_k^*} = \frac{a_l}{a_k^* + a_l} - \frac{a_k^* a_l}{(a_k^* + a_l)^2} = \lambda_{kl}(a_l - \alpha_{kl}) \quad (\text{A.8})$$

$$\frac{\partial \vec{\pi}_{kl}}{\partial a_k^*} = \frac{(\vec{b}_k^* - \vec{b}_l)}{i(a_k^* + a_l)^2} = -\lambda_{kl} \vec{\pi}_{kl} \quad (\text{A.9})$$

$$\frac{\partial \vec{\rho}_{kl}}{\partial a_k^*} = \frac{\vec{b}_l}{a_k^* + a_l} - \frac{(a_l \vec{b}_k^* + a_k^* \vec{b}_l)}{(a_k^* + a_l)^2} = \lambda_{kl}(\vec{b}_l - \vec{\rho}_{kl}), \quad (\text{A.10})$$

while the nonvanishing derivatives with respect to the j component of \vec{b}_k^* is

$$\frac{\partial \pi_{kl,i}}{\partial b_{k,j}^*} = \frac{i}{a_k^* + a_l} \delta_{ij} = i \lambda_{kl} \delta_{ij} \quad (\text{A.11})$$

$$\frac{\partial \rho_{kl,i}}{\partial b_{k,j}^*} = \frac{a_l}{a_k^* + a_l} \delta_{ij} = \lambda_{kl} a_l \delta_{ij}. \quad (\text{A.12})$$

Another compact notation is the matrix element of the product of two components i and j of the position and the momentum operator:

$$\varrho_{kl,ij} := \frac{\langle q_k | \tilde{x}_i \tilde{x}_j | q_l \rangle}{\langle q_k | q_l \rangle} = (\alpha_{kl} \delta_{ij} + \rho_{kl,i} \rho_{kl,j}) \quad (\text{A.13})$$

$$\Pi_{kl,ij} := \frac{\langle q_k | \tilde{k}_i \tilde{k}_j | q_l \rangle}{\langle q_k | q_l \rangle} = (\lambda_{kl} \delta_{ij} + \pi_{kl,i} \pi_{kl,j}). \quad (\text{A.14})$$

$$\frac{\partial \varrho_{kl,ij}}{\partial q_\mu^*} = \frac{\partial \alpha_{kl}}{\partial q_\mu^*} \delta_{ij} + \frac{\partial \rho_{kl,i}}{\partial q_\mu^*} \rho_{kl,j} + \rho_{kl,i} \frac{\partial \rho_{kl,j}}{\partial q_\mu^*} \quad (\text{A.15})$$

$$\frac{\partial \Pi_{kl,ij}}{\partial q_\mu^*} = \frac{\partial \lambda_{kl}}{\partial q_\mu^*} \delta_{ij} + \frac{\partial \pi_{kl,i}}{\partial q_\mu^*} \pi_{kl,j} + \pi_{kl,i} \frac{\partial \pi_{kl,j}}{\partial q_\mu^*} \quad (\text{A.16})$$

$$\frac{\partial}{\partial q_\mu^*} \langle q_k | \tilde{x}_i \tilde{x}_j | q_l \rangle = \left[\frac{\partial \varrho_{kl,ij}}{\partial q_\mu^*} n_{kl} + \varrho_{kl,ij} \frac{\partial n_{kl}}{\partial q_\mu^*} \right] \delta_{mk} \quad (\text{A.17})$$

$$\frac{\partial}{\partial q_\mu^*} \langle q_k | \tilde{k}_i \tilde{k}_j | q_l \rangle = \left[\frac{\partial \Pi_{kl,ij}}{\partial q_\mu^*} n_{kl} + \Pi_{kl,ij} \frac{\partial n_{kl}}{\partial q_\mu^*} \right] \delta_{mk} \quad (\text{A.18})$$

A.2 Derivatives of the oscillator quanta constraint

First the derivatives of the two matrices X and K are needed

$$\frac{\partial X_{ij}^{p,n}}{\partial q_\mu^*} = \frac{\partial}{\partial q_\mu^*} \langle q_k | \sum_{l=1}^A \tilde{P}^{p,n}(l) (\tilde{x}_i(l) - \langle \tilde{X}_i^{\text{CM}} \rangle) (\tilde{x}_j(l) - \langle \tilde{X}_j^{\text{CM}} \rangle) | q_l \rangle \quad (\text{A.19})$$

$$\frac{\partial K_{ij}^{p,n}}{\partial q_\mu^*} = \frac{\partial}{\partial q_\mu^*} \langle q_k | \sum_{l=1}^A \tilde{P}^{p,n}(l) (\tilde{k}_i(l) - m \langle \tilde{V}_i^{\text{CM}} \rangle) (\tilde{k}_j(l) - m \langle \tilde{V}_j^{\text{CM}} \rangle) | q_l \rangle \quad (\text{A.20})$$

This derivative is only valid if projecting on protons or neutrons

$$\begin{aligned} \frac{\partial K_{ij}^{p,n}}{\partial q_\mu^*} &= \sum_{k,l=1}^A \frac{\partial}{\partial q_\mu^*} (\langle q_k | \tilde{k}_i \tilde{k}_j \tilde{P}^{p,n} | q_l \rangle \mathcal{O}_{lk}) + \frac{m_{p,n}^2 A^{p,n}}{M^2} \frac{\partial}{\partial q_\mu^*} (\langle \tilde{K}_i^{\text{CM}} \rangle \langle \tilde{K}_j^{\text{CM}} \rangle) \\ &\quad - \frac{m_{p,n}}{M} \frac{\partial}{\partial q_\mu^*} (\langle \tilde{K}_i^{p,n} \rangle \langle \tilde{K}_j^{\text{CM}} \rangle + \langle \tilde{K}_j^{p,n} \rangle \langle \tilde{K}_i^{\text{CM}} \rangle), \end{aligned} \quad (\text{A.21})$$

while this is only valid if no proton or neutron projection is performed

$$\begin{aligned} \frac{\partial K_{ij}}{\partial q_\mu^*} &= \sum_{k,l=1}^A \frac{\partial}{\partial q_\mu^*} (\langle q_k | \tilde{k}_i \tilde{k}_j | q_l \rangle \mathcal{O}_{lk}) + \frac{m_p^2 Z + m_n^2 N}{M^2} \frac{\partial}{\partial q_\mu^*} (\langle \tilde{K}_i^{\text{CM}} \rangle \langle \tilde{K}_j^{\text{CM}} \rangle) \\ &\quad - \frac{\langle \tilde{K}_j^{\text{CM}} \rangle}{M} \sum_{k,l=1}^A \frac{\partial}{\partial q_\mu^*} (\langle q_k | m \tilde{k}_i | q_l \rangle \mathcal{O}_{lk}) \\ &\quad - \frac{\langle \tilde{K}_i^{\text{CM}} \rangle}{M} \sum_{k,l=1}^A \frac{\partial}{\partial q_\mu^*} (\langle q_k | m \tilde{k}_j | q_l \rangle \mathcal{O}_{lk}). \end{aligned} \quad (\text{A.22})$$

The derivative of N expressed by X and K and their derivatives is

$$\frac{\partial N}{\partial q_\mu^*} = \text{Tr} \left(\frac{\partial N^{\frac{1}{2}}}{\partial q_\mu^*} \right) \quad (\text{A.23})$$

$$= \frac{1}{2} \text{Tr} \left(N^{-\frac{1}{2}} \cdot \frac{\partial N}{\partial q_\mu^*} \right) \quad (\text{A.24})$$

$$= \frac{1}{2} \text{Tr} \left([X \cdot K]^{-\frac{1}{2}} \cdot \left[\frac{\partial X}{\partial q_\mu^*} \cdot K + X \cdot \frac{\partial K}{\partial q_\mu^*} \right] \right). \quad (\text{A.25})$$

A.3 Properties

A.3.1 Electromagnetic transitions

The transition amplitudes are calculated as

$$T(E\lambda) = \frac{8\pi(\lambda + 1)}{\lambda [(2\lambda + 1)!!]^2} q^{2\lambda+1} B(E\lambda) \quad (\text{A.26})$$

where $B(E\lambda)$ is the reduced transition strength from the initial to the final state

$$B(E\lambda) = \frac{2J_f + 1}{2J_i + 1} \left| \frac{\langle J_f \| \tilde{M}(E\lambda) \| J_i \rangle}{\sqrt{2J_f + 1}} \right|^2. \quad (\text{A.27})$$

A.3.2 Harmonic oscillator occupation numbers

The harmonic oscillator occupation numbers that are used to compare to the configuration mixing shell model are

$$n_{nlj} = \sum_m \frac{\langle \Psi | a_{nljm}^\dagger a_{nljm} | \Psi \rangle}{\langle \Psi | \Psi \rangle}. \quad (\text{A.28})$$

Here $|\Psi\rangle$ is usually either a Slater determinant $|Q\rangle$ or the angular momentum projected multi configuration space after K -Mixing $|Q^{(a)}; J^\pi M; \kappa_a\rangle$.

A.3.3 Form factors

To calculate the radial point density of a configuration mixing state $|\Psi\rangle$ the form factor is used. To get the charge density the form factor is multiplied by the proton and the neutron form factor. After the Fourier transformation this is identical to the evaluation of a convolution.

The proton or neutron densities are given by the delta like ansatz:

$$\rho^{p,n}(\vec{x}) = \sum_{l=1}^A \langle \Psi | P^{p,n}(l) \delta^3(\vec{x}(l) - \vec{X}_{\text{CM}} - \vec{x}) | \Psi \rangle. \quad (\text{A.29})$$

To solve the integral in the definition of the form factor it is convenient to use the Fourier representation of the δ function:

$$\delta^3(\vec{x}(l) - \vec{X}_{\text{CM}} - \vec{x}) = \frac{1}{(2\pi)^3} \int d^3k e^{i\vec{k} \cdot (\vec{x}(l) - \vec{X}_{\text{CM}} - \vec{x})}. \quad (\text{A.30})$$

The form factor is defined as the Fourier transform of the density distribution:

$$F^{p,n}(\vec{q}) = \int d^3x \rho^{p,n}(\vec{x}) e^{i\vec{q}\cdot\vec{x}}. \quad (\text{A.31})$$

After inserting the density $\rho^{p,n}$ and evaluating the integral the form factor becomes:

$$F^{p,n}(\vec{q}) = \sum_{l=1}^A \langle \Psi | P^{p,n}(l) e^{i\vec{q}\cdot\vec{x}(l)} e^{-i\vec{q}\cdot\vec{x}_{\text{CM}}} | \Psi \rangle. \quad (\text{A.32})$$

The operator $e^{-i\vec{q}\cdot\vec{x}_{\text{CM}}}$ gives a boost with the velocity $\vec{V} = -\frac{1}{M}\vec{q}$ to the many-body state $|\Psi\rangle$. It is evaluated by altering the parameters of the ket $|\Psi(\vec{V} = -\frac{1}{M}\vec{q})\rangle = e^{-i\vec{q}\cdot\vec{x}_{\text{CM}}}|\Psi\rangle$ to account for this boost. The one-body operator needed to calculate remaining matrix elements $\langle \Psi | P^{p,n}(l) e^{i\vec{q}\cdot\vec{x}(l)} | \Psi(\vec{V} = -\frac{1}{M}\vec{q}) \rangle$ is

$$\langle q_k | e^{i\vec{q}\cdot\vec{x}} | q_l \rangle = e^{i\vec{p}_{kl}\cdot\vec{q} - \frac{1}{2}\alpha_{kl}\vec{q}^2} R_{kl} S_{kl} T_{kl} \quad (\text{A.33})$$

R_{kl} is the spatial overlap of the single particle states $|q_k\rangle$ and $|q_l\rangle$. For the case of one Gaussian per nucleus it can be found in equation (3.4).

The angular momentum components are obtained by projection:

$$F_{LM}(\vec{q}) = \int d^2\Omega_q F(\vec{q}) Y_{LM}(\hat{q}). \quad (\text{A.34})$$

This expression is given in spherical coordinates $\hat{q} := \frac{\vec{q}}{\|\vec{q}\|}$ is the unit vector with the same angles Ω_q as \vec{q} .

The form factor expressed in terms of the angular momentum components is:

$$F(\vec{q}) = \sum_{LM} F_{LM} Y_{LM}^*(\hat{q}). \quad (\text{A.35})$$

The form factors are calculated on a grid in the three spacial coordinates. They are expanded in terms of their angular momentum components. To calculate the point densities only the monopole term is used.

A.4 Notation

- Planck units are used throughout this thesis ($\hbar = c = 1$).
- As usual in nuclear physics distances are measured in Fermi (1 fm = 10^{-15} m). This implies that energy, mass and momentum are given in fm^{-1} .
- To simplify comparison with experimental data, calculated energies are converted to MeV by multiplying with $\hbar c = 197.327053 \text{ MeV fm}$
- Vectors are indicated by an arrow: \vec{b} .
- Operators are marked by a tilde underneath the symbol: \tilde{H} .
- Operators, eigenstates and eigenvalues may be represented by the same letter $\tilde{k}|k; n\rangle = k_n|k; n\rangle$.
- Matrices are denoted by a sans-serif letter: H.
- The nuclear saturation density used is $\rho_0 = 0.17 \text{ fm}^{-3}$.
- Numbering of energy levels in spectra starts at one for the lowest energy state with given J^π . The “1” indicating the lowest state is omitted. The first 0^+ state of a nucleus is denoted as 0^+ while the first excited 0^+ is denoted as 0_2^+ .
- Shell model single-particle orbits are denoted by the radial quantum number (i.e. the number of nodes in the radial wavefunction) and the usual spectroscopic notation (i.e. “s” $l = 0$, “p” $l = 1$, “d” $l = 2$, “f” $l = 3 \dots$).
- When using the spectroscopic notation the $j = 1/2$ quantum number might be omitted for s ($l=0$) states and the radial quantum number might be omitted if it is zero.
- All intrinsic density plots are shown from -9 to 9 fm on both axes.

Curriculum Vitae

Name: Torabi, Bahram Ramin
Geburtsdatum: 10. Juni 1979
Geburtsort: Berlin, Wilmersdorf
Staatsangehörigkeit: deutsch

- 05/2005 - 01/2009 Anfertigung der Dissertation bei dem GSI Helmholtzzentrum für Schwerionenforschung und Promotionsstudent der Technischen Universität Darmstadt
- 10/2003 - 03/2005 Anfertigung der Diplomarbeit im Hahn-Meitner-Institut Berlin (heutiger Name: Helmholtz-Zentrum Berlin für Materialien und Energie)
Thema: *Untersuchung von Clusterzuständen in leichten, neutronenreichen Kernen mit Multi-Nukleonen-Transferreaktionen*
- 08/2003 - 09/2003 Sommerschule im Hahn-Meitner-Institut Berlin
Thema: *Untersuchungen im Mischkristallsystem $Cu_xNi_{1-x}Cr_2O_4$ am Forschungsreaktor BERII*
- 09/2002 3. Sommerschule Mikroelektronik in Dresden
- 04/2000 - 03/2005 Studium der Physik (grundlagenorientiert) an der Technischen Universität Berlin, Abschluss: Diplom
- 08/1992 - 07/1999 Friedrich Engels Gymnasium, Berlin Reinickendorf Abschluss: Allgemeine Hochschulreife

Bibliography

- [AS91] F. Ajzenberg-Selove. Energy levels of light nuclei $A = 13$ – 15 . *Nuclear Physics A*, 523(1):1–196, February 1991.
- [AWT03] G. Audi, A. H. Wapstra, and C. Thibault. The AME2003 atomic mass evaluation (II). Tables, graphs and references. *Nuclear Physics A*, 729:337–676, December 2003.
- [BDK⁺07] H. G. Bohlen, T. Dorsch, T. Kokalova, W. von Oertzen, C. Schulz, and C. Wheldon. New assignments for ^{10}Be states from the $^{12}\text{C}(^{12}\text{C}, ^{14}\text{O})^{10}\text{Be}$ reaction. *Nuclear Physics A*, 787:451–454, May 2007.
- [BFN08] S. Bacca, H. Feldmeier, and T. Neff. Long range tensor correlations in charge and parity projected fermionic molecular dynamics. *Phys. Rev. C*, 78(4):044306–044318, October 2008.
- [BKP⁺98] A. V. Belozyorov, R. Kalpakchieva, Y. E. Penionzhkevich, Z. Dlouhý, Š. Piskoř, J. Vincour, H. G. Bohlen, M. von Lucke-Petsch, A. N. Ostrowski, D. V. Alexandrov, E. Y. Nikolskii, B. G. Novatskii, and D. N. Stepanov. Spectroscopy of ^{13}Be . *Nuclear Physics A*, 636:419–426, July 1998.
- [BM75] A. Bohr and B.R. Mottelson. *Nuclear Deformations*. W.A. Benjamin Inc., New York, nuclear structure volume II: edition, 1975.
- [CAA⁺08] N. Curtis, N. L. Achouri, N. I. Ashwood, H. G. Bohlen, W. N. Catford, N. M. Clarke, M. Freer, P. J. Haigh, B. Laurent, N. A. Orr, N. P. Patterson, N. Soić, J. S. Thomas, and V. Ziman. Breakup reaction study of the Brunnian nucleus $\text{C}10$. *Phys. Rev. C*, 77(2):021301–+, February 2008.

-
- [CK65] S Cohen and D. Kurath. Effective interactions for the 1p shell. *Nuclear Physics*, 73:1–24, January 1965.
- [Cri05] A Cribeiro. *Nuclear many-body continuum states and their boundary conditions in a collective-coordinate representation*. PhD thesis, Technische Universität Darmstadt, 2005.
- [Cus08] R. Cussons. *A Unified and Microscopic Approach to Astrophysical Nuclear Reactions using Fermionic Molecular Dynamics*. PhD thesis, Technische Universität Darmstadt, 2008.
- [Des94] P. Descouvemont. Evidence for particle stability of ^{13}Be in a microscopic cluster model. *Physics Letters B*, 331:271–275, July 1994.
- [EG70] J.M. Eisenberg and W. Greiner. *Nuclear Models Vol. I*. North-Holland, 1970.
- [EGM05] E. Epelbaum, W. Glöckle, and Ulf-G. Meißner. The two-nucleon system at next-to-next-to-next-to-leading order. *Nucl. Phys. A*, 747(2-4):362–424, January 2005.
- [EM02] D. R. Entem and R. Machleidt. Accurate nucleon–nucleon potential based upon chiral perturbation theory. *Phys. Lett. B*, 524(1-2):93–98, January 2002.
- [EM03] D. R. Entem and R. Machleidt. Accurate charge-dependent nucleon–nucleon potential at fourth order of chiral perturbation theory. *Phys. Rev. C*, 68(4):041001, Oct 2003.
- [Epe06] E. Epelbaum. Few-nucleon forces and systems in chiral effective field theory. *Prog. Part. Nucl. Phys.*, 632(2):654, 2006.
- [FBS95] H. Feldmeier, K. Bieler, and J. Schnack. Fermionic molecular dynamics for ground states and collisions of nuclei. *Nuclear Physics A*, 586:493–532, February 1995.
- [FCA⁺06] M. Freer, E. Casarejos, L. Achouri, C. Angulo, N. I. Ashwood, N. Curtis, P. Demaret, C. Harlin, B. Laurent, M. Milin, N. A. Orr, D. Price, R. Raabe, N. Soić, and V. A. Ziman. $\alpha:2n:\alpha$ Molecular Band in ^{10}Be . *Physical Review Letters*, 96(4):042501–+, January 2006.
- [FNOC05] C. Forssén, P. Navrátil, W. E. Ormand, and E. Caurier. Large basis ab initio shell model investigation of ^9Be and ^{11}Be . *Phys. Rev. C*, 71(4):044312–+, April 2005.

BIBLIOGRAPHY

- [FNRS98] H. Feldmeier, T. Neff, R. Roth, and J. Schnack. A unitary correlation operator method. *Nuclear Physics A*, 632:61–95, March 1998.
- [FS00] H. Feldmeier and J. Schnack. Molecular dynamics for fermions. *Reviews of Modern Physics*, 72:655–688, July 2000.
- [GPP92] J. M. G. Gómez, C. Prieto, and A. Poves. Hartree-Fock shell model structure of Li and Be isotopes. *Physics Letters B*, 295:1–2, November 1992.
- [Her50] G. Herzberg. *Spectra of diatomic molecules*. D. van Nostrand Comp. Inc, Princeton, vol.i edition, 1950.
- [IISI08] M. Ito, N. Itagaki, H. Sakurai, and K. Ikeda. Exotic molecular structures in highly-excited states of ^{12}Be . *Journal of Physics Conference Series*, 111(1):012010–+, May 2008.
- [Ito06] M. Ito. Non-adiabatic dynamics in ^{10}Be with the microscopic $\alpha+\alpha+N+N$ model. *Physics Letters B*, 636:293–298, May 2006.
- [IYKI05] M. Ito, K. Yabana, K. Kato, and K. Ikeda. Low-energy $\alpha + ^6\text{He}$ collisions and the continuum structures in ^{10}Be . *Journal of Physics Conference Series*, 20:185–186, January 2005.
- [KEH03] Y. Kanada-En'yo and H. Horiuchi. Cluster structures of the ground and excited states of ^{12}Be studied with antisymmetrized molecular dynamics. *Phys. Rev. C*, 68(1):014319, Jul 2003.
- [Kra01] P. Kraft. *Fermionische Molekularodynamik mit Konfigurationsmischung*. Diplomarbeit, TU Darmstadt, May 2001.
- [LMSV99] M. Labiche, F. M. Marqués, O. Sorlin, and N. Vinh Mau. Structure of ^{13}Be and ^{14}Be . *Phys. Rev. C*, 60(2):027303, Jul 1999.
- [MLO⁺01] F. M. Marqués, M. Labiche, N. A. Orr, J. C. Angélique, L. Axelsson, B. Benoit, U. C. Bergmann, M. J. Borge, W. N. Catford, S. P. Chappell, N. M. Clarke, G. Costa, N. Curtis, A. D'arrigo, E. D. Brennan, F. D. Santos, O. Dorvaux, G. Fazio, M. Freer, B. R. Fulton, G. Giardina, S. Grévy, D. Guillemaud-Mueller, F. Hanappe, B. Heusch, B. Jonson, C. L. Brun, S. Leenhardt, M. Lewitowicz, M. J. López, K. Markenroth, A. C. Mueller, T. Nilsson, A. Ninane, G. Nyman, I. Piqueras, K. Riisager, M. G. Saint Laurent, F. Sarazin, S. M. Singer, O. Sorlin, and L. Stuttgé. Three-body correlations in Borromean halo nuclei. *Phys. Rev. C*, 64(6):061301–+, December 2001.

-
- [MOWH83] D. J. Millener, J. W. Olness, E. K. Warburton, and S. S. Hanna. Strong E1 transitions in ${}^9\text{Be}$, ${}^{11}\text{Be}$, and ${}^{13}\text{C}$. *Phys. Rev. C*, 28:497–505, August 1983.
- [MSB⁺02] D. Miljanić, N. Soić, S. Blagus, S. Cherubini, E. Costanzo, M. Lattuada, M. Milin, A. Musumarra, R. G. Pizzona, D. Rendić, S. Romano, C. Spitaleri, A. Tumino, and M. Zadro. ${}^{10}\text{Be}$ and molecular states. *Fizika B*, 10:235–246, 2002.
- [Mug85] S. F. Mughabghab. Evidence for a Nucleon-Nucleus Spin-Spin Interaction in ${}^9\text{Be}$. *Phys. Rev. Lett.*, 54(10):986–988, March 1985.
- [NAA⁺00] A. Navin, D. W. Anthony, T. Aumann, T. Baumann, D. Bazin, Y. Blumenfeld, B. A. Brown, T. Glasmacher, P. G. Hansen, R. W. Ibbotson, P. A. Lofy, V. Maddalena, K. Miller, T. Nakamura, B. V. Pritychenko, B. M. Sherrill, E. Spears, M. Steiner, J. A. Tostevin, J. Yurkon, and A. Wagner. Direct Evidence for the Breakdown of the $N = 8$ Shell Closure in ${}^{12}\text{Be}$. *Physical Review Letters*, 85:266–269, July 2000.
- [Nef98] T. Neff. *Fermionische Molekulardynamik mit Konfigurationsmischungen und realistischen Wechselwirkungen*. Diplomarbeit, TU Darmstadt, July 1998.
- [Nef02] T. Neff. *Short-Ranged Central and Tensor Correlations in Nuclear Many-Body Systems*. PhD thesis, Technische Universität Darmstadt, 2002.
- [NF03] T. Neff and H. Feldmeier. Tensor correlations in the unitary correlation operator method. *Nuclear Physics A*, 713:311–371, January 2003.
- [NF08] T. Neff and H. Feldmeier. Clustering and other exotic phenomena in nuclei. *Eur. Phys. J. Special Topics*, 156:69–92, April 2008.
- [Nil55] S.G. Nilsson. *Kgl. Danske Videnskab. Selskab. Mat.-fys. Medd.*, 29(19), 1955.
- [NKG00] A. Nogga, H. Kamada, and W. Glöckle. Modern Nuclear Force Predictions for the α Particle. *Physical Review Letters*, 85:944–947, July 2000.

BIBLIOGRAPHY

- [NTZ⁺09] W. Nörtershäuser, D. Tiedemann, M. Zakova, Z. Andjelkovic, K. Blaum, M. L. Bissell, R. Cazan, G. W. F. Drake, Ch. Geppert, M. Kowalska, J. Kramer, A. Krieger, R. Neugart, R. Sanchez, F. Schmidt-Kaler, Z.-C. Yan, D. T. Yordanov, and C. Zimmermann. Nuclear Charge Radii of $^{7,9,10}\text{Be}$ and the One-Neutron Halo Nucleus ^{11}Be . *Physical Review Letters*, 102(6):062503, 2009.
- [Nun05] F. M. Nunes. Valence pairing, core deformation and the development of two-neutron halos. *Nuclear Physics A*, 757:349–359, August 2005.
- [OBD⁺92] A. N. Ostrowski, H. G. Bohlen, A. S. Demyanova, B. Gebauer, R. Kalpakchieva, C. Langner, H. Lenske, M. Lucke-Petsch, W. Oertzen, A. A. Ogloblin, Y. E. Penionzhkevich, M. Wilpert, and T. Wilpert. Mass spectroscopy of ^{13}Be . *Zeitschrift für Physik A Hadrons and Nuclei*, 343:489–490, December 1992.
- [PWG85] N. A. F. M. Poppelier, L. D. Wood, and P. W. M. Glaudemans. Properties of exotic p-shell nuclei. *Physics Letters B*, 157:120–122, July 1985.
- [RHP⁺05] R. Roth, H. Hergert, P. Papakonstantinou, T. Neff, and H. Feldmeier. Matrix elements and few-body calculations within the unitary correlation operator method. *PRC*, 72(3):034002–+, September 2005.
- [Ros57] M.E. Rose. *Elementary Theory of Angular Momentum*. John Wiley and Sons Inc., 1957.
- [RRH08] R. Roth, S. Reinhardt, and H. Hergert. Unitary correlation operator method and similarity renormalization group: Connections and differences. *Physical Review C (Nuclear Physics)*, 77(6):064003, 2008.
- [RS00] P. Ring and P. Schuck. *The Nuclear Many-Body Problem*. Springer, 2000.
- [SMA⁺07] H. Simon, M. Meister, T. Aumann, M. J. G. Borge, L. V. Chulkov, U. Datta Pramanik, T. W. Elze, H. Emling, C. Forssén, H. Geissel, M. Hellström, B. Jonson, J. V. Kratz, R. Kulessa, Y. Leifels, K. Markenroth, G. Münzenberg, F. Nickel, T. Nilsson, G. Nyman, A. Richter, K. Riisager, C. Scheidenberger, G. Schrieder, O. Tengblad, and M. V. Zhukov. Systematic investigation of the drip-line nuclei ^{11}Li and ^{14}Be and their unbound subsystems ^{10}Li and ^{13}Be . *Nuclear Physics A*, 791:267–302, July 2007.

- [SNK⁺07] T. Sugimoto, T. Nakamura, Y. Kondo, N. Aoi, H. Baba, D. Bazin, N. Fukuda, T. Gomi, H. Hasegawa, N. Imai, M. Ishihara, T. Kobayashi, T. Kubo, M. Miura, T. Motobayashi, H. Otsu, A. Saito, H. Sakurai, S. Shimoura, A. M. Vinodkumar, K. Watanabe, Y. X. Watanabe, T. Yakushiji, Y. Yanagisawa, and K. Yoneda. The first 2^+ state of ^{14}Be . *Physics Letters B*, 654:160–164, October 2007.
- [SOD⁺07] S. Shimoura, S. Ota, K. Demichi, N. Aoi, H. Baba, Z. Elekes, T. Fukuchi, T. Gomi, K. Hasegawa, E. Ideguchi, M. Ishihara, N. Iwasa, H. Iwasaki, S. Kanno, S. Kubono, K. Kurita, M. Kurokawa, Y. U. Matsuyama, S. Michimasa, K. Miller, T. Mine-mura, T. Motobayashi, T. Murakami, M. Notani, A. Odahara, A. Saito, H. Sakurai, E. Takeshita, S. Takeuchi, M. Tamaki, T. Teranishi, K. Yamada, Y. Yanagisawa, and I. Hamamoto. Lifetime of the isomeric 0_2^+ state in ^{12}Be . *Physics Letters B*, 654:87–91, October 2007.
- [Spe] P. Spellucci. Donlp2 short users guide.
- [Spe98] P. Spellucci. An sqp method for general nonlinear programs using only equality constrained subproblems. *Mathematical Programming*, 82:413–448, 1998.
- [SPO⁺07] N. C. Summers, S. D. Pain, N. A. Orr, W. N. Catford, J. C. Angélique, N. I. Ashwood, V. Bouchat, N. M. Clarke, N. Curtis, M. Freer, B. R. Fulton, F. Hanappe, M. Labiche, J. L. Lecouey, R. C. Lemmon, D. Mahboub, A. Ninane, G. Normand, F. M. Nunes, N. Soić, L. Stuttge, C. N. Timis, I. J. Thompson, J. S. Winfield, and V. Ziman. B(E1) strengths from Coulomb excitation of ^{11}Be . *Physics Letters B*, 650:124–128, June 2007.
- [TCG⁺02] DR Tilley, CM Cheves, JL Godwin, GM Hale, HM Hofmann, JH Kelley, CG Sheu, and HR Weller. Energy levels of light nuclei/A= 5, 6, 7. *Nuclear Physics A*, 708(1-2):3–163, 2002.
- [TKG⁺04] DR Tilley, JH Kelley, JL Godwin, DJ Millener, JE Purcell, CG Sheu, and HR Weller. Energy levels of light nuclei A= 8, 9, 10. *Nuclear Physics, Section A*, 745(3-4):155–362, 2004.
- [TTT04] T. Tarutina, I. J. Thompson, and J. A. Tostevin. Study of ^{14}Be with core excitation. *Nuclear Physics A*, 733:53–66, March 2004.

BIBLIOGRAPHY

- [vFKE06] W von Oertzen, M. Freer, and Y. Kanada-En'Yo. Nuclear clusters and nuclear molecules. *Physics Reports*, 432:43–113, September 2006.
- [vG84] A. G. M. van Hees and P. W. M. Glaudemans. A shell-model treatment of $(0+1)\hbar\omega$ states in $A=4-16$ nuclei (II). *Zeitschrift fur Physik*, 315:223–238, June 1984.
- [von97] W. von Oertzen. Dimers Based on the $\alpha + \alpha$ Potential and Chain States of Carbon Isotopes. *Z. Phys.*, pages 355–365, 1997.
- [von03] W. von Oertzen. Clusters and covalently bound nuclear molecules. *Physics of Atomic Nuclei*, 66:1591–1598, September 2003.
- [WB92] E. K. Warburton and B. A. Brown. Effective interactions for the $0p1s0d$ nuclear shell-model space. *Phys. Rev. C*, 46:923–944, September 1992.
- [WSS95] R. B. Wiringa, V. G. J. Stoks, and R. Schiavilla. Accurate nucleon-nucleon potential with charge-independence breaking. *Phys. Rev. C*, 51(1):38–51, Jan 1995.
- [WvG90] A. A. Wolters, A. G. M. van Hees, and P. W. M. Glaudemans. p-shell nuclei in a $(0+2)\hbar\omega$ model space. II. Results. *Phys. Rev. C*, 42:2062–2078, November 1990.

Erklärung

Hiermit erkläre ich an Eides statt, daß ich die vorliegende Dissertation selbständig verfaßt, keine anderen als die angegebenen Hilfsmittel verwendet und noch keinen Promotionsversuch unternommen habe.

Darmstadt, den 27. Januar 2009

(Ramin Torabi)

Unterschrift